UNIVERSITY OF CAPE COAST

CHARACTERIZATION OF CATARACTOUS LENSES OF SPRAGUE – DAWLEY RATS USING SELECTED OPTICAL SPECTROSCOPIC TECHNIQUES

PETER OSEI – WUSU ADUEMING

2020

UNIVERSITY OF CAPE COAST

CHARACTERIZATION OF CATARACTOUS LENSES OF SPRAGUE – DAWLEY RATS USING SELECTED OPTICAL SPECTROSCOPIC TECHNIQUES

BY

PETER OSEI - WUSU ADUEMING

Thesis submitted to the Department of Physics of the School of Physical Sciences, College of Agriculture and Natural Sciences, University of Cape Coast, in partial fulfilment of the requirements for the award of Doctor of Philosophy degree in Physics

MARCH 2020

DECLARATION

Candidate's Declaration

I hereby declare that this thesis is the result of my own original work and that no part of it has been presented for another degree in this University or elsewhere.

…………………………………   Date: …………………

Peter Osei-Wusu Adueming

(Candidate)

Supervisors' Declaration

We hereby declare that the preparation and presentation of the thesis were supervised in accordance with the guidelines on supervision of thesis laid down by the University of Cape Coast.

……………………………….   Date: …………………

Prof. Moses Jojo Eghan

(Principal supervisor)

…………………………………   Date: ………………….

Dr. Benjamin Anderson

(Co-Supervisor)

ABSTRACT

Current methods for discriminating cataractous lenses from healthy lenses during preclinical studies are based on either histopathological or clinical assessments which are weakened by subjectivity. In this work, four optical spectroscopic techniques: slit lamp microscopy, multispectral imaging (MSI), Laser-induced autofluorescence (LIAF) and attenuated total reflectance Fourier transform infrared (ATR-FTIR) spectroscopy have been used to study and characterize cataractous as well as healthy lenses of Sprague Dawley rats. With the aid of slit lamp images, mean integrated optical density (IOD) of cataractous lenses were found to increase with severity. Analysis of multispectral images captured in transmission and reflection and scattering modes showed that five wavelengths markers discriminates cataractous lenses from healthy lenses with 470 nm and 625 nm in reflection mode, and 435 nm, 590 nm and 700 nm in transmission mode. The scattering spectral bands could not discriminate cataractous lenses from healthy lenses. Fisher's linear discriminant analysis showed more than 85 % success in classifying the lenses. LIAF results revealed that spectra peak wavelengths of cataractous lenses were red-shifted with cataractous lens tissues exhibiting high autofluorescence intensity than the healthy ones. Infrared spectra from cataractous lens tissues showed intensity difference and some wavenumber shifts in vibrational modes associated with proteins from the healthy ones. *P*-values obtained from independence T-test showed significant differences in absorbed intensities at 7 peak wavenumbers. Upon applying Hierarchical cluster analysis, the infrared lens spectra data were classified as cataractous or healthy. These optical techniques may be potentially applied for improved cataract diagnosis.

KEYWORDS

Cataractous Lenses

Fisher’s Linear Discriminant Analysis

Integrated Optical Density

Laser-Induced Autofluorescence

Multispectral Imaging

Optical Spectroscopic Techniques

ACKNOWLEDGEMENTS

I would like to express my gratitude to Prof. Moses Jojo Eghan and Dr. Benjamin Anderson who are my principal and co-supervisor respectively for their supervision, advice and guidance from the very early stage of this research as well as giving me an extraordinary experience throughout the work. Above all, they provided me with unflinching encouragement and support in various ways.

My sincere appreciation also goes to the Office of the External Activity (OEA) of the Abdus Salam International Centre for Theoretical Physics (ICTP) Italy, for financially supporting my work and the opportunity given to me to attend conferences. The support from the International Programme in the Physical Sciences (IPPS) of the International Science Programme (ISP) of Uppsala University, Sweden in donating the equipment is gratefully acknowledged. I thank all members of the African Spectra Imaging Network (AFSIN) for valuable advice during scientific discussions.

I am also thankful to all Professors, lecturers and staff of the Department of Physics especially the Head, Prof. George Amoako and Dr. Samuel Sonko Sackey who is the co-ordinator of Laser and Fibre Optics Centre (LAFOC) for their support. I wish to express my profound gratitude to senior members of the LAFOC research group. I am also grateful to the entire administrative staff of LAFOC. A special thank you to Dr. Samuel Kyei and Dr. Charles Darko Takyi for your unflinching support. I really appreciate all the things you did for me.

Finally, my dear parents, caring siblings, friends and love ones deserve special mention for their inseparable support and prayers during this period of work.

DEDICATION

To all members of the OSEI-WUSU ADUEMING family- the present and the generation to come.

TABLE OF CONTENTS

CHAPTER ONE: INTRODUCTION

CHAPTER TWO: LITERATURE REVIEW

CHAPTER THREE: RESEARCH METHODS

LIST OF TABLES

LIST OF FIGURES

Figure Page

LIST OF PLATES

LIST OF ACRONYMS

AAS	Atomic Absorption Spectroscopy
AS	Absorption Spectroscopy
AFM	Atomic Force Microscopy
ANOVA	Analysis of Variance
AOI	Area of Interest
AFS	Autofluorescence Spectra
ATR	Attenuated Total Reflectance
ATR-FTIR	Attenuated Total Reflectance Fourier Transform Infra-Red
AREDS	Age-Related Eye Disease Study
BS	Beam Splitter
CAD	Computer-aided
CCD	Charge Coupled Device
CCESG	Cooperative Cataract Epidemiology Study Group
CPU	Central Processing Unit
DOAS	Differential Optical Absorption Spectroscopy
DAQ	Data Acquisition
DNA	Deoxyribonucleic Acid
EM	Electromagnetic
FE-SEM	Field Emission Scanning Electron Microscopy (FE-SEM)
FLD	Fisher’s Linear discriminant
FLDA	Fisher’s Linear Discriminant Analysis
FTIR	Fourier Transform Infra-Red
FS	Fluorescence Spectroscopy
GASMAS	Gas in Scattering Medium Absorption Spectroscopy

GUI	Graphical User Interface
HIS	Hyperspectral Imaging
H & E	Hematoxylin and Eosin
IOD	Integrated Optical Density
INAA	Instrumental Neutron Activation Analysis
IR	Infra-Red
LAFOC	Laser and Fibre Optics Centre
LDF	Linear Discriminant function
LOCS	Lens Opacities Classification System
LIDAR	Light Detection And Ranging
LIF	Laser – Induced Fluorescence
LIAF	Laser – Induced Autofluorescence
LED	Light Emitting Diode
MDA	Multivariate Data Analysis
MRI	Magnetic Resonance Imaging
MS	Mass Spectroscopy
MSI	Multispectral Imaging
MSIM	Multispectral Imaging Microscopy
MSLEDIM	Multispectral Light Emitting Diode Imaging Microscope
NIR	Near Infra-Red
NMR	Nuclear Magnetic Resonance
PCA	Principal Component Analysis
PC	Principal Component
PDF	Probability Density Functions
RBC	Red blood Cells

RNA	Ribonucleic Acid
RS	Raman Spectroscopy
SEM	Scanning Electron Microscopy
SI	Spectra Imaging
SS	Sample Stage
SLI	Slit Lamp Imaging
SLM	Slit lamp Microscope
SLT	Sectioned Lens Tissue
SSLT	Stained Sectioned Lens Tissue
STZ	Streptozocin
TDLAS	Tunable Diode Laser Absorption Spectroscopy
TEM	Transmission Electron Microscopy
TIF	Tagged Image File
TPM	Total Probability of Misclassification
USLT	Unstained Sectioned Lens Tissue
USB	Universal Serial Bus
UV	UltraViolet
VIS	Visible
WHO	World Health Organization
WMS	Wavelength Modulation Spectroscopy
XES	X-ray Emission Spectroscopy
XRI	X-Ray Imaging

LIST OF SYMBOLS AND CONSTANTS

Symbol	Meaning
I	Intensity
I_0	Unattenuated intensity
K	Potasium
Br	Bromine
V	Frequency

CHAPTER ONE

INTRODUCTION

Background to the Study

In recent years the methods of using light and light-based technologies, which is widely known to be optical techniques, to investigate, probe and or characterize materials have become wide spread among researchers. (Ellis et al., 2005; Aparicio & Harwood, 2013). The morphology and sample characterization are obtained at the microscopic, mesoscopic and macroscopic levels when light interacts with matter (Wilson et al., 2016). Optical techniques involve the use of ultraviolet (UV), visible (VIS) and infrared (IR) regions of the electromagnetic (EM) spectrum as excitation light sources (Demtroder, 2003; Svanberg, 2012). The techniques use these radiations to study its effects after interaction with material samples under investigation. Optical techniques provide useful information about the electronic, vibrational and rotational transitions of molecules/atoms. These transitions are as a result of the various excitation where the electronic transitions are due to the UV and VIS excitation and the rotational and/or vibrational is by the IR excitation (Hollas, 2004; Svanberg, 2012). Optical techniques often require minimal or no sample preparation and they provide rapid analysis as well as have the potential to run multiple test on a single sample (Wang, 2008; Sun, 2008). Currently optical techniques require reduced space, low cost instrumentation and are simpler to set-up compared to other techniques such as Instrumental Neutron Activation Analysis (INAA), Gas Chromatography (GC), High Performance Liquid Chromatography (HPLC) and Thermogravimetry (Heftmann, 2004; Greenberg et al., 2011). Optical techniques help in the study of scattering, absorption, transmission and reflection properties.

These properties go a long way to unearth features of the samples/ materials such molecular composition, crystal structure, scattering coefficient, absorption coefficient, to mention but a few.

Due to the rigorous, non- destructive and non-invasive nature of optical techniques, researchers have found them to be most promising, multidisciplinary and valuable technique which are applicable in disciplines such as biomedicine, remote sensing, food science and agriculture (Svanberg, 2004; 2009; Ellis et al., 2005; Brydegaard et al., 2011; Aparicio & Harwood, 2013).The techniques allow probing of cellular structures and dynamics for understanding the mechanisms of physiological regulation which provide cellular or molecular level information, with almost single molecule sensitivity (Michaelis et al., 2000; Prasad, 2003). They frequently interrogate endogenous optical contrast in tissue samples which include absorbing, scattering, or fluorescing tissue sample constituents. Therefore, many of these optical techniques do not require an exogenous contrast agent (such as a fluorescent dye) to probe tissue sample structure and function. (Wilson et al., 2016).

As powerful tools, optical techniques have been used in environmental monitoring, water and vegetation status assessment and air quality monitoring. The techniques are also used for flying insect identifications via remote sensing. Besides, optical diagnostic techniques have been remotely used for quantifying agricultural and epidemiological importance (Anderson et al., 2004; Svanberg, 2004; Brydegaard et al., 2011). Results from the characteristic and distinctive interaction of each compound with EM radiation makes optical techniques very useful (Milosevic & Berets, 1993).

The numerous advantages of optical techniques particularly apply to nuclear magnetic resonance (NMR), UV-VIS spectroscopy, X-ray emission spectroscopy (XES), Tetrahertz Spectroscopy (TS), Mass Spectroscopy (MS), Atomic Absorption Spectroscopy (ASS) and Fourier transform infrared (FTIR) spectroscopy. Other optical techniques are Attenuated Total Reflectance Fourier transform infrared (ATR-FTIR) Spectroscopy, Absorption spectroscopy (AS), fluorescence spectroscopy (FS) and Raman spectroscopy (RS) which are some of the common measurement techniques for atomic and molecular studies of samples. RS, which is a technique based on inelastic scattering of monochromatic light source, usually from a laser source (Raman & Krishnan, 1928), for example is fast advancing most especially in the field of cellular biology. RS has been used objectively and successfully for discrimination between normal and malignant cells in cancer studies. (Nijssen et al., 2002; Haka et al., 2005; Movasaghi et al., 2007). Other applications of RS are in the study of infected and uninfected red blood cells (RBCs) for early diagnosis of malaria (Carter, 2007; Webster et al., 2008) and mapping of composition of drugs to aid uniformity in batch manufacturing process (Wartewig & Neubert, 2005; Henson & Zhang 2006). RS has also been used for detecting forgery in art work as well as investigating crime in forensics without necessarily destroying evidence (Edwards & Chalmers, 2005; Yang & Ying, 2011).

Atomic Absorption Spectroscopy (AAS) is an analytical technique for measuring concentrations of chemical elements present in samples by measuring the absorbed radiation by the chemical element of interest. Atomic absorption is so sensitive that it can measure parts per billion of a gram (μg dm^{-3}) in a sample (Ning et al., 2011; Yang et al., 2012). The technique makes use of the wavelengths of light that specifically absorb element of interest. There are many applications of AAS due to its specificity and these can be divided into the broad categories of biological analysis, environmental and marine analysis, and geological analysis. AAS can be used to determine the amount of various levels of metals and other electrolytes within tissue samples. AAS has been applied on human hair to measure electrolytes sodium and potassium in plasma (Zhao et al., 2012). In the food industry, AAS provides analysis of vegetables, animal products, herbal tea, wine and animal feed.

The presence of molecular species having energies which are in resonance with the spectra line(s) of the radiation source are investigated with absorption measurement techniques (Knee, 1996). Tunable diode laser absorption spectroscopy (TDLAS), differential optical absorption spectroscopy (DOAS), wavelength modulation spectroscopy (WMS), differential absorption light detection and ranging (LIDAR) and gas in scattering medium absorption spectroscopy (GASMAS) (Sigrist, 1994; Platt & Stutz, 2008) are some of the absorption measurement techniques. Wavelength modulation spectroscopy (WMS) is an extensively used technique for sensitive detection of absorption signals, as it can significantly reduce the low-frequency noise by shifting the detection band to higher frequencies (Kluczynski et al., 2001; Schilt et al., 2003). WMS can provide substantial sensitivity enhancement and noise immunity compared to direct absorption methods (Zhou et al., 2005). The GASMAS technique relies on the fact that the absorption features for free gas are about 10^3 times narrower than the spectra features of the surrounding liquid and solid. This makes it possible to discern the gas. The GASMAS technique opens up new possibilities for characterization and diagnostics of scattering solids and turbid liquids. The GASMAS project emerged from the interaction of diode-laser gas spectroscopy (Kauranen et al., 1994; Gustafsson et al., 2000) with optical mammography (Andersson-Engels et al., 1990; Berg et al., 1993) and differential absorption lidar (Svanberg, 1993; Weibring et al., 2003), which all contain elements of the technique.

Another common optical technique is fluorescence spectroscopy (FS) where the fluorescence emission results from absorption of photon into an atom (Sauer et al., 2010). The technique is very useful and important in the study of biological samples. Fluorescence is the phenomenon where a molecule absorbs photon within its absorption band and then emits this photon at longer wavelengths within its emission band. Fluorescence emission is caused by electronic transitions of atoms and this occurs in the optical region of the EM spectrum. This technique is appropriate for analyzing molecules and can be used to identify, quantify, and observe chemical activity, and it is a popular method due to its high levels of sensitivity, simplicity, and specificity (Lakowicz, 2006). Fluorescence emissions depend on the excitation wavelength. Generally, not all substances do fluoresce for a particular excitation. Fluorescence spectroscopy is a highly sensitive technique whose set-up constitute basic elements such as light source, excitation and emission mono chromators (filters), sample holder, and a detector. The light sources, which are usually lamp, laser or light emitting diode (LED), produces light photons over a broad energy spectra for exciting fluorephores in the sample. Excitation of the sample takes about 10 ns and the fluorescence is measured by the detector. Most of the FS set-up uses laser as a source of excitation to overcome the challenges of stability (De Oliveira Silva et al., 2010; Kalnina et al., 2010; Al-Salhi et al., 2011; Masilamani et al., 2011).

Laser-induced fluorescence (LIF), is (spontaneous) emission from atoms or molecules that have been excited by (laser) radiation obtained with laser-induced fluorescence spectroscopy. The LIF technique which is another type of optical spectroscopic technique analyzes induced fluorescence of samples. The phenomenon of induced fluorescence was first seen and discussed back in 1905 by R. W. Wood, many decades before the invention of the laser (Helmut et al., 2007). When excited by UV/Vis radiation of suitable wavelengths, the fluorescence emission from endogenous fluorescent molecules in living tissue (algae, plant and animal) are observed. This fluorescence emission, called autofluorescence, is an intrinsic property of tissue samples. Autofluorescence emission, by endogenous fluorophores from laser sources is referred to as laser-induced autofluorescence (LIAF) spectroscopy technique. Autofluorescence spectrum therefore provides an accurate fingerprint of these fluorephores. Nevertheless, one must be able to distinguish these intrinsic signals from other fluorescent signals resulting from the addition of exogenous markers (Zimmerman et al., 2003).

LIAF has been extensively studied over the past 20 years and significantly emerged as a promising technology for biomedical diagnostics. This is a process whereby molecules/atoms are excited to higher electronic energy levels via photon absorption and subsequently fluoresce at emission wavelengths, which are independent and longer (red-shifted) than that of the excitation wavelength. It has been applied for the *in vitro* and *in vivo* analysis (Yang et al., 1987) of many different types of samples, ranging from individual biochemical species (e.g. NADH, tryptophan) to human and animal tissues as the associated signal is intense with an excellent signal to noise ratio. This leads to a greater achievable sensitivity (Anidjar et al., 1996; Zheng et al., 2003). This technique has the capability to quickly, non-invasively, and quantitatively probe the biochemical and morphological changes that occur as the tissue transforms from normal to malignant. The altered tissue architecture and bio-characteristics of native fluorophores associated with malignant transformations is reflected in the spectral characteristics of the measured fluorescence. Thus in recent years, laser induced autofluorescence has emerged as a promising tool (Yang et al., 1987; Anidjar et al., 1996; Zheng et al., 2003). LIAF reflects the structural characteristics of endogenous spectra of fluorophores inside tissue (Fauaz et al., 2010). LIAF diagnostic methods have been used to investigate the structural and spectra characteristics of normal and diseased tissues (Bengtsson et al., 2005; Karadaglic et al., 2009; De Goes Rocha et al., 2010; Fauaz et al., 2010).

Laser-induced autofluorescence (LIAF) technique is among the least complicated optical techniques and takes advantage of the fluorescence to provide discrimination between different materials (Ondrej et al., 2014). LIAF technique is emerging as a diagnostic technique to obtain the fluorescence spectra of healthy and pathological tissue samples to evaluate structural difference between the tissue samples which reflect the structural characteristics of endogenous spectra about fluorophores of the tissues (Karadaglic et al., 2009; De Goes Rocha et al., 2010; De Oliveira Silva et al., 2010; Kalnina et al., 2010; Al-Salhi et al., 2011; Masilamani et al., 2011; Peng & Liu, 2013; Opoku – Ansah et al., 2016; Amuah et al., 2017). LIAF, is therefore, an adequate analytical technique with advantages of being rapid, objective, highly sensitive and non-destructive.

Infrared spectroscopy (IR) as identified with optical spectroscopic technique uses excitation sources of relatively longer wavelength (> 700 nm) to provide vibrational information of the molecules present in a given sample (Nakamoto, 1977; Colthup, 2012). Samples are prepared with either Nujul oil or Potasium Bromide (KBr) to avoid the absorption of water which may affect the measured spectra (Harwood et al., 1989). IR spectroscopy requires a special chamber for the experiment to be performed. An infrared spectrum represents a fingerprint of a sample with absorption peaks which correspond to the frequencies of vibrations between the bonds of the atoms making up the material. Because each different material is a unique combination of atoms, no two compounds produce exactly same infrared spectrum. A very common spectroscopic technique which uses infrared radiation as an excitation source is the Fourier Transform Infrared spectroscopy (FTIR).

FTIR spectroscopy is a technique that has undergone rapid development over the past decade with a promise of easier, more rapid, and more objective diagnosis (Diem et al., 2002). FTIR spectroscopy is also an effective and nondestructive technique for monitoring cellular alterations (Griffiths & de Haseth, 1986; Mantsch & Chapman, 1996). Diseases of several organs have been characterized through FTIR spectra analysis, and quantification of different biomolecules such as proteins (Cooper & Knutson, 1995), nucleic acids (Liquier &Taillandier, 1996; Brandenburg & Seydel, 1998), and lipids (Banyay et al., 2003) have also been carried out using this technique. The potential of FTIR spectroscopy in molecular diagnostics relies on its ability to determine and characterize the unique fingerprint of a sample at the biochemical level (Zohdi et al., 2015). The three major spectroscopical sampling modes are transmission, transflection, and Attenuated Total Reflection (ATR). Each mode offers convenience for some samples. ATR is the most widely practiced infrared spectroscopy technique. The reasons for this are fairly straightforward: the technique requires little or no sample preparation, and consistent results can be obtained with relatively little care or expertise. The technique is not fool-proof, but it can be very forgiving (Griffiths & de Haseth, 2007; Lyng et al., 2011). ATR is a technique whereby the sample is placed in contact with a sensing element, and a spectrum is recorded as a result of that contact. Unlike many other sampling techniques used in infrared spectrometry, radiation is not transmitted though the sample. The physical morphology of the sample is usually not a problem, as long as sufficient contact area between the sample and the sensing element can be maintained. (Movasaghi et al., 2008; Baranska, 2014).

Other optical techniques are also applied for imaging of samples. These optical imaging techniques include fluorescence imaging (FI), X-ray imaging (XRI), magnetic resonance imaging (MRI), Slit lamp imaging (SLI) biomicroscopy and multispectral imaging (MSI) microscopy (Kane & Lee, 2007; Frey & Warda, 2008; Demtröder, 2008; 2013; Cosentino, 2013). There are enormous benefits of applying these optical imaging techniques to samples. Most importantly, light can provide exquisite sensitivity to functional changes via intrinsic changes in the optical properties of the sample. Absorbing and fluorescent dyes, as well as cutting-edge transgenic methods, can also provide highly specific optical contrast enhancement. Additional advantages of the optical imaging techniques include the use of non-ionizing radiation and inexpensive instruments. Besides, optical imaging techniques are able to measure a range of functional contrast. The technique can readily be exploited via a wide range of approaches which span from studies of intricate cellular mechanisms of normal and diseased tissues to *in-vivo* non-invasive imaging.

MSI microscopy is a novel and important imaging technique that combines optical spectroscopy with imaging. MSI microscopy is a technique of imaging microscopic samples at more than one spectral band and extracting both physical and chemical information out of the images. The term refers to imaging systems that use a number of non-overlapping discrete spectral bands to highlight certain features within the field of view so that spatial as well as spectra information emanating from microscopic samples can be extracted within the optical region (Hu et al., 2005; Teikari, 2008; Coffey, 2012). It works on the principle that the recorded spectra is over all the spatial locations of the study area. A major advantage for spectral imaging (SI) probes and instrumentation, particularly those targeted towards eventual clinical applications, is overcoming attenuation and scattering of light by tissues. MSI has been used in various applications to extract detailed information about an image (Higham et al., 1975). MSI has been used for quantifying biological process which include biometric pattern recognition, retinal physiology and plant physiology among others. (Contag et al., 1995; Teikari, 2008).

Spectra imaging (SI) has been suggested as a method for non-destructive identification of pigments. The use of SI to tentatively identify pigments has an important advantage of being rapid and low-cost survey of large areas (Frey & Warda, 2008; Teikari, 2008; Brydegaard et al., 2009; Cosentino, 2013). SI has been used for colour analysis, colour constancy, object recognition, digital staining and the analysis of works of art (Hu et al., 2005; Teikari, 2008; Bautista & Yagi, 2011). SI cannot only provide spatial and structural information about a sample, but it can also provide intracellular spectral data (Levenson & Hoyt, 2000; Hu et al., 2005; Park et al., 2007; Teikari, 2008). Spectral imaging has been found useful for investigating tissue irregularities based on the interaction of the EM radiation with the tissue (Bremard et al., 1993; Ong et al., 2002; Wood et al., 2003; 2004; Svanberg, 2004; Somesfalean, 2004). SI is emerging as a powerful technique for diagnosing diseases (Luker & Luker, 2008; De Oliveira Silva et al., 2010; Kalnina et al., 2010; Al-Salhi et al., 2011; Masilamani et al., 2011).

Magnetic resonance imaging (MRI) is an imaging technique that uses a magnetic field and pulses of radio wave energy to produce images of organs and structures inside a body. Imaging of brain tissues has also seen major improvement with the application of MRI (Ogawa et al., 1990; Belliveau et al., 1991; Kwong et al., 1992; Matthews et al., 2006). MRI has been utilized to study signals between oxygenated and deoxygenated blood to indirectly quantify changes in blood flow associated with neuronal activity (Buxton, 2002). It is now possible to study the effects of pharmacological agents, such as alcohol and other drugs, in very small animals such as mice using small animal MRI. (Chen et al., 1997; Benveniste & Blackband, 2002; Van der Linden et al., 2007).

The imaging systems have a unique role in the ophthalmologic routine practice. While imaging has an auxiliary role in other branches of medicine, it is the most essential part of the ophthalmic examination. The slit lamp biomicroscopy is an important tool in ophthalmic practice. It is basically designed for examination of anterior segment but with the appropriate attachments, all ocular structures can be viewed. The most important advantage of Slit Lamp Imaging (SLI) biomicroscopy in examining the eye structures is stereopsis, in other words ophthalmologist can examine eye structures in three dimensions. It is a routine examination tool of most ophthalmologist (Yolcu et al., 2014).

The slit lamp imaging microscopy technique has been used to detect and measure the severity of cataractous lenses. Clinically, cataracts are described as a significant decrease of vision due to irreversible increase in absorption or scattering of light by the lens. (Brown et al., 1993; Antunes et al., 2007: Kapelhof et al., 1986). Cataracts are the major and leading cause of visual impairment worldwide (Thylefors, 1997), accounting for more than half of blindness in developing countries (Xu et al., 2013). Most cataracts are age-related, though they have also been attributed to disease, trauma and congenital factors. With the global trend of aging populations, the prevalence of cataracts is expected to increase. (IAPB Report, 2010). For disease related cataract, it has been attributed to high mineral intake, heavy yoghurt consumption and ultraviolet radiation from the sun (Harding, 1980).

Cataract detection and measurement of its severity is usually performed by an Ophthalmologist through various eye test and grading systems. The final diagnosis is therefore subjective, slow and relatively expensive. The grading system normally employed by Ophthalmologist and Optometrist which uses integer scale includes the Lens Opacities Classification System (LOCS) I-II (Chylack et al., 1988; Chylack et al., 1989), the Wisconsin system (Klein et al., 1990) an adaptation of which became the Age-Related Eye Disease Study (AREDS) system, the Wilmer system (West et al., 1988), the Cooperative

Cataract Epidemiology Study Group (CCESG) system (Sasaki et al., 1997), and the Oxford system (Sparrow et al., 1990) whiles those which use decimal scale includes the LOCS III system (Chylack et al., 1993), and a simplified cataract grading system in the World Health Organization (WHO) cataract grading group (Thylefors et al., 2002).

Even though these grading systems are useful, their subjectivity has a number of disadvantages of which various researcher have tried to address. Fujikado and his team used higher-order aberrations, and light scattering to estimate the visual deterioration of cataractous eyes (Fujikado et al., 2004). Computer-aided (CAD) techniques was employed by Abraham and his team to analyse diagnostic images of cataracts for epidemiological research (Abraham et al., 2009). There have been some attempts towards computerized cataract detection recently (Acharya et al., 2007). To the best of my knowledge, there is no computer aided nuclear cataract grading system using slit-lamp images and based on Integrated Optical density. One of the goals of this work is to computerize this process and provide an objective and repeatable grading system for nuclear cataract evaluation from slit-lamp images. A relatively simple, reliable, and computer aided cataract detection and evaluation technique will greatly reduce treatment costs, enhance health care levels, thus improve quality of life.

During preclinical studies, histopathological evaluation remained the gold standard for discriminating cataractous lenses from healthy ones. This process involves subjective assessment of tissue biopsies / autopsies by Pathologist, which makes it laborious, time consuming and relatively expensive (Okano et al., 1993; Wang et al., 2011; Kyei et al., 2015). Therefore, there is need for relatively simple, objective and non-destructive technique that can provide diagnostic information of the eye lenses.

Considering such limitations, optical and spectroscopic modalities are more rigorous and objective than traditional pathologist interpretation as they provide a quantitative rather than qualitative assessment (Alfano et al., 1984; Feride et al., 2000). Other microscopic techniques which have also been used to discriminate cataractous lenses from healthy ones include Atomic Force microscopy (AFM), Transmission electron Microscopy (TEM), Scanning Electron Microscopy (SEM) (Antunes et al., 2007) and Field Emission Scanning Electron Microscopy (FE-SEM) (Jongelbloed et al., 1998). All these microscopic techniques produce single images on a sample. However multispectral imaging (MSI) provides multiple images on a sample from different excitation light sources and better information than these single imaging techniques. MSI together with techniques such as fluorescence microscopy, point-scanning laser confocal microscopy and photoacoustic microscopy imaging (Rice et al., 2001; Graves et al., 2003; Levenson & Mansfield, 2006; Zhang et al., 2007; Zhang et al., 2011) have been used to optically identify tissue irregularities (Hiraoka et al., 2002; Zhou & El-Deiry, 2009; Sangare et al., 2015). Examples are the identification of precise spectral band(s) for discrimination of infected red blood cells (iRBCs) from uninfected red blood cells (uRBCs) (Opoku-Ansah et al., 2014) and development of rapid multispectral endoscopic imaging system to map mucosa blood supply to the lungs (Fawzy et al., 2015). MSI has also been used in a variety of applications including dentistry, dermatology, and histopathology (Levenson et al., 2008). To the best of my knowledge no studies have been done so far in applying MSI technique in cataract research. Another goal of this work study is to apply MSI in combination with multivariate analysis to study, analyse and discriminate cataractous and healthy lens images of rats. This would be beneficial in veterinary ophthalmology and other ophthalmic applications.

Research has shown the usefulness of LIAF technique in ocular tissue assessment in many areas which includes the navigation on the cornea during eye surgeries (Tuft et al., 1990; Phillips & McDonnell, 1997; Chuck et al., 2004), examination of LIAF of excimer-irradiated pig cornea (Loree et al., 1988) and the fluorescence spectra of bovine and human cornea irradiated at subablative levels have been acquired (Tuft et al., 1990). Zuclich et *al* also used the technique to study the diagnostic capabilities of fluorescence of ocular tissues excited by UV radiation (Zuclich et al., 2005) whiles Maslov et *al* worked on secondary cataract using LIAF with excitation sources in the UV region (210 nm – 350 nm) (Maslov et al., 2016). However, exposure of UV radiation to the eye lens induces cataract and there are series of experimental evidence that show that UV radiation and most especially UVB rays are associated with cataract formation (McCarty & Taylor, 2002; Okuno et al., 2012; Zoris & Stojcic, 2013). In my view, the use of a safer light source to detect and discriminate cataractous lenses from the healthy ones will be a great improvement in reducing the inherent risk involved in the use of emerging diagnostic approach. This study therefore uses 405 nm and 445 nm as excitation sources for the LIAF technique to detect and discriminate cataractous lenses from the healthy ones.

In order to determine the health status of lens tissues there is the need to obtain some biophysical information. There is therefore the need for relatively simple and objective technique that can provide biophysical information. ATR-FTIR has been established as a powerful and objective technique to characterize, identify and quantify substances (Marc-Michael & Harald, 2012). So far ATR-FTIR has not been used for cataractous lens research. This study is also undertaken to investigate the possible application of ATR-FTIR to distinguish, discriminate and classify cataractous lens tissues from healthy ones. In spite of all these advances, no research work has focused on combining different optical techniques to study and characterize the cataractous lenses using animal model.

Scope of Study

Overall Purpose

Generally, this work seeks to apply four (4) optical techniques: Slit lamp microscopy, multispectral imaging (MSI), laser – induced autofluorescence (LIAF) and Attenuated Total Reflectance Fourier Transform infrared (ATR-FTIR) spectroscopy to study and characterize cataractous lens tissues from the healthy ones. Stained and unstained sectioned lens tissues, henceforth known as SSLT and USLT will be prepared for MSI technique. The cataractous and healthy lens tissues will be obtained from Sprague –Dawley rats. In addition, digital slit lamp microscopy will be employed to assess the severity of cataractous lenses as they develop from mild through to severe.

Specific Purpose

First and foremost, the aim of this work is to conduct feasibility studies on the cataractous and healthy lens tissues from the Sprague- Dawley rats employing LIAF technique. This is to aid discrimination and classification of cataractous lens tissues from the healthy ones with laser light sources in the visible region.

More so, the work aims at applying digital slit lamp microscopy technique for characterizing cataractous lenses of Sprague-Dawley rats by assessing the severity of the cataract as it develops from mild to severe. Integrated optical density (IOD), with the aid of *Image Pro Plus 5.0* software, will be retrieved from the slit lamp images containing the cataractous lenses.

Furthermore, the work seeks to discriminate stained and unstained sectioned cataractous lens tissues from the healthy ones by finding spectral bands that can be used as markers for discriminating cataractous sectioned lens tissues from the healthy. This will be achieved with the help of MSLEDIM system which captures spectral images in transmission, reflection and scattering modes.

The work finally employs infrared technique to study infrared spectra of both cataractous and healthy lens tissues. This will aid in objective discrimination and classification of the cataractous lens tissues from the healthy ones by finding wavenumbers that can be used to identify the cataractous lens tissues and the healthy lens.

Organization of Study

This thesis consists of five main chapters. Chapter one gives an introduction to optical techniques, cataractous lens tissues discrimination from the healthy ones and their associated challenges, optical solutions and the related concepts as well as applications to multispectral image acquisition. The purpose of the work and the arrangement of the thesis are also included in this chapter. Chapter two reviews literature on light-tissue interaction principles, optical spectroscopy and its concepts, optical microscopy, digital slit lamp microscopy, spectral imaging, the crystalline lens, cataract as well as the principle underlying the experimental techniques used in this work.

Chapter three looks at the experimental methods and procedure for the research work. Results, analysis and discussions from digital slit lamp images, multispectral images, laser-induced autofluorescence excitation spectra and infrared spectra are presented in Chapter four. In the fifth chapter, conclusions are drawn and relevant recommendations given to assist in further research.

Chapter Summary

This chapter has discussed the background to optical spectroscopic techniques such as multispectral imaging, digital slit lamp microscopy, Laser – induced autofluorescence spectroscopy, infrared spectroscopy and related concepts. The background to cataractous lens tissues discrimination from the healthy ones and their associated challenges which led to the problem statements was also discussed. The purpose of the study and the arrangement of the thesis were also included in this chapter.

CHAPTER TWO

LITERATURE REVIEW

Introduction

Important information for characterization and diagnostics purposes can be obtained in many applications by studying light that has interacted with matter. This is due to the fact that every atom and molecule has its unique way of interacting with matter. In this chapter, discussion will be made on different processes that may occur when a beam of light propagates in and interact with matter. Some basic principles concerning light are presented as a start. This is followed by literature review on optical spectroscopic techniques used to characterize different materials and or samples. The last part discuses review of data analysis techniques, the crystalline lens and cataract.

Interaction of Light with Tissue

The resultant spectrum measured as a result of interaction of light with tissue is the combined effect of the properties of the light source and the characteristics of the tissue. Fundamentally, the outcome of the interaction of light with tissue depends on the wavelength of the light and the dimensions of the particles involved in the interaction. These particles can be of atomic size to complex molecule in the case of biological materials.

For biological materials, the tissue type and the state as well as the medium of the biological sample primarily influence the optical properties of the sample. Therefore, these optical properties are used to characterize light propagation through these materials. In general, when the light source is monochromatic in nature, for example a diode laser, the variables involved in the light-tissue interaction process are limited.

There are several factors that influence light-tissue interaction. The power density provided by the source is considered one of the main factors. The amount of source power coupled into the medium under irradiation is a function of the light power output. At a constant power density, that is, the power per unit area, the radiant fluence rate in the sample at the core of the spot size increases with the spot size.

When a beam of photons incidents on the tissue surface at an angle, a progressively higher percentage of photons will be reflected off the surface at an increasing angle of oblique incidence. Generally, when light impinges on a tissue, it can be reflected back towards the source, refracted or scattered, and results in a change in the angle of propagation, absorbed by the molecules in the sample, or transmitted. Figure 1 shows some possible interactions between light and tissue. Depending on the specific material one or two of these dominate over the other.

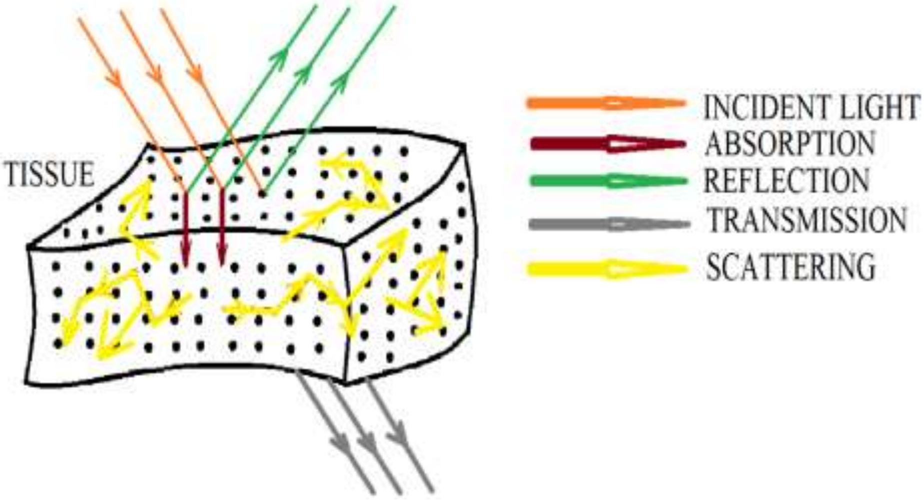

Figure 1: Some Possible Interactions (Reflection, Transmission, Absorption, and Scattering) between Light and Tissue.

Optical properties are different for distinctive biological tissues, and these differences are not always distinguishable by visual examination. The optical parameters are in fact a function of delivery protocol of the light source, tissue composition, temperature and water content of the tissue. Different tissue and its constituents will interact with light according to specific optical parameters, and require individual attention in the classification of these optical properties.

Reflection is the change in direction of light at an interface between two different media so that the light returns into the medium from which it came. Reflection of light is either specular (mirror-like) or diffuse (retaining energy, but losing image of original medium) depending on the nature of the boundary. Generally, a certain fraction of the light is reflected from the boundary and the remainder is refracted.

When light travels in an incident medium with same speed, one part of the law of reflection is given as:

$$\theta_i = \theta_r \tag{1}$$

where θ_i is the angle of incidence and θ_r is the angle of reflection. Thus, angle of incidence equals angle of reflection.

Transmission of light through a medium is a repetitive process of scattering and re-scattering. Such event introduces a phase shift into the light field, which ultimately shows up as a shift in the apparent phase velocity of the transmitted light from its nominal value of speed of light of the medium. The transmittance (T) of light, with incident intensity I_0 and transmitted intensity I is given as:

$$T = {}^{I}/_{I_0} \tag{2}$$

i.e. the fractional intensity of the original light detected.

In general, variables involved in the light-matter interaction process are limited when the light source is monochromatic in nature. When light irradiation reaches the medium surface at an angle, a progressively higher percentage of light will be reflected off the surface at an increasing angle of oblique incidence.

Absorption is one of the three distinct processes that attenuate light incident on a material. It is the transformation of light energy into some other forms of energy as it moves through matter. Energy at certain frequencies or wavelengths are absorb by atoms and molecules of matter. The unique nature of every atom or molecule which leads to unique set of absorption lines makes identification of a gas possible using absorption analysis. (Svanberg, 1992; Somesfalean, 2004).

Scattering of light radiation is the deflection of light in random directions by particles in a medium, or in the interface between two media with different refractive indices. Scattering may be due to surfaces which can be described as troughs and valleys that are slightly larger than the incident wavelength. Scattering often can occur when light travels in transparent solids and liquids, but is more prevalent in gases. Bubbles, impurities and inhomogeneities in a medium can also cause scattering (Katzir, 1993).

Light can be scattered by a sample if its wavelength does not match the energy-level transitions of atoms and molecules. Elastic scattering of light occurs when charged particles in a medium are set into oscillatory motion by the electric field of the incident wave, and re-emit (as opposed to absorb) light of the same frequency as the primary wave. Thus if the wavelength of the scattered light is equal to the wavelength of the incident light. Inelastic scattering on the other hand occurs if the wavelengths differ. Thus, for inelastic scattering, energy is transferred between the incident light and the particles in the medium. Rayleigh and Mie scattering are elastic, while Raman scattering is inelastic. Scattering occurs at non-resonance frequencies. Hence, the scattered intensities are relatively weak since the forced vibrational amplitudes of the particles are much smaller than those at natural resonances. In most solids and liquids, however, intermolecular interactions broaden the absorption frequencies such that both scattering and absorption of light occur at all wavelengths.

As a result of scattering, the velocity of light in all tissue is less than it is in vacuum. In an optically dense or homogeneous medium, i.e. one in which the molecular separation is much smaller than the wavelength of the incident light, individual atoms or molecules in a medium will scatter the incident radiation in all directions. The phase difference of the scattered light relative to the primary wave will depend on the frequency of the primary wave. In any direction the total scattered field is then a superposition of all the scattered wavelets propagating in that direction.

The scattered light will interfere with the incident light, modifying its phase and hence the velocity of the light through the medium. The refractive index (RI) of a medium is given by

$$n = \frac{c}{v} \qquad (3)$$

where c is the speed of light in vacuum and v the speed of light in the medium. The refractive index depends on the number of molecules per unit volume and their polarizability, since the total scattered light that interferes with the incident light depends on the amplitudes of, and phase relations between, the individual scattered wavelets.

Furthermore, refractive index for a given medium, changes with the frequency of the incident light. This phenomenon is known as dispersion and is due to the frequency-dependence of the relative phase change between the incident and scattered light. Theory has shown, however, that to explain dispersion in real media over a broad spectrum, including the resonance frequencies, the absorption of light must also be considered. Thus, the complex refractive index is defined as:

$$N = n + ik \tag{4}$$

where the real part, *n*, as defined in equation (4), determines the speed of the light and the imaginary part, *k*, determines the absorption of the light as it propagates through the medium. From Maxwell's equations *k* can be related to the absorption coefficient μ_{abs} as follows:

$$k = \frac{\mu_{abs}\lambda}{4\pi} \tag{5}$$

Various theories have been put forward to describe the scattering of light by particles of different shapes and sizes. In general, these fall into two categories: single scattering and multiple scattering theories. In single scattering theory it is assumed that the particle separation is sufficiently large, or the number of particles are sufficiently small, such that the total scattered light due to all the particles is small compared to the incident light (Van de Hulst, 1981; Bohren & Huffman, 1983). In other words, the assumption is that the particles do not further interact with the light that has been scattered from neighbouring particles.

Single scattering by particles small in diameter compared to the wavelength of the incident light is often known as Rayleigh scattering. When unpolarised light is incident on a small particle the intensity distribution of the scattered light is almost isotropic, since the secondary wavelets emitted by the oscillating charges are approximately in phase with one another. At an angle of 90^o to the direction of propagation of the incident light, however, the charges oscillate linearly in one direction only, and thus the light appears to an observer to be linearly polarized.

According to Stark effect, an electric dipole moment P is induced in a polarized particle if the particle is subject to an electric field of resultant amplitude (E), initial amplitude (E_o), frequency (ν) and time (t). As shown in equation 6, the polarization will vary at the frequency.

$$E = E_o \sin(2\pi \nu t) \tag{6}$$

The total radiated intensity of Rayleigh scattered light, I is of the form

$$I = \frac{16\pi^4 c\alpha^2 E_o{}^2}{3\lambda^4} \tag{7}$$

where α is the polarizability tensor, c is the speed of light and λ is the wavelength of light source (Svanberg, 1992; Vo-Dinh, 2003). Equation 7 shows that the intensity of Rayleigh scattered light is inversely proportional to the fourth power of wavelength of light source.

The most important aspect of Rayleigh scattering is its wavelength-dependence, which varies with the inverse fourth power of the wavelength of the illuminating light. Determining the scattered field patterns from particles that are large compared to the wavelength of the illuminating light is an enormously complex task, due to the significant phase differences between the scattered wavelets which must be taken into consideration. However, various approximations can be made to simplify the problem, as is the case in Rayleigh-Gans theory (Rayleigh, 1881). In this formulation, the large particle is theoretically split up into many small particles. It is then assumed that the scattered field from each particle of a smaller size is completely independent of the scattered fields from all the others, i.e. as described by Rayleigh scattering.

The scattered wavelets from individual particles will interfere with another and the theory must take account of the phase differences, relative to some common origin, between them. Provided the small particles are identical in terms of their size, shape and orientation, it can be shown that all wavelets propagating in the forward direction, i.e. the direction of propagation of the incident beam, are in phase with one another (Bohren & Huffman, 1983). Hence, the amplitudes of the scattered wavelets simply sum to give the total scattered field amplitude in the forward direction. In all other directions constructive and destructive interference will occur.

If particles are much larger than the wavelength of the incident light, the process is called Mie scattering. This form of scattering describes spherical particles. Mie scattering is not strongly wavelength dependent. The intensity of Mie scattered light varies from λ^{-4} in the Rayleigh limit to about λ^{-2} for large particles. Mie theory exactly describes both absorption and scattering by a spherical particle of arbitrary radius and refractive index (Mie, 1908). The analysis involves the formal solution of Maxwell's electromagnetic theory for homogeneous spheres using the appropriate boundary conditions (Van de Hulst, 1981; Bohren & Huffman, 1983), which in the limit of a small particle reduces to the relatively simple solution for a Rayleigh scatterer. As with the Rayleigh-Gans theory, the scattering is most intense in the forward-direction. However, unlike the Rayleigh-Gans scatterer, the amplitudes of the scattered wavelets in any direction will never be exactly the same, due to the inclusion of absorption effects, therefore complete destructive interference cannot occur.

In the case of single scattering, therefore, a new exponential relationship can be defined for the collimated-beam intensity I, relative to the incident intensity I_o, transmitted through a distance l of an absorbing medium in which only single scattering occurs

$$I = I_o e^{\mu_t l} \tag{8}$$

where μ_t is the total attenuation coefficient, given by

$$\mu_t = \mu_{abs} + \mu_s \tag{9}$$

and μ_s is the scattering coefficient, the probability that a photon will be scattered per unit length. The reciprocal of the total attenuation coefficient, μ_t^{-1} is known as the mean free path, and is the distance travelled by a photon between interactions. In reality, there are many systems for which the assumption that the particles are independent of one another is invalid and multiple scattering becomes important (Ishimaru, 1978).

Absorption Spectroscopy

Absorption spectroscopy is an analytical technique based on measuring the amount of light absorbed by a sample at a given wavelength. Absorption spectroscopy, particularly in the UV and Vis portions of the EM spectrum, is one of the most versatile and widely used techniques. This is concerned with the measured absorption of radiation in its passage through a gas, liquid or solid. The wavelength region generally used is from 190 nm to about 1000 nm, and the absorbing medium is at room temperature (Andor technology, 2006). Absorption of a photon results in a change of the electronic energy accompanied by changes in the vibrational and rotational energies. Each vibronic transition, i.e. a particular electronic plus vibrational transition, corresponds to an absorption band consisting of rotational lines. In liquids and solids, the rotational lines are broad and overlap so that no rotational structure is distinguishable.

Absorption of light is the way by which energy of a photon is taken up by matter, typically by the electrons of an atom (Anderson & Parrish, 1981, Bersha, 2010). The absorbed light energy is transformed to other forms of energy such as heat in the medium. The spectra distribution of light due to the absorption process depends on the distribution, concentration and absorption spectra of the absorptive elements. Atoms and molecules of matter absorb energy at certain frequencies or wavelengths. If the photon energy, its frequency and wavelength, is suitable to the atom or molecule, it may absorb the energy and get excited (Svanberg, 1992; Somesfalean, 2004).

An absorption spectrum is the result of electronic, vibrational, and rotational transitions. The spectrum maximum (the peak) corresponds to the electronic transition line, and the rest of the spectrum is formed by a series of lines that correspond to rotational and vibrational transitions. Therefore, absorption spectra are sensitive to temperature. Raising the temperature increases the rotational and vibrational states of the molecules and induces the broadening of the recorded spectrum.

The profile of the absorption spectrum depends extensively on the relative position, which depends on the different vibrational states. The intensity of the absorption spectrum depends, among others, on the population of molecules reaching the excited state. The more the number of molecules, the higher the intensity of the corresponding absorption spectrum will be. Therefore, recording absorption spectrum of the same molecule at different temperatures should yield, in principle, an altered or modified absorption spectrum. A spectrum is characterized by its peak position (the maximum), and the full width at half maximum (FWHM), which is equal to the difference

$$\delta\nu = \nu_2 - \nu_1 \tag{10}$$

where ν_1 and ν_2 correspond to the frequencies that are equal to half the maximal intensity.

Absorption of light by a medium is directly correlated to the frequency of the incident radiation and the absorption coefficient of the medium. A medium with a high coefficient of absorption will absorb a large amount of light if the wavelength of the incident light corresponds to the absorption band of the medium. Conversely, light can propagate a long distance without or with very little absorption in a medium with a low absorption coefficient.

When light radiation is incident on tissue composed of discrete electrical charges, the charges are forced to oscillate at the frequency of the incident electric field. The range of frequencies covered by radiation in the electromagnetic spectrum is comparable to the natural frequencies at which atoms or molecules will vibrate in the absence of an applied field. Thus when the radiation is incident on a system of tissue, resonance will occur around the natural frequencies, whereby energy is transferred from the incident field to the system and its amplitude of vibration is greatly increased.

A relationship between the absorption of light in a purely absorbing medium and the thickness of the medium was first determined by Bouguer (Bouguer, 1729). Some years later Lambert (Lambert, 1760) derived the following mathematical expression for the relationship, known as the Lambert-Bouguer law:

$$\frac{dI}{I} = \mu_{abs} dl \tag{11}$$

which describes how each successive layer dl of the medium absorbs the same fraction dI/I of the incident intensity I for a constant μ_{abs}, the latter known as the absorption coefficient with units of inverse length (usually mm^{-1}). For an incident intensity I_o, therefore, the transmitted intensity I through a distance l will be

$$I = I_o e^{-\mu_{abs} l} \tag{12}$$

The absorption coefficient μ_{abs} can thus be interpreted as the probability that a photon will be absorbed by the medium per unit length. The reciprocal of the absorption coefficient, known as the absorption length, is the distance required for the intensity of the beam to fall to e^{-1} of the initial intensity. When equation (12) is expressed in base 10 logarithms

$$I = I_o 10^{-\beta l} \tag{13}$$

then the constant β is known as the extinction coefficient. The absorbance of the medium is defined as the $\log_{10}$ ratio of the incident and transmitted intensities

$$A = \log_{10}\left(\frac{I_o}{I}\right) = \beta l \tag{14}$$

where the unit of absorbance is the optical density (OD). Hence, the units of β are OD per unit length (usually ODcm^{-1}). The extinction coefficient and the absorption coefficient are conceptually the same, differing only by the base of the logarithm used in the Lambert-Bouguer expression. For the same unit length, therefore, the extinction coefficient is related quantitatively to the absorption coefficient by a factor of 0.434. In 1852, Beer determined that the absorption coefficient of a compound is linearly related to its concentration c diluted in a non-absorbing medium (Beer, 1852)

$$\mu_{abs} = \alpha c \tag{15}$$

where α is known as the specific absorption coefficient. Substituting for μ_{abs} in equation (12) gives what is known as the Beer-Lambert law

$$I = I_o e^{-\alpha c l} \tag{16}$$

Expressing the Beer-Lambert law in $\log_{10}$ gives

$$I = I_o 10^{-\varepsilon c l} \tag{17}$$

where ε is the specific extinction coefficient, usually expressed in units of ODcm^{-1}mM^{-1}.

There are many compounds in biological tissues which absorb light radiation, collectively known as tissue chromophores, each of which has its own unique spectrum. The total extinction coefficient of a mixture of compounds is equal to the sum of their individual extinction coefficients, weighted by their relative concentrations. Therefore, approximating tissue as a homogeneous mixture of compounds, the overall light absorption in tissue at a given wavelength depends on the type and concentration of chromophores present.

Mathematically, if the energy of the incident flux is normalized to 1, then the absorbance (A), reflectance (R), scattering (S) and transmittance (T) sum up to unity as expressed in equation 18 (Palmer & Grant, 2009):

$$A + R + S + T = 1 \qquad (18)$$

In general, a measure of A, R, S and T of the incident light depend on the wavelength of the incident radiation. Thus, these four processes can either be quantified for a monochromatic radiation or for a polychromatic radiation. In addition, the A, R, S and T of the incident light might also depend on polarization and geometric distribution of the incident radiation, which has to be specified.

Fluorescence Phenomenon

Fluorescence is the process of absorption of light of a short wavelength which results in emission of light at a longer wavelength. This emitted light is called fluorescence, as certain molecules (fluorophores) de-excite electronically from higher energy level to a lower energy level (Anil &Anand, 2007; Walsh & Shakibaie, 2007). Fluorescence occurs if the transition is between states of the same electron spin and phosphorescence if the transition occurs between states of different spin. The fluorescence energy is higher than that of phosphorescence.

Intensity of emitted light depends on a number of factors, including intensity of incident exciting light (the more powerful the exciting light, the stronger the emitted fluorescence intensity). Fluorescence spectra often give detailed information on fluorescent molecules, including their conformation, binding sites, and interactions within cells and tissues. Fluorescence intensity can be measured as a function of either the emission wavelength or the excitation wavelength. The fluorescence emission spectrum $I_F(\lambda)$, which is specific for any fluorophore is commonly used in fluorescence diagnostics (Bigio & Mourant, 1997)

Chemical compounds are known to absorb energy which causes excitation of electrons bound in the molecule, such as increased vibrational energy or, under appropriate conditions, transitions between discrete electronic energy states. For a transition to occur, the absorbed energy must be equivalent to the difference between the initial electronic state and a high-energy state.

Usually Jablonski energy diagram such as that presented in Figure 2 is used to represent fluorescence and phosphorescence phenomena of a molecule. These energy levels include the ground electronic state (S_0) and higher energy electronic states (e.g., S_1, S_2) reached upon the absorption of light and are represented by thick lines. Each electronic state of a molecule also contains numerous vibrational and rotation energy levels that fully describe the energetic electronic state of the system and is represented by thin lines in the Figure. The absorption of a photon excites the fluorophore from its electronic ground state (S_0) to upper electronic states (S_1, S_2). The exact vibrational and electronic level reached will depend upon the energy content of the light absorbed. Regardless of the excited level reached, the molecule will rapidly lose energy to its environment through non-radiative modes (internal conversion) and will revert to the lowest vibrational level of the lowest electronic excited state.

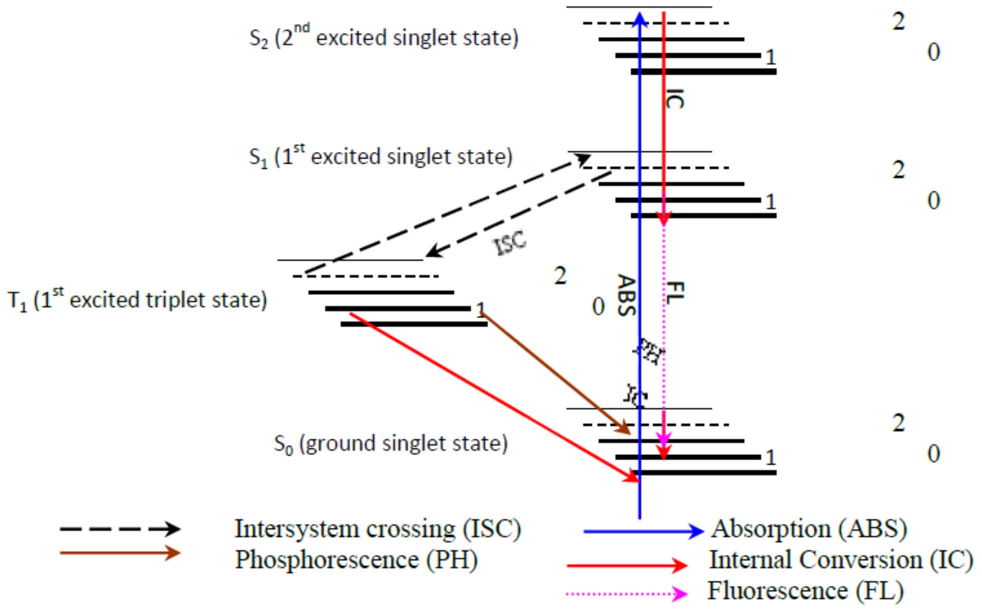

Figure 2: Jablonski Energy Diagram of Fluorescence and Phosphorescence Molecular Processes (Hof et al., 2005; Anil &Anand, 2007).

The transition from this state to the ground state may be accompanied by the emission of a photon with energy in the process called fluorescence emission. A molecule may persist in this lowest level of the S_1 state for a period of time known as the fluorescence lifetime, which, for most fluorophores of interest in tissues, are in the range of several nanoseconds to a few tens of nanoseconds. Many naturally occurring substances fluoresce, including minerals, fungi, bacteria, keratin, collagens and other components of body tissue; this is termed primary fluorescence or autofluorescence.

Absorption and fluorescence do not require any spin reorientation. However, intersystem crossing and phosphorescence require a spin reorientation.

Therefore, absorption and fluorescence are much faster than phosphorescence. Absorption occurs within a time equal to 10^{-15} s, and the fluorescence lifetime goes from 10^{-9} s to 10^{-12} s. Phosphorescence is a long transition that can last from milliseconds to seconds, minutes, or even hours.

The absorption spectrum occurs from the ground state. Therefore, it will characterize the electronic distribution in this state. Fluorescence and phosphorescence occur from excited states, and so they are the mirrors of electronic distribution within the excited states. Any modification of the electronic distribution in these states, such as in the presence of a charge transfer, will modify the corresponding spectrum. One such example is the reduction of cytochromes. The addition of an electron to the ground state, for example, modifies the electronic distribution within the molecule affecting the absorption spectrum. Emission (E) occurs from a population of n excited fluorophores with intensity I as seen in equation 19.

$$I = nE \tag{19}$$

The emission lifetime is within the picosecond-to-nanosecond range. In order to observe fluorescence emission, the fluorophore should be excited continuously since the emission is a very fast process.

Temperature variation induces modification of global and local motions of the fluorophore environment and of the fluorophore itself, modifying its fluorescence emission feature. The intensity, position of the emission wavelength, and lifetime are some of the observables that will characterize a fluorophore. Each fluorophore has its own fluorescence properties and observables. These properties are intrinsic to the fluorophore and are modified with the environment. A fluorescence spectrum is the plot of the fluorescence intensity as a function of wavelength as shown in Figure 3.

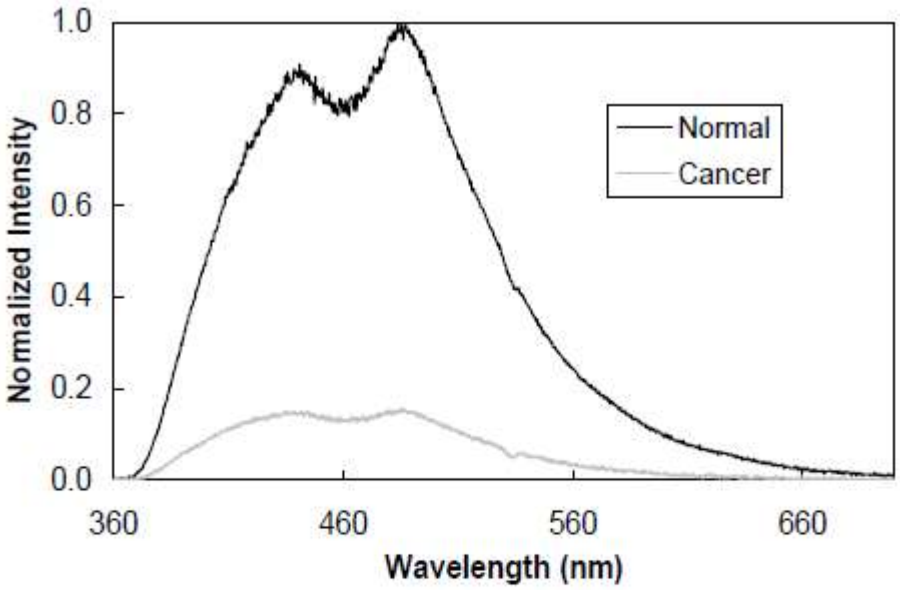

Figure 3: Typical Fluorescence Emission Spectrum from a Normal and Cancerous Liver Tissue.

Most natural and artificial samples exhibit autofluorescence or endogenous fluorescence, that is, fluorescence from natural fluorophores (Svanberg, 2004). Fluorescence spectra from natural molecules are very complex and the contributions from the different fluorophore can usually not be separated. Different excitation light sources may decrease the overall intensity of the fluorescence spectrum without changing its shape. Naturally, the shape of the spectrum depends on the excitation wavelength, since this determines what energy transitions in the fluorescence are possible.

Several other relaxation pathways that have varying degrees of probability compete with the fluorescence emission process. The excited state energy can be dissipated non-radiatively as heat. The excited fluorophore can also transfer energy to another molecule in different types of non-radiative process, such as quenching and photo-bleaching. The two phenomena are distinct in that quenching is often reversible whereas photo-bleaching is not.

Quenching arises from a variety of competing processes that induce non-radiative relaxation of excited state electrons to the ground state, which may be either intra-molecular or inter-molecular in nature. Most quenching processes act to reduce the excited state lifetime and the quantum yield of the affected fluorophore and thus lower fluorescence emission dramatically or, in some cases, completely eliminate it. A common example of quenching is observed with the collision of an excited state fluorophore and another (non-fluorescent) molecule in its environment, resulting in radiationless deactivation of the fluorophore and its return to the ground state. In most cases, neither of the molecules is chemically altered in the collisional quenching process. The mechanisms for collisional quenching include electron transfer, spin-orbit coupling, and intersystem crossing to the excited triplet state.

A second type of quenching mechanism, termed static or complex quenching, arises from non-fluorescent complexes formed between the quencher and fluorophore that serve to limit absorption by reducing the population of active, excitable molecules. This effect occurs when the fluorescent species form a reversible complex with the quencher molecule in the ground state, and does not rely on diffusion or molecular collisions. In static quenching, fluorescence emission is reduced without altering the excited state lifetime. A fluorophore in the excited state can also be quenched by a dipolar resonance energy transfer mechanism when in close proximity with an acceptor molecule to which the excited state energy can be transferred non-radiatively. In some cases, quenching can occur through non-molecular mechanisms, such as attenuation of incident light by an absorbing species, including the fluorophore themselves.

Fluorescence from fluorophores is studied either by varying the excitation wavelength while detecting the emissions at a fixed wavelength, producing excitation spectra, or by a fixed excitation wavelength and the fluorescence being detected at different wavelengths, resulting in fluorescence emission spectra. Excitation spectra can be helpful in indicating the most appropriate wavelength (Lakowicz, 1999), in laser-induced fluorescence studies.

Laser – Induced Fluorescence Spectroscopy

Laser-Induced Fluorescence (LIF) is the fluorescence emission from atoms or molecules that have been excited to higher energy levels by absorption of laser light. In the laser-induced fluorescence technique, a laser is tuned to the allowed dipole transition from a lower to an upper state of the fluorophore under consideration, and the fluorescence that is emitted during the subsequent decay is observed. Laser-induced fluorescence methods can make use of pulsed or continuous lasers for steady state and dynamic processes.

Lasers with wavelength ranging from UV to visible have been used in both laboratory and field fluorosensors or fluorometers (Svanberg, 2004). With the advent of the diode lasers, these fluorosensors have become compact for easy handling especially in areas such as environmental protection, medical or agricultural technologies (Lang et al., 1995; Barócsi et al., 2000; Gustafsson et al., 2000; Anderson et al., 2004). Fluorosensors using diode lasers have now become relatively inexpensive compared to the conventional ones, which use excitation sources like Nd:YAG lasers and nitrogen lasers.

Diode laser as a source has been widely applied on biological materials for assessments and diagnostics in recent times. This is due to the fact that diode lasers enable sensitive detection of photophysical parameters, which are very difficult to assess with conventional techniques using lamps. Methods based on laser measure the optical parameters of the biological materials in their natural environment avoiding the influence of the measurements on the measured parameter. Several optical-based analytical methods have been developed using diode lasers. The spectra quality and high intensity of diode laser light aid in highly sensitive detection of various substances.

Diode laser have shown some promising application with great advances in their development. One of these is the use of diode lasers as light sources for spectroscopic applications. The small size and high operationability of diode lasers are paving way for a new generation of compact, portable and relatively inexpensive sensors. These sources have been used for chemical species detection, gas sensing and temperature. Other areas of application include velocity, pressure, mass flux, combustion, atmospheric sciences and medicine.

Diode laser-based spectroscopy applies the concept of the interaction of light with matter on the principle that every atom and molecule may absorb and or scatter or emit light. Such phenomena tend to associate specific characteristic spectra features of the material under study to enable the atom or molecule in the material to be identified. Important information on the properties of the atoms or molecules in that medium, thus the material, can be gained for diagnosis, characterization, discrimination and classification of the material for subsequent applications in diverse fields.

The reason for the success of the diode laser-based spectroscopic techniques is that laser light has a number of spectacular properties that make it useful for detection of atoms and molecules in solid, liquid and especially gas phase. The most important attribute of diode lasers for spectroscopic applications is that it often has a narrow frequency width. Of special importance is their ability to detect the presence of small or unknown concentrations of species in gas phase under various types of conditions. There are a number of diode laser-based techniques that have been developed during the past two to three decades and the general denominator is their high sensitivity and selectivity.

The narrow frequency width is the basis for the high species selectivity that laser techniques possess. Another is that it has a high directionality with the aid of a lens system. This implies, among other things, that it can be sent over long distances, as is done in techniques for probing the atmosphere, or focused down to micrometer-sized spots. Additionally, there are safety advantages in non-invasive sampling and the use of fibre optics light transmission so that the monitoring and control of equipment can be kept at a safe location. In order to be able to run a given instrumentation under optimum or at least suitable conditions, one has to have a good understanding of the underlying mechanisms of the techniques. This is indeed a matter of crucial importance for the applicability and reliability of the techniques.

The wavelength of all individual diode lasers can be slightly tuned by temperature and current control. The tuning range depends on the laser materials and structure. Due to the linewidth and limited tunability additional optical techniques are normally required for their application as spectroscopic light sources. Several techniques have been developed in order to operate the diode laser in a single mode with narrow linewidth and to extend the tuning range.

For spectroscopic purposes, especially absorption spectroscopy, in the NIR the detection sensitivity decreases because weaker vibrational transitions are detected. However, this is outweighed in many cases by the tremendous practical advantages of easy to use, robust, reliable devices operating at room temperature with relatively high output emission power and at a single discrete wavelength. In addition, inexpensive spectrometer components can be used. The very narrow wavelength spread of the light emission can ensure that interferences from other transitions are negligible. The ability to directly vary the output emission, that is, by modulation in order to improve detection sensitivities, also remains as a technical advantage. Due to its low demand on systems and samples, fluorescence spectroscopy has been one of the most used optical methods for analysis. After the absorption of photons, the excited molecule emits a characteristic fluorescence spectrum. Like a fingerprint, it allows a differentiated statement about the fluorescing molecule.

Fluorescence has numerous measurement aspects, including intensity and excitation wavelength dependence, and quantities such as fluorescence decay time, anisotropy, polarization conditions, quantum yields and Stokes' shifts, which can be accessible for analysis. These parameters for the detection of substances allow alleviating some difficulties which may occur when applying fluorescence spectroscopy, for example, matrix and quenching effects. There are also cases where one parameter may give little or no information at all; in this case, other parameters may be used. However, there are substances which show an extremely low fluorescence yield or even no fluorescence at all due to other fast decay pathways such as intersystem crossing. The major advantage of *in situ* laser-Induced fluorescence (LIF) measurements is absence of sampling and sample preparation procedures preceding the analysis. Such procedures are error-prone, time consuming and expensive. A general concept for *in situ* analysis is to increase the dimensionality of the measured data. Since the substances have to be analyzed in a complex matrix and in the presence of other interfering compounds, higher information content is crucial for a subsequent analysis since there is no clean-up step and no separation involved. Therefore, the LIF system should be able to record multi-dimensional fluorescence data, for example, fluorescence intensity versus emission wavelength and time.

Infrared Spectroscopy

Infrared spectroscopy is the spectroscopy that deals with the infrared region, 14000 cm^{-1} (714 nm) to 10 cm^{-1} (1×10^6 nm), of the electromagnetic spectrum. Moreover, the IR portion of the electromagnetic spectrum is divided into three regions; near infrared, mid-infrared and far-infrared. The near-infrared energy, approximately in the region between 14000-4000 cm^{-1}, can excite overtone or harmonic vibrations (Workman, 2011). The mid infrared energy, approximately in the region between 4000 cm^{-1} (2500 nm) to 400 cm^{-1} (25000 nm), can be used to study the fundamental vibrations of structures. The far-infrared region, approximately in the region between 400-10 cm^{-1}, can be used to study rotations of structures (Heise et al., 1998). With IR spectroscopy, different functional groups adsorb at different IR bands or regions Thus, this technique can help identify and even quantify organic and inorganic molecules.

The infrared spectrum of a sample can be obtained by passing a beam of infrared light through the sample. A Fourier transform instrument can be used to measure how much energy was absorbed by the sample over the entire wavelength range. The interferometer is a fundamentally different piece of equipment compared to a monochrometer. The beam of light incident on a beam splitter reflects and transmit IR light equally. The collimated beam of light from the IR source is partially reflected (50 %) to a fixed mirror and partially transmitted (50 %) to a movable mirror. The two IR beams are then reflected back to the beamsplitter by the mirrors. The recombination of the two beams at the beamsplitter causes the combined beam to interfere constructively or destructively depending on the wavelength of the IR source. A mathematical function called a Fourier transform converts an intensity-vs.-time spectrum into an intensity-vs.-frequency spectrum. This can be explained with equation 20 where A(r) and x(k) are the frequency domain and time domain points, respectively, for a spectrum of N points (Smith, 1996).

$$A(r) = \sum x(k) exp^{\left(-2\pi\frac{ikr}{N}\right)} \qquad (20)$$

Fourier Transform Infrared Spectroscopy

Fourier transform infrared spectroscopy is a non-dispersive method of infrared spectroscopy. The original infrared spectrometers were “dispersive,” meaning that the instruments separated individual frequencies of energy emitted from the infrared source via the use of a prism or grating. After passing through a sample, the amount of energy at each frequency is measured by a detector and the results are represented by a spectrum of intensity versus frequency. This method takes a considerable amount of time, and FTIR spectroscopy was created in part to overcome this disadvantage.

Fourier transform infrared spectroscopy measures all infrared frequencies simultaneously via the use of an interferometer. The sample can be analyzed via either transmittance or reflectance mode. Transmission FTIR spectroscopy was the method employed during this study. Briefly, a silica carbide rod serves as the radiation source. Photons released from the radiation source are directed into the interferometer, and incident on a beamsplitter. The beamsplitter "splits" the beam of photons in two. One half of the IR beam is transmitted to a fixed mirror and the other half is reflected to a moving mirror. The beams recombined at the beamsplitter after being reflected by the two mirrors. An interference pattern is produced that passes through the sample and is focused on the detector. An interferogram is created that contains information over the entire IR region to which the detector is responsive. The interferogram is converted from an intensity versus time within the mirror scan spectrum to the final IR spectrum showing intensity versus frequency by a mathematical operation known as Fourier transformation (Hsu, 1997). Advantages of FTIR spectroscopy over other methods include greater optical throughput because of decreased time per sampling and precise measurement without the need for external calibration. Infrared spectroscopy allows positive identification, or qualitative analysis, of different kinds of material as well as quantitative analysis via the use of modern software algorithms to analyze the area of the peaks in the spectra produced by the spectrometer (Thermo Nicolet Co., 2001).

Attenuated Total Reflectance (ATR) Technique

The attenuated total reflectance technique is based on internal reflection where the infrared beam is totally reflected inside an ATR crystal (Mirabella, 1993) as seen in Figure 4. The ATR crystal must have a higher refractive index (n_1) than the sample (n_2). Total internal reflection only occurs if the angle of incidence is larger than the critical angle. The angle of incidence is defined as the angle with respect to the normal and the critical angle is defined according to equation 21.

$$C = \mathrm{Sin}^{-1}\left(\frac{n_2}{n_1}\right) \tag{21}$$

where C is the critical angle. An evanescent wave from the infrared beam is created perpendicular to the surface of the ATR crystal at each point of reflection in the ATR crystal as shown in Figure 5. The electric field of the evanescence wave interacts with the sample in the vicinity of the ATR crystal where part of the electrical field may be absorbed by the sample resulting in an attenuation of the intensity of the reflected infrared beam, hence the name of the technique. The amplitude of the electric field declines exponentially with distance from the surface, z, of the ATR crystal according to

$$E = E_0\, e^{-z/dp} \tag{22}$$

where E and E_o are the electric field after and before the exponential decline, respectively, and the penetration depth, d_p, is a measure of depth at which the electric field penetrates into the sample of refractive index n_2. (Mirabella, 1993)

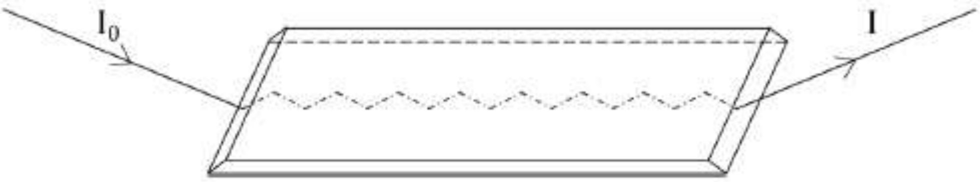

Figure 4. Schematic Figure Illustrating the ATR Technique where the Infrared Beam is Totally Reflected Several Times Inside the ATR Crystal. I_o and I are the Intensity of the Infrared Beam Before and After the Interaction with the Sample Respectively.

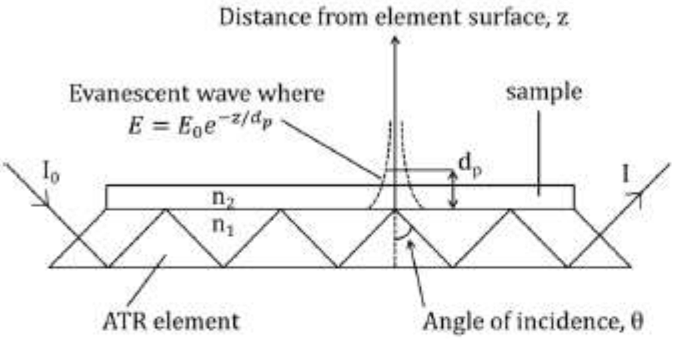

Figure 5: Schematic Diagram Illustrating the ATR Technique where the Evanescent Wave is Penetrating the Sample.

The penetrating depth may be represented by

$$d_p = \frac{\lambda_1}{2\pi\left(sin^2\theta - n_{21}^2\right)^{\frac{1}{2}}} \tag{23}$$

where λ_1 is the wavelength of the infrared radiation inside the ATR crystal, θ is the angle of incidence and n_{21} is the ratio of the refractive indices $(n_2|n_1)$. The penetration depth is typically some hundreds of nanometers to a few micrometers, which makes ATR spectroscopy a technique ideal for studying surfaces and thin films.

Spectral Imaging

Spectral imaging (SI) has proven extremely useful in numerous imaging applications, including object and material recognition, color analysis, remote sensing and astronomy (Wellman, 1981; Sun & Anderson, 1993; Abrardo et al., 1999; Slater & Healey, 1999). The fields which find applications for SI are growing in number, for example, medical imaging, agriculture, archaeology, and art (Gat, 2000). Besides, SI has been suggested as a non-destructive method for identifying pigments (Frey & Warda, 2008; Cosentino, 2013).

Spectral imaging provides images at multiple wavelengths and hence generates precise optical spectra at every pixel (Richard et al., 2002). A spectral image can be considered as a three dimensional image cube $I(x, y, \lambda)$ where a 2-dimensional image records the spatial information of a sample, and the third dimension represents spectral wavelength. Spectral imaging is an active field, made possible through the advances in charge-coupled device (CCD) detectors, dispersion optics, and spectral image processing algorithms (Yuval et al., 2006).

Imaging is the science and technology of acquiring spatial and temporal data information from objects for the purpose of obtaining information. At this time, digital imaging is the most advanced and applicable method where data are recorded using a digital camera, such as a charged coupled device (CCD). In biological studies, the images can be measured either by common optical methods such as optical microscopy or by more advanced methods that provides additional physical or chemical information about the objects.

Imaging spectroscopy is the simultaneous acquisition of spatially coregistered images, in many narrow, spectrally contiguous bands, measured in calibrated radiance units, from a remotely operated platform (Schaepman et al., 2009). Imaging spectroscopy is particularly useful for non-homogeneous samples or scenes. Examples include spatial classification based on spectra signatures, use of spectra libraries for material identification, mixture composition analysis, plume detection, etc (Gat, 2000).

Digital imaging was originally a field that has been developed in the early sixties to solve physical and technical problems by simulation, design and processing of pictorial data for analysis, visual inspection, measurement and visualization (Yuval et al., 2006). Currently, digital imaging has received a high level of maturity with a well founded rationale for many application fields (Matthias, 2006). It is the most advanced and applicable method where data are recorded using a digital camera, such as CCD. A digital image may be created directly from a physical scene by a camera or similar devices. Many technical images, which are not subject of our study, such as those acquired with tomographic equipment, or radio telescopes, are actually obtained by complex processing of non-image data. The best example of such imaging is magnetic resonance imaging (MRI). MRI is a medical imaging technique most commonly used in radiology to visualize detailed internal structures and limited functions of the body. It provides much greater contrast between the different soft tissues of the body making it very useful (Bersha, 2010).

The fields of classical imaging and optical spectroscopy have developed independently. While imaging deals with pictorial information that uses the description of material by their surfaces in terms of brightness, texture and color depending on the illumination in the two dimensional field of view of the optics, spectroscopy classifies material properties due to their radiation in particular spectra bands but mostly limited to a single point of the object's surface (Stuart, 2004). Combining imaging devices and spectrographs to record point spectra for entire surfaces of objects lead to the new and emerging field of spectral imaging. Both spectroscopy and imaging are well developed and being used broadly in many fields.

The combination of optical imaging and spectroscopy creates a three dimensional (3D) data set that contains many images of the same object, where each one of them is measured at a different wavelength, providing wealth of information that enables solutions for challenging tasks in various application sectors (Yuval et al., 2006). Imaging provides the intensity at every pixel of the image $I(x, y)$, spectroscopy provides a single spectrum, $I(\lambda)$ and therefore spectral image provides a spectrum at each pixel $I(x, y, \lambda)$ (Yuval et al., 2006). Figure 6 shows a spectral image data set and a spectral image cube. As a result, the spectral image provides a complete spectrum of the object at every pixel location throughout the lateral dimensions. Thus, a spectral image cube can be considered as either a collection of images, each of which is measured at a specific wavelength, or as a collection of different wavelengths at each pixel location. The spectral image $I(x, y, \lambda)$ is commonly referred to in the scientific literature as image cube, spectral cube, and spectral hyper cube etc.

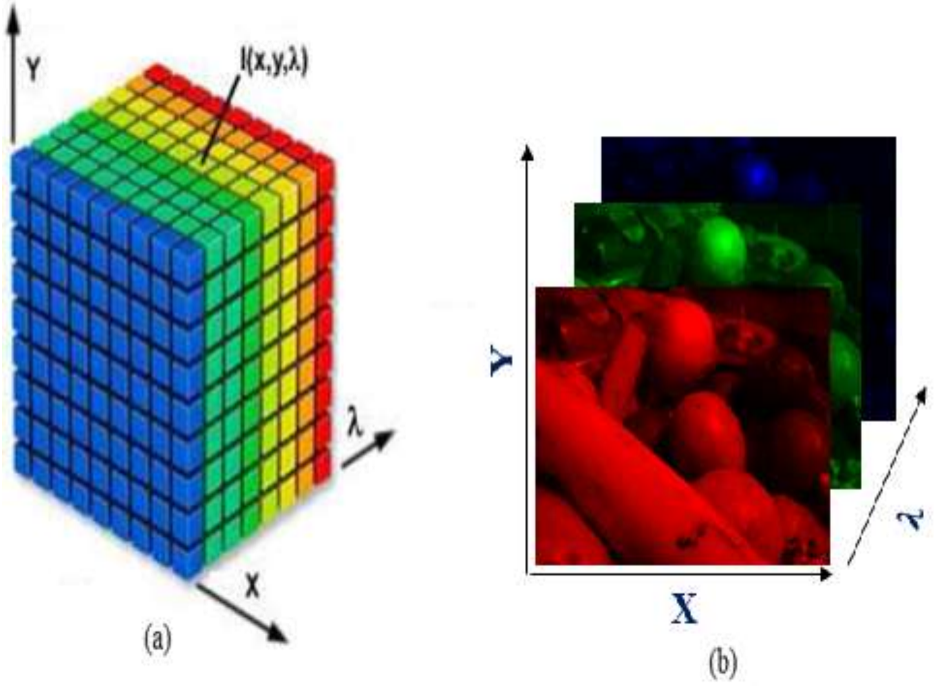

Figure 6: Description of a Spectral Image Data Set: (a) Each Point in the Cube Represents a Single Number and the Spectral Image is Described as $I(x, y, \lambda)$ and (b) Represents a Series of Spectral Images (Dickson & Davidson, 2010).

There are two basic approaches for SI techniques. The first approach acquires a sequence of two-dimensional images at different wavelengths. This can be implemented by using a rotating filter wheel or a tunable filter in front of a monochrome camera. The second approach acquires a sequence of line images where for each pixel on this line a complete spectrum is captured. This implementation requires an imaging spectrograph coupled to a monochrome matrix camera. One dimension of the camera (spatial axis) records the line pixels and the other dimension (spectral axis) the spectral information for each pixel. To acquire a complete spectral image, either the object, or the spectrograph needs to be moved in small steps, until the whole object has been scanned (Matthias, 2006).

In digital imaging spectroscopy, each pixel acquires many bands of light intensity data from the spectrum (Schaepman et al., 2009). Simultaneous imaging in multiple spectral bands across the spectrum enables us to visualize details far beyond the capabilities of the human eye. When imaging is done at spectral bands between 2 to 20, we have multispectral imaging (MSI) and hyperspectral imaging (HSI) for more than 100 spectral bands. MSI and HSI systems, operated from ground, airborne and space-based platforms, have found a variety of applications. These technologies have applications in fields that range from environmental monitoring, geology, military surveillance, among others.

Spectral signatures acquired in MSI make it possible to discriminate among different types of materials (Nischan et al., 2003). Combined with telescopes, MSI exposes the secrets of the universe (Coffey, 2012). A multispectral image can be seen as:

$$F: R^2 \rightarrow R^m \tag{24}$$

where R is the image and m is the number of bands. This function corresponds to a point (x, y) to a vector of functions:

$$F = f_1(x,y), f_2(x,y), \dots, f_m(x,y) \tag{25}$$

where f is intensity, and x and y, coordinates in the plane.

The involvement of imaging spectroscopy in diagnostics is now applied in a vast range of research fields, including biomedicine, zoology, remote sensing, food sciences, and agriculture (Brydegaard et al., 2011). Optical diagnostics involving photon transport usually starts by measuring the basic optical properties of the sample of interest. (Tuchin, 2007; Jacques & Pogue, 2008).

Spectral image cubes are analogous to a stack of pictures of an object, a sample, or a scene, where each image is acquired at a narrow spectra band. Each pixel in the image cube, therefore, represents the spectrum of the scene at that spectra band (Gat, 2000). The nature of imagery data is typically multidimensional, spanning three spatial, one spectrum and one temporal dimension. Each point in this multidimensional space is described by the intensity of the radiance which is emitted, reflected, or a combination of both (depending on the phenomenology under investigation). Since detector arrays in image capture devices are two dimensional at most, they can only capture two dimensions of the data at a time (Gat, 1999).

The data collected by imaging spectroscopy devices facilitates quantitative and qualitative characterization of spectral measurements. The results had been used, mostly unambiguous direct and indirectly, for the identification of materials, such as biological samples and atmospheric trace gases, the measurement of their relative concentrations, and subsequently the assignment of the proportional contribution of mixed pixel signals (e.g. spectral unmixing), the derivation of their spatial distribution (e.g. mapping), and finally their evolution over time (multi-temporal analysis) (Park et al., 2007; Jalil, 2008; Coffey, 2012). On a microscopic level, blood cells are spatially distributed by their refractive indices (Jacques, 1998; Bersha, 2010).

Multispectral imaging microscopy (MSIM) is obtained when optical imaging spectroscopy is done at several spatial locations at microscopic level, with transmittance (ϕ), at several wavelengths, ϕ (λ). MSIM at these locations and wavelengths is therefore represented as ϕ (x, y, λ) (Brydegaard et al., 2009). In most optical diagnostics, the aim lies in extracting all the information possible from a sample, which is generally impossible. In spectroscopy, the aim is to account for all photons emitted and to be able to explain whether they are absorbed, scattered, or re-emitted as fluorescence. The potential of measuring scattering, reflection and transmission of samples have advanced the MSIM significantly over a conventional transmission microscope (Svanberg, 2009; Merdasa, 2010). Application of MSIM identifies hidden diseases (Coffey, 2012).

The power of MSIM arises from the ability to image a scene rapidly in numerous spectral bands. The spectral signatures acquired in this fashion make it possible to discriminate among different types of materials (Nischan et al., 2003). The chemical and physical properties of samples can be produced from MSIM, since a material’s chemical and physical properties are dependent on its distribution within the sample. On the basis of MSIM data, quantitative and qualitative analysis of the sample can be performed (Morris, 1993; Colarusso et al., 1998).

Multispectral imaging microscopy uses a digital charge-coupled device (CCD) camera coupled with coloured filters of different spectral bands, ranging from just three components, as in a RGB conventional camera, up to hundreds of components, as in a hyperspectral system (Nieves et al., 2005). MSIM system employs more than 3 (N>3) narrowband filters which result in greater spectral sensitivity compared to the conventional RGB imaging system which utilizes 3 broadband filters (Bautista & Yagi, 2011). The main application is spectral recovery, and therefore these techniques have been applied intensively in areas as diverse as artificial vision, industrial colorimetry, biomedical engineering, and medicine (Jalil, 2008). Of particular interest is their application in atmospheric optics and remote sensing, where it is difficult to obtain high spectra and high spatial resolution at low cost (Nieves et al., 2005).

In many cases, the availability of a larger number of spectra bands has created important competitive advantages with regards to techniques based on MSIM. In MSIM data, the detectable number of pure spectra signatures (end members) is often less than the effective number of end members present. MSIM devices, when combined with image processing techniques, can solve portability and cost problems and recover either spectral reflectance or the illumination spectrum at each pixel of a captured image with good spectral resolution (Clark, 1999).

Multispectral imaging microscopy systems are not designed to sample a large portion of the electromagnetic (EM) spectrum at a fine detail, and may miss important information contained in the non-sampled bands. Diagnostic absorption features that characterize materials often occur over a small portion of the spectrum (Clark, 1999).

Now it is understandable that the amount of information available in MSIM is almost endless, so it would be very costly and inefficient to try to collect all data throughout the electromagnetic spectrum. An analytical device is made with a definite number of spectra bands in the region of interest for experiments. The imaging device is capable to simultaneously collect spectra data from several regions in space discredited, leading to both the collection of spatial and spectra data from many points in a three-dimensional image.

Components involved in the acquisition process of a MSIM system are illustrated in the Figure 7. I_R (λ) is the spectral radiance of the illuminant, r (λ) is the spectral reflectance of the surface, O (λ) is the spectral transmittance of the optical system, $\Phi_k(\lambda)$ is the spectral transmittance related to the *k*th filter and a (λ) is the spectral sensitivity of the camera (Jalil, 2008). The camera output f_k, related to the channel *k* for a single pixel of the image, and is given by equation 26.

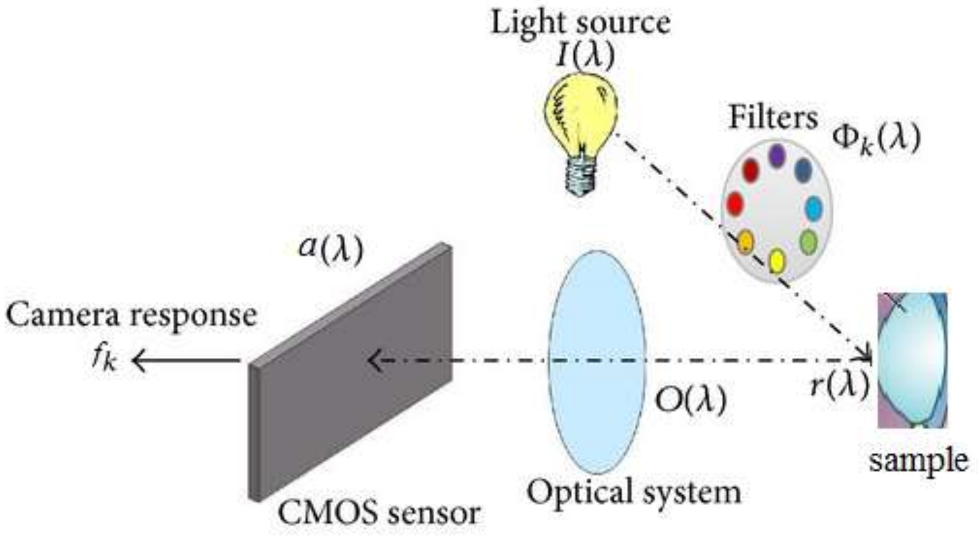

Figure 7: Synopsis of the Spectral Model of the Acquisition Process in a Multispectral System (Jalil, 2008).

$$f_k = \int_{\lambda_{\min}}^{\lambda_{\max}} I_R(\lambda) r(\lambda) O(\lambda) a(\lambda) \Phi_k(\lambda) d\lambda$$

(26)

The vector of the sampled spectral reflectance of the scene $r(\lambda)$ is also given as:

$$r(\lambda) = [r(\lambda_1), r(\lambda_2), \ldots, r(\lambda_n)]^{TP} \qquad (27)$$

where *TP* is the transpose operator. Assuming a linear optoelectronic transfer function, $I_R(\lambda)$, $a(\lambda)$, $O(\lambda)$ and $\Phi_k(\lambda)$ can be replaced by the spectral sensitivity $S_k(\lambda)$ of the *k*th channel. Then, equation 26 becomes:

$$f_k = \int_{\lambda_{min}}^{\lambda_{max} \int S_k(\lambda) d\lambda} r(\lambda) \tag{28}$$

By sampling the spectra to *N* wavelengths, equation 28 can be written in matrix notations as shown in equation 29.

$$f_k = r(\lambda)^{TP} S_k(\lambda) \tag{29}$$

$$S_k(\lambda) = [S_k(\lambda_1), S_k(\lambda_2), \ldots, S_k(\lambda_N)]^{TP} \tag{30}$$

is the vector containing the spectral sensitivity of the acquisition system related to the *k*th channel. From equation 29, the spectra response of the system is firstly characterized, including the camera and the illuminant, by finding the operator $S_k(\lambda)$. Then, using this operator from a spectral image, the spectral reflectance curve for each pixel of the imaged scene is reconstructed (Jalil, 2008).

Optical Microscopy

Optical microscopy is the most efficient and reliable diagnostic technique being applied today. It is highly sensitive and specific in the sense that samples are visualized and identified by their features. One advantage of optical microscopy is that it is used for specie identification (Ross et al., 2006). Optical microscopy technique has been used for the detection of malaria parasites in the vertebrate host and involves direct microscopy of fixed tissue or blood cells stained with differential stains such as Giemsa or with fluorescent dyes which are deoxyribonucleic acid (DNA) or ribonucleic acid (RNA) specific (Van Den Berg et al., 1991).

Resolution of an optical microscope is defined as the minimum separation needed between two media under examination in order for the microscope to discern them as separate media. If two media are separated by a distance shorter than the minimum distance (δ), they will appear as a single medium viewed under the microscope.

Generally, a measure of the resolving power of a lens is given by its numerical aperture (NA):

$$NA = n \sin \alpha_o \tag{31}$$

where α_o is the angle spanned by the objective lens seen from the medium, and n is the refractive index of the medium (≈1 for air). State of the art objectives can have a numerical aperture of up to 0.95. Because sin α_o is always less than or equal to unity, the numerical aperture can never be greater than unity for an objective lens in air.

$$\delta = \frac{0.61\lambda}{NA} \tag{32}$$

where λ is the wavelength of light. From this it is clear that a good resolution (small δ) is connected with a high numerical aperture. The combination of optical microscopy imaging and spectroscopy quantify several biological investigations (Teikari, 2008).

Multispectral Imaging Microscope

The imaging system used in this study was a multimodal, multispectral imaging microscope developed by Mikkel *et al.* (Mikkel et al., 2008) and advanced by Merdasa (Merdasa, 2010). The equipment consists of a commercial optical microscope (Brunei compound microscope) modified by replacing the conventional illumination light (white light) with monochromatic LED lighting system. Thirteen LEDs emissions centred at 375 nm, 400 nm, 435 nm, 470 nm, 525 nm, 590 nm, 625 nm, 660 nm, 700 nm, 750 nm, 810 nm, 850 nm and 940 nm were used. This wavelength range covers UV, visible and NIR optical region. It may be noted that all the LEDs show an appreciable chromaticity though there is little overlap of some of the spectra of neighbouring LEDs. The LEDs are mounted in a quasi hemispherical container made of teflon and illuminate same spot on a 5 mm Opal light diffuser (Edmund Optics) which in turn provides a Lambertian-like illumination to the sample**.** A Lambertian source of light is one which has same apparent radiance when viewed at any angle, hence provides uniform illumination to the sample.

To achieve multispectral imaging, the LEDs are activated sequentially through a computer-controlled data acquisition card (DAQ from National Instruments Inc.). The sample is illuminated in three different modes: bright field (transmission), dark field (scattering) and reflection. For transmission measurement, the sample is illuminated by the set of LEDs located directly below the sample. In reflection mode, light reaches the sample from above via a system of optics, which includes a Cassegrain objective. The cassegrain objective (XI5 Reflx™® objective from Edmund Optics) is a reflective objective that is essential for reduction of chromatic aberration in all the three modes of imaging. Dark field imaging is achieved through the use of a ring coupled on an optical fibre. The ring provides an oblique illumination that cannot be accepted by objective’s aperture, hence only light which is scattered by the specimen can enter the objective. An image formed in this way has bright objects superimposed upon a dark background.

A computer controlled 12-bit (resolution 640X480 - 1600X1200) monochrome CMOS camera (Guppy GF503B, Allied Vision Technologies) is fitted on the microscope ocular to capture an image of the sample at each LED illumination. Figures 8 show the schematic diagram of the multispectral imaging microscope

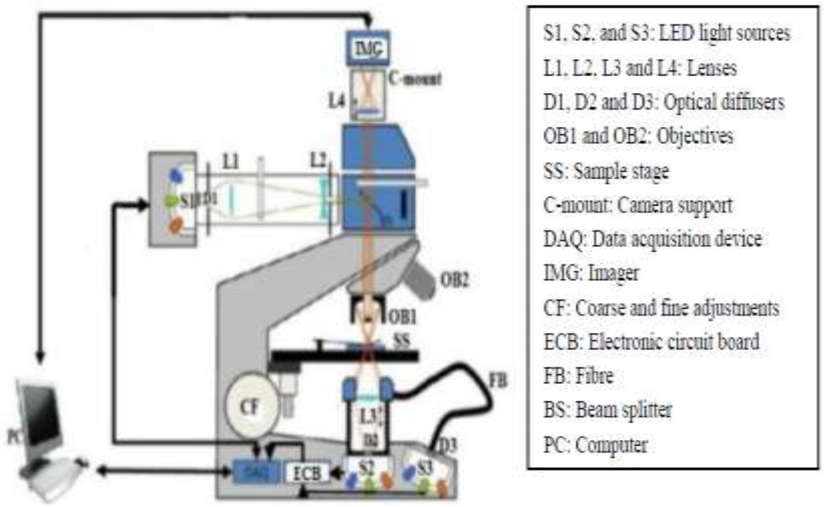

Figure 8: Multispectral Imaging Microscope (Opoku-Ansah, 2016).

Slit Lamp Microscope

The Slit Lamp Microscope (SLM) can be defined as a long working distance microscope for observation of the eye. By using oblique illumination it provides oblique sectioned views of the cornea. Gullstrand developed its principle and Zeiss made the first instrument. This microscope was used for the first time for corneal endothelium examination by Vogt (Böhnke & Barry, 1999). A lamp is attached to a standard stereomicroscope. The projected light (focused or diffuse) has high intensity and can illuminate the eye from different angles. This allows examination of all anterior structures of the eye (Gierl et al., 2007).

In this type of microscope, the light is conveyed onto the specimen through an adjustable slit which limits the beam width. The microscope is built in a way that it always focuses the region that is being illuminated. To maximize the image contrast, the angle between the observation microscope and the viewing optical system can be changed (Böhnke & Barry, 1999). The illumination lamp has freedom to rotate to accomplish the idea of different angles of observation. To obtain a focused image, the position of the lamp can be changed through both horizontal and vertical axis and through the rotational angle α. The instrument position will affect the imaged area (Gierl et al., 2007). The slit lamp microscope needs an illumination system whose function is to provide the ideal light conditions for the best observation of the specimen. In these microscopes, the most adopted technique is the Koeller illumination system. While providing a homogeneous slit image, it uses a variable aperture slit allowing to change the slit width and height (Henson, 1983).

The resolution, brightness and depth of field are important characteristics of the slit lamp microscope. In this type of microscope the resolution is directly associated with its numerical aperture. Numerical aperture is also associated with the working distance of the microscope and the diameter of the objective as given in equation 31 (Henson, 1983). The microscope depth of field restrains the brightness of the instrument. It is not possible to have maximum brightness (not counting with the lamp brightness) and maximum depth of field. Higher brightness will result in lower depth of field (Zeiss, 2001).

The slit lamp microscope is described as an instrument with the capability to observe different structures of the living eye. For that purpose, several configurations can be used in order to get the best image of each ocular structure. The differences in these configurations result from the type of illumination, magnification power and slit width. Optical section, direct illumination, indirect illumination, scattering sclera-corneal illumination, fundus observation, fluorescence observation and assessment of lachrymal film are some examples of illumination techniques that can be executed on the slit lamp microscope (Zeiss, 2001). Optical section technique, also known as direct focal illumination, is the most adopted technique in slit lamp examination. In this method, the illumination system and the viewing path should form a large angle, around 90º.

Another method to examine the different eye structures is the direct diffuse illumination. Here, the light source is modified by placing a diffuser or ground glass screen in the illuminating path (Zeiss, 2001).The recommended settings to perform this type o examination are well established; the slit must be fully opened, the angle between the illuminating and viewing paths should be around 30 º and the magnification can vary from 5x to 30x, depending on the structure to be observed. Indirect illumination is characterized by the non-intersection between the axis of the illumination and viewing paths at the focus. Instead, the slit lamp illuminating prism rotates around its vertical position and becomes decentred. This position will illuminate the area to be examined by a reflected indirect beam of light. The slit width varies from narrow to medium (2 to 4 mm). This method is mainly used to observe corneal features such as corneal scars, deposits, epithelial or stromal defects (Zeiss, 2001).

Multivariate Data Analysis Techniques

Spectra containing data sets with many physical parameters have groups of these parameters varying together. One reason is that more than one parameter may be measuring the same driving principle governing the behaviour of the spectra. In many systems there are only a few such driving forces. Another reason is that important characteristics of the spectra may be completely or partially obscured during measurements, because individual measurements may be noisy and contain large variability. These problems can be simplified by replacing a group of variables with few representative new variables.

The task of extracting the driving principle governing the behaviour of the spectra from the many measured variables in general has been addressed by means of multivariate data analysis (MDA) techniques, which deals with optimum extraction of information from a set of measured data by application of relevant mathematics and statistical tools (Martens & Naes, 1991; Esbensen, 2002; Davies & Fearn, 2005; Davies, 2005). This rather broad characterization reflects the fact that many techniques constituting MDA have evolved from a number of rather diverse fields, e.g. economics, psychology and chemistry. Hence, MDA lacks a distinctive definition.

Multivariate methods are robust to noise, and enable a filtering of the data such that the systematic information (the “effects”) is highlighted. This is because the latent variables become stabilized by including many relevant variables, even if each of the measured variables is very noisy. Multivariate data analysis seeks to overcome the limitation of noisy variables registered, by using all variables at the same time.

Large data tables in general, and short and wide matrices in particular, require the use of multivariate projection methods, such as Principal Component Analysis (PCA), for analysis. Multivariate analysis by projection has the following advantages: it deals with the dimensionality problem, handles many variables and few observations, few variables and many observations, and almost square matrices of any size (Esbensen, 2002; Davies & Fearn, 2005; Davies, 2005). Further, it copes with multi-collinearity, missing data, robust to noise, separates regularities from noise, provides informative diagnostic and graphical tools (Esbensen, 2002; Davies & Fearn, 2005; Davies, 2005).

In multivariate data, the possibility of finding correlations by chance increases dramatically with increasing number of variables. In the comprehensive framework of MDA, extracting information from a multivariate data set may be approached in numerous ways, e.g. by applying principal component analysis or discrimination and classification analysis (Esbensen, 2002; Davies & Fearn, 2005; Davies, 2005). Both of these approaches can be very effective, especially for classifying samples.

Calibration, as used in MDA, is in short to relate some more or less concealed characteristics of the system to a set of directly measurable parameters, or in other words, to relate a set of implicit properties of a system to a set of explicit properties. These implicit and explicit properties are quantified by a set of so-called dependent and independent variables.

Clustering Analysis

Cluster analysis, in general, uses statistical methods to identify groups that behave similarly or show similar characteristics in a dataset (Kaufman et al., 2005). There are many clustering algorithms such as K-means cluster analysis, Hierarchical Cluster Analysis (HCA) and C-means clustering techniques. In this work, Hierarchical Cluster Analysis (HCA) has been used because of its popularity in production of dendrograms which can provide a two-dimensional pictorial representation of the clustering process (Thanh et al., 2004).

Clustering analysis or simply clustering is the process of organizing a set of data into groups in such a way that observations within a group are more similar to each other than they are to observations belonging to a different group. Clustering is also known as an unsupervised learning process that assumes that the data set represents features that would allow one to distinguish one group from another. It is known as unsupervised learning process because it does not require prior knowledge of the number of groups in a data set.

Clustering is defined in terms of two functions, the distance function and the linkage function. The distance function computes the distance between points and the linkage function computes the distance between clusters. Clustering results often vary based on the choice of these functions. Let A and B be two clusters containing two ponts a_α and b_β respectively. Generally, the distance between the two points a_α and b_β is defined by

$$d_p(a_\alpha, b_\beta) = \left(\left|\sum_{k=1}^{K} a_{\alpha,k} - b_{\beta,k}\right|^p\right)^{\frac{1}{p}} = \left\|a_\alpha - b_\beta\right\|_p, p > 1 \qquad (33)$$

called the Euclidean distance. The Euclidean distance has an intuitive appeal as it is commonly used to evaluate the proximity of objects in two or three-dimensional space. The distance between the two clusters also is defined as:

$$\varphi(A, B) = min\, \varphi\, (a_\alpha, b_\beta) \qquad (34)$$

known as a single-linkage criterion (Jain & Dubes, 1988; Jain et al., 1999). The clusters depend on the choice of a clustering distance. If two points satisfy the condition that $\varphi(A,B) \leq d$, then A and B are combined into a single cluster.

The linkage function clusters all groups in a data set hierarchically by their similarity. The visualization of the linkage structures are often plots referred to as dendrograms. Dendrograms are tree diagrams that show nested structure of partitions and how various groups in the data set are linked at each stage. Dendrogram can be represented horizontally or vertically.

Principal Component Analysis

Principal component analysis (PCA), introduced in 1933 by H. Hotelling (Hotelling, 1933), is an exploratory statistical multivariate technique designed to identify unknown trends in a multidimensional data set, say Z. PCA is an applied linear algebra technique that computes the most important basis to re-express a complex and noisy multidimensional data set. Application examples of PCA are numerous, from neuroscience to computer graphics (Esbensen, 2002; Davies & Fearn, 2005; Davies, 2005).

PCA is a non-parametric method of extracting relevant information from the multidimensional data set, Z, by reducing the complex multidimensional data set to a lower dimension such that the principal hidden or latent factors are revealed. The reduced-dimensional space help build more effective data analyses for classification, pattern recognition clustering and so on.

PCA produces a new set of dimensions or axes against which the original multidimensional data set is represented, described or evaluated. This analysis approach enables one to discover and work with the principal latent components rather than the original data.

When two or more signals or dimensions are highly correlated or dependent, they are likely to represent highly related phenomena. Thus, the variances in the data are where the signals or dimensions can be best discriminated and key underlying phenomena observed. So, in PCA, correlated variables are combined and uncorrelated ones, particularly the observations that have high variance, are focused on. At the end of the analysis, smaller set of variables that explain most of the variance in the original data, in more compact and insightful form is sought for.

The new variables or dimensions in PCA are linear combinations of the original ones and uncorrelated with one another, that is, orthogonal in the original dimension space. They are captured as much of the original variance in the data set as possible and are called principal components, (PCs). The PCA as a projection method projects the experimental multidimensional data set onto new axes, the principal components (PCs), and gives better representation of the data set without losing much information.

Principal component analysis is considered as a form of rotation of the existing axes to new positions in the space defined by original variables. The new dimensions or axes are orthogonal and stand for the directions with maximum variability.

More often PCs are obtained for use as input to another analysis. One example is in principal component regression (PCR). PCs are useful when there are too many explanatory variables relative to the number of observations and are highly correlated. Both situations lead to problems when applying regression techniques, and may be overcome by reducing the explanatory variables to a smaller number of principal components (Everitt & Dunn, 2001).

Principal component analysis is considered as a form of rotation of the existing axes to new positions in the space defined by original variables. The new dimensions or axes are orthogonal and stand for the directions with maximum variability. A multidimensional data set, Z of m observations and n variables is centered Z_c such that the elements of the matrix of dimension $m \times n$ are around the sample mean of zero. The Z_c is then converted into covariant matrix S defined as

$$L = \frac{1}{m-1} Z_c^{/} Z_c \tag{35}$$

where $Z_c{}'$ denotes the matrix transpose of Z_c. Each column in the captured data corresponds to one variable and one row corresponds to the values observed at one point at a time. Thus, the data points are vectors in a multidimensional space and the PCA of the data gives vectors of scores, with values that summarize all the variables entering the analysis. The square, symmetric, nonsingular covariant matrix L is further transformed into a diagonal matrix using the relation below,

$$K = \gamma^{/} L \gamma, \tag{36}$$

where the columns of γ contain the eigenvectors of L and

K is a diagonal matrix with the eigenvalues along the diagonal. γ is used to obtain new variables called Principal Components (PCs).

A plot of the PC loadings shows the variables that are responsible for the trends in the data set and how much each variable contributed to each PC. These indicate the variables that are important, and correspond to the directions in a PC score plot.

So, the new axes are the eigenvectors of the matrix of covariance or correlations of the original variables, which capture the similarities of the original variables based on how data samples project to them.

The first PC (PC1) retains the greatest amount of variation in the sample and corresponds to the line with maximal variance. The data points are projected with values along this new axis. The second PC (PC2) retains the second greatest amount of variation in the sample but orthogonal to PC1 and the data points are again arranged so that the variance is as large as possible. The procedure continues to PC3 and so on. Thus, the k^{th} PC retains the k^{th} greatest fraction of the variation in the sample but orthogonal to $(k-1)^{th}$ PC. PCs once identified can be used for classification and discrimination or as parameters for modeling in other multivariate techniques.

The usefulness of this artificial variants (PCs) constructed from the observed variables is obtained by determining the proportions of the total variance for which it is accounted. The components of lesser significance can be eliminated without losing much information provided the eigenvalues are very small. If, for example, 96 % of the variation in a multivariate data set involving 30 variables can be accounted for in the PC 1 and PC 2, then almost all the variation could be expressed along a double continuum rather than in 30-dimensional space. This would provide a best summary of the data that might be useful in later analysis.

The new co-ordinate values, collected as columns along given PC, are called the PC scores. These columns are orthogonal and are PC score vectors.

The PC scores are the co-ordinates of the data points in the PC space and a plot of these PC scores in the PC space results in a PC score plot.

The eigenvalue denotes the amounts of variability captured along that dimension and tell about the explanation grade and suggest the possible truncation or PCs to be retained. Factors often considered when determining the number of PCs to be retained include the amount of total sample variance explained, the relative sizes of the eigenvalue (variances of the sample components), and the subject-matter interpretations of the components.

A useful visual aid to determining an appropriate number of PCs has been a "scree plot", a graphical method of plotting the ordered v_k against k and deciding visually when the plot has flattened out, i.e., a bend in the scree plot. The number of PCs is taken to be the point at which the remaining eigenvalues are relatively small and all about the same size (Johnson & Wichern, 2002). Alternatively, Kaiser's rule, which suggests that from all the m PCs only the ones whose variances are greater than unity or, equivalently, are the components that should be retained, explain at least $(1/m)100$ % of the total variance, can also be used. This criterion has a number of positive features that have contributed to its popularity but cannot be defended on a safe theoretical ground (Esbensen, 2002).

Two Group Discrimination and Classification

For groups of observations, a subset of variables of the groups and associated functions of this subset and a set of associated variables can be located in order to maximize separation among these groups using discriminant analysis. Discriminant analysis is one of such exploratory multivariate methods of determining variables and reduced set of functions concerned with maximally separating set of observations obtained for the groups. This analysis method is employed on a one-time basis in order to investigate observed differences when causal relationships are not well understood. The following references (Everitt & Dunn, 2001; Johnson & Wichern, 2002; Esbensen, 2002) are good sources for more comprehensive discussions on discrimination and classification.

The objectives of any discriminant analysis is to construct a set of discriminants that can be used to explain or characterize the group separation with a reduced set of variables, as well as to analyze the contributions of the original variables to the separation and evaluate the degree of separation. The immediate objective of discrimination analysis is to describe, either graphically or algebraically, the differential features of the observation from the several known collections. The numerical values of the discriminants are such that the collections of the data are separated as much as possible.

Maintaining maximum separation for the subset of the original variables in discriminant analysis requires a number of functions known as rank or dimensionality of the separation. Such functions when linear are referred to as linear discriminant functions (*LDF*) and can locate the exact contrast, up to a constant of proportionality that lead to significant separation. When comparing the significance of two means with a common covariance matrix, Σ of the population, a two group *LDF* can be develop to obtain a contrast in the sample mean vectors that can lead to maximum separation of the sample group means.

In order to locate a meaningful mean difference, a variable-at-a-time, independent of the other variables in order to assist in a model when the mean difference is found to be significantly different from zero, correlation between the discriminant function is calculated. Correlations of variables with the linear discriminant function have been used as a past-hoc data analysis tool.

It is assumed that, for two group discriminant analysis, the two independent samples from two multivariate normal populations have common covariance matrix, Σ and unknown means μ_1 and μ_2. A linear combination of the variables from the two groups that provides for the maximum separation between the groups is the Fisher's two group linear discriminant function, L. given as

$$L = v^{/} x = \sum_{j=1}^{p} v_j x_j \ , \qquad (37)$$

The discriminant scores that brings about a maximum separation between the two groups is a vector defined as

$$v = S^{-1}(\bar{x}_1 - \bar{x}_2) \qquad (38)$$

where S is the common sample variance, an unbiased estimate of Σ and $\bar{x}_i$ is the sample mean for the observations in groups 1 and 2.

The discriminant scores are evaluated at the group mean vector $\bar{x}_i$, using the difference in the mean discriminant scores such that it is exactly equal to Mahalanobis' D^2 statistic defined as

$$D^2 = \left(\bar{x}_1 - \bar{x}_2\right)^{/} S^{-1}\left(\bar{x}_1 - \bar{x}_2\right) \qquad (39)$$

Hotelling's T^2 statistics, defined as

$$T^2 = \left(\frac{n_1 n_2}{n_1 + n_2}\right) D^2 \qquad (40)$$

is used to test for the difference in the mean vectors of the two groups. If T^2 is significant then the sample group centroids for the two classes are said to have good separation. However, the square of the univariate student t^2 statistic is equal to T^2, thus a simple t test on the discriminant scores is equivalent to calculating T^2 for testing for the difference in the mean vectors for the two groups.

For discriminant scores, say y, representing the dependent variable and the dummy independent variables $x_1 = -1$ and $x_2 = 1$ for the two groups. A regression equation of the form

$$y = v_1 + v_2 x \tag{41}$$

where v_1 and v_2 are the constant coefficients, is fitted to the discriminant scores. A sample linear discrimination function, *LDF*, $L = \alpha' x$ as the estimate of the *LDF*, where $\alpha = \Sigma^{-1}(\mu_1 - \mu_2)$, will lead to significant separation between the two groups. The number of variables can be reduced and yet maintain significant discrimination, which can be approached using F statistic.

Classification analysis is another multivariate method technique that is closely connected with discriminant analysis. While discrimination analysis is often done to sharpen the separation between groups of observations and to understand the variables that carry the groups separation information, the classification analysis is often performed to predict a probable group membership from an observation. The objectives of these two methods tend to overlap because linear discrimination functions are often used to develop classification rules. The primary difference is that variables used to develop classification rules are usually applied to a group of known number of groups.

Classification analysis seeks to sort observations into classes with the emphasis on a rule that can be used to optimally assign new observations to the already labelled classes. So the concern of classification analysis is the development of rules for allocating or assigning observations to one or more groups. This leads to well-defined rules that can be used to assign new observation. This analysis method usually requires more knowledge about the parametric structure of the groups.

So, creating rules for assigning observations to groups that minimize the total probability of misclassification of the average cost of misclassification are the objectives. A good and optimal classification procedure results in few misclassifications, that is, the probability of misclassification is small and accounts for the costs associated with misclassification taking prior probabilities of occurrence into account.

Supposing two groups are labeled $\boldsymbol{\alpha}$ and $\boldsymbol{\beta}$ and have probability density functions (*pdfs*) $f_1(x)$ and $f_2(x)$ respectively, associating with them. Again, supposing p_1 and p_2 are their prior probabilities that x is a member of $\boldsymbol{\alpha}$ and $\boldsymbol{\beta}$ respectively, where $p_1 + p_2 =1$. And, let $c_1 = C(2|1)$ and $c_2 = C(1|2)$ represent the misclassification cost of assigning an observation from $\boldsymbol{\beta}$ and $\boldsymbol{\alpha}$ and from $\boldsymbol{\alpha}$ and $\boldsymbol{\beta}$. Then, assuming the *pdfs* are known, the total probability of misclassification (*TPM*) is equal to p_1 times the probability of assigning an observation to $\boldsymbol{\beta}$ given that it is from $\boldsymbol{\alpha}$, $P(2|1)$, plus p2 times the probability of assigning an observation into $\boldsymbol{\alpha}$ given that it is from $\boldsymbol{\beta}$, $P(1|2)$. Hence,

$$TPM = p_1 P(2|1) + p_2 P(1|2) \tag{42}$$

The error rate that minimizes the TPM is the optimal error rate (OER). Considering cost, the average or expected cost of misclassification (*ECM*) is defined as

$$ECM = p_1 P(2|1)C(2|1) + p_2 P(1|2)C(1|2) \tag{43}$$

A reasonable and better classification rule is established when the *ECM* is made as small as possible. However, costs of misclassification are hardly known.

Using *LDF* and assumptions that $\Sigma_1 = \Sigma_2 = \Sigma$ and $p_1 = p_2$ and that $C(1|2) = C(1|2)$, Fisher developed a *LDF* known as Fisher's Linear discriminant (*FLD*) function (Fisher, 1936). This discriminant function is used to find the linear combination of features that best separate the two groups. The *FLD* function simply uses unstandardized discriminant coefficients and may be used as a classification rule for classifying an observation *x* into $\boldsymbol{\alpha}$ or $\boldsymbol{\beta}$. The *LDF* as a rule does not required normality because *pdf* is not assumed. The groups' covariance matrices are assumed to be equal, because a pooled estimate of the common covariance matrix is used.

The method transforms the multivariate observation $\boldsymbol{x}$, by taking a linear combination of $\boldsymbol{x}$ to create univariate observations, *y*'s such that the *y*'s derived from the groups $\boldsymbol{\alpha}$ and $\boldsymbol{\beta}$ are separated as much as possible. A fixed linear combination of the $\boldsymbol{x}$'s take the values of *y*'s for the observations from group $\boldsymbol{\alpha}$ and the values of *y*'s for the observations from group $\boldsymbol{\beta}$. The difference between the means of the univariate *y*'s of the two groups, $\bar{y}_1$ and $\bar{y}_2$ expressed in standard deviation units is used to assess the separation of these two sets. That is,

$$R = \frac{|\bar{y}_1 - \bar{y}_2|}{S_y}, \tag{44}$$

where

$$S_y^2 = \frac{\sum_{j=1}^{n_1}\left(y_{1j} - \bar{y}_1\right)^2 + \sum_{j=1}^{n_2}\left(y_{2j} - \bar{y}_2\right)^2}{n_1 + n_2 - 2} , \tag{45}$$

is the pooled estimate of the variance. The objective of this process is to select a linear combination of ***x*** to attain maximum separation of the sample means $\bar{y}_1$ and $\bar{y}_2$.

The ratio of the variance between the groups to the variance within the groups is the separation, *R* between the two group distributions as defined by Fisher. That is

$$R = \frac{\sigma^2_{between}}{\sigma^2_{within}} = \frac{\left[w^{/}(\bar{x}_1 - \bar{x}_2)\right]^2}{w^{/} S_{pooled} w} \tag{46}$$

where $w^{/}\bar{x}_i$ is the weighted mean and $w^{/}S_{pooled}w$ is the weighted variance for group *i = 1, 2* which is as a result of the linear combinations of the variables of the groups. The *w* is the overall possible coefficient vectors. The *R* in a sense represents the measure of the signal-to-noise ratio for the group labeling.

The linear combination

$$Y = w^{/}x = (\bar{x}_1 - \bar{x}_2)^{/} S^{-1}_{pooled} x \tag{47}$$

maximizes the ratio and thus the separation over all the possible coefficient vectors *w*. The maximum of this ratio, from equation (50), is

$$D^2 = (\bar{x}_1 - \bar{x}_2)^{/} S^{-1}_{pooled} (\bar{x}_1 - \bar{x}_2) \tag{48}$$

In allocating a new observation $\boldsymbol{x_0}$ to say α, if

$$Y_0 = (\bar{x}_1 - \bar{x}_2)^{/} S_{pooled}^{-1} x_0 \geq M \tag{49}$$

where

$$M = \frac{1}{2}(\bar{x}_1 - \bar{x}_2)^{/} S_{pooled}^{-1} (\bar{x}_1 + \bar{x}_2) \tag{50}$$

else $\boldsymbol{x_0}$ is allocated to **β** if

$$Y_0 < M \tag{51}$$

The group mean and group covariance are estimated from the training sets. Although the estimates of the covariance may be considered optimal in some sense, this does not mean that the resulting discriminant obtained by substituting these values is optimal in any sense, even if the assumption of normally distributed classes is correct.

Crystalline Lens

The crystalline lens, as part of the anterior segment of the eye, is located behind the cornea and the iris as shown in Figure 9. It is composed of a clear membrane (the lens capsule), a subcapsular lens epithelium (only anteriorly), and lens fibers, which emerge from the epithelium cells. The lens and cornea transmit and refract light to form an image of the world on the retina. The elastic young crystalline lens changes shape via constriction or relaxation of the ciliary muscle to which the lens zonules are attached, resulting in a change of the optical power of the eye. This variable power provides a focused image of objects both near and far. With aging, the human lens becomes thicker, relatively steeper, and loses the ability to accommodate (Atchison et al., 1995; Glasser & Campbell, 1998; Dubbelman et al., 2005), a condition known as presbyopia. The refractive index of the lens is not homogeneous. It is distributed over the lens gradually, with a high refractive index in the lens centre, and a lower refractive index towards the lens surface. This gradient refractive index (GRIN) changes with age (Campbell, 1984; Hemenger, et al., 1995; Jones et al., 2005; Castro et al., 2011)

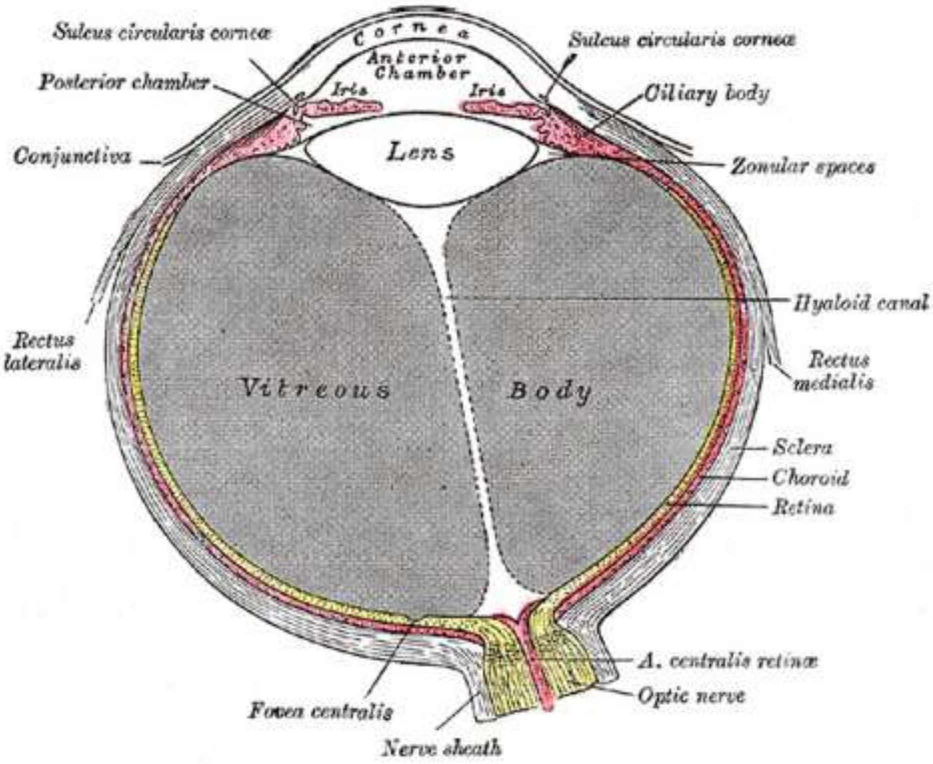

Figure 9: **C**rystalline Lens is Located Behind the Cornea and the Iris.

(Reproduced from Gray’s Anatomy, Standring, 2008).

The lens is composed of ectodermal cells at various stages of differentiation, surrounded by a basal lamina, the lens capsule. Anteriorly they form an epithelial monolayer while internally they are represented by shells of concentrically arranged fibre cells, which form the bulk of the lens. The most superficial fibres are metabolically active, nucleated cells while the deeper fibres, making up most of the adult lens, are organelle-free. The energy required for growth and transparency derives chiefly from glucose. Fifty per cent of epithelial ATP is derived aerobically, while for the lens as a whole about 70 per cent arises from anaerobic glycolysis (Winkler & Riley, 1991).

The proteins of the lens make up about 33 per cent of its wet weight and account for its high refractive index. The lens crystallins, alpha, beta and gamma, make up over 90 per cent of these proteins. Other proteins include cytoskeletal and membrane proteins such as actin, filensin and spectrin, transporters and channel proteins, junctional proteins concerned with cell communication and many enzymes involved in metabolism, protein synthesis and degradation. A number of excellent reviews on crystallin structure and function are available (Horwitz, 2003; Bloemendal et al., 2004; Sharma & Santhoshkumar, 2009).

Cataract

The cataract is simply clouding of the otherwise clear crystalline lens. It might involve the whole lens or just a portion e.g. the capsule of the anterior or posterior lens and the cortex, or the core of the lens. It usually leads to reduction in visual acuity. Cataract has not lost its place as the leading cause of treatable blindness and visual impairment around the globe (Abraham et al., 2006). Notwithstanding the fact that developing countries harbours 90% of the world’s cataract patients, its public, material and financial consequence is extended to industrial countries (Resnikoff et al., 2004; Abraham et al., 2006). Recent studies have brought to light that cataract is not a single disease (West & Taylor, 1986). Despite the fact that it was admitted that congenital cataract and secondary forms of cataract have a range of definite causative factors, 'senile cataract' had been tagged as a solitary disease unit since. There is a consensus now that there are three precise and different conditions constituting senile cataract. These are cortical cataract, nuclear cataract and posterior subcapsular cataract. Each has a unique pathology, occur in anatomically separate areas of the lens; they have a different age of onset, and also differ in their risk factors. Each one of this cloudiness could crop all alone or in mishmash. Cataracts remain a common disease of the elderly. Available data indicates that 2.4 million English and Welsh subjects in the United Kingdom suffer cataract (The Royal College of Ophthalmologists, 2004). In France, 20% of people between ages of 65-75 years, 35% of those aged between 75-85, and more than 60% of persons older than 85 are victims. In Canada, 12% of those aged 65-69 years and 28% of people 80 years and older experience cataracts (Millar, 2004). In Belgium, persons aged 65 years and older, 6.2% of male and 12.2% of females report with cataracts (Institut Scientifique de la Santé Publique, 2006). Owing to improved life expectancy, incidence rates of cataracts are on the ascendancy. In Ghana, the occurrence of cataract resulting in severe visual impairment or blindness among persons who are 40 years and older is 9% (Guzek *et al*., 2005) and is pegged at 2% in people aged 30 years and older (Moll et al., 1994)

Risk factors for cataract include gender. Age surely embody the collective result of dynamics so far to be identified. Several reports have branded the length of education as an essential risk factor for cataract (Taylor, 1999). However, duration of education is almost certainly confounded by factors that were ignored or yet to be understood. Many other cross-sectional studies of cataract risk factors are now available. The results from some longitudinal studies are also accessible (Chylack et al., 1998). Amidst all these propositions it seems convenient to sum up the risk factors for cataract; the six Ds (daylight, diet, drugs, diabetes, dehydration and "don't know").

Cataracts have been described using different descriptions some of which overlap. The classification is mostly based on anatomical location, etiological factors and others. Over the years classification systems such as the Lens Opacities Classification System II and III (LOCS II and LOCS III), the Oxford Cataract Classification System, and the systems used in the Beaver Dam Eye Study, at Johns Hopkins, and in the Age Related Eye Diseases Study use photographic standards to subdivide each major type further into grades (Klein et al., 1990). These grades are founded either on density and tint (in the case of the nucleus) or according to the anatomic area of the cataract (in the case of the cortical and posterior subcapsular regions).

Experimentally-Induced Animal Model for Cataract

Experimentally-induced models are by far the earliest approaches in the study of cataracts. The galactose cataract in rats had been used since 1935 to mimic diabetic cataract. Other sugar cataract models include alloxan and streptozocin induced (STZ) cataract (Mitchell & Cook, 1938). As at 1960s, *in vivo* cataract studies had started, employing radiation and other chemical agents such as naphthalene, phenothiazines, and triparanol. One of the well-studied is the selenite cataract that is created by inoculation of sodium selenite into 10-day-old rat pups (Sheaer et al., 1992). The strength of this model includes the reproducibility and swiftness of cataractogeneis. Following the injection of sodium selenite severe nuclear cataract arises in a matter of 5 days, after which cortical cataract ensues several weeks later. The trait of the selenite model is elevated levels of calcium in the lens nucleus that leads to the formation of nuclear cataract. The elevated calcium levels activate the protease calpain II that partly degrades diverse lens proteins, including α- and β-crystallins. The selenite model has highlighted the role of proteolysis in cataractogenesis. This model has also added to facts on the role of oxidation in cataract formation (Mitton et al., 1995). Oxidative stress, as evidenced by decreased GSH and increased hexose monophosphate shunt action, occurs within the first day after selenite injection, and it is hypothesised that oxidative stress at the cell membranes accounts for the loss of normal calcium homeostasis. The selenite model has been used to test potential anti-cataract agents, including calpain inhibitors, anti-oxidants, and phase separation inhibitors.

Chapter Summary

The chapter began with some basic principles of light interaction with tissue. This was followed by literature review on some optical spectroscopic techniques and principles such as fluorescence phenomenon, Laser – induced fluorescence spectroscopy, infrared spectroscopy, Fourier transform infrared spectroscopy, attenuated total reflectance technique and spectral imaging used to characterize different materials and or samples. The last part discussed multivariate data analysis techniques, the crystalline lens and cataract.

CHAPTER THREE

RESEARCH METHODS

Introduction

The experimental set-up, methods and procedures for acquiring data (slit lamp images, spectral images, autofluorescence spectra and infra-red spectra) from lens tissues of Sprague-Dawley rats are presented in this chapter. The first part of the chapter looks at animal husbandry, the procedure involved in the induction of cataract to the eye lens of Sprague – Dawley rats and lens tissue preparations. The first part also involves the procedure for acquisition of slit lamp images using a slit lamp microscope. The second and third parts of this chapter focuses on experimental methods and procedure for acquisition of spectral images and autofluorescence spectra using a multispectral light emitting diode (LED) imaging microscope system (MSLEDIM) and laser-induced fluorescence spectroscopy technique respectively. Finally, infra-red spectral acquisition from lens tissues using Attenuated Total Reflectance Fourier transform infra-red spectroscopy technique (ATR-FTIR) is presented in the last part.

Sprague – Dawley Rats and Husbandry

Ten-day-old Sprague-Dawley rat pups of either sex with mean weight of 24.29 ± 2 g were used for this research work. The pups together with their mothers were housed in cages with soft wood shavings as bedding as shown in Plate 1. The rats were monitored under ambient laboratory conditions (temperature 28 ± 2 °C, relative humidity 60–70 %) and a normal light–dark cycle at the animal house of the School of Biological Sciences, University of

Cape Coast. The mothers were fed on a normal commercial pellet diet (Agricare Ltd, Kumasi, Ghana) and had access to water *ad libitum.*

Plate 1: Photograph of Sprague – Dawley Rats and Pups in One of the Cages at the Animal House of the School of Biological Sciences, University of Cape Coast, Cape Coast.

Selenite - Induction of Cataract in Rat Pups and Digital Slit Lamp Image Acquisition

A total of 270 pup rats were put into six (6) groups consisting of 45 pup rats per group. Three (3) groups (Group A1, Group A2 and Group A3) were kept as control while the other three (3) groups (Group B1, Group B2 and Group B3) were injected subcutaneously daily with 15 μmolkg^{-1} sodium selenite Na_2SeO_3 (Sigma Aldrich, Germany) in normal saline on the 11th and 12th day respectively. The groups (Group A's and Group B's) were monitored till the 30th day. On the 31st day, the crystalline lens of Group Bs were assessed for cataract development using a digital slit lamp microscope (SLM Ophthalmic slit lamp microscope SLM-4ER).

In order to assess and verify the degree of cataract development in the Group Bs, image of each lens was captured using the slit-lamp microscope after the lenses had been dilated with 1% tropicamide ophthalmic solution (Akorn Inc., lake Forest, USA). Direct illumination technique followed by the parallelepiped was used in the acquisition of the images. In acquiring the images of the cataractous lenses, the Sprague- Dawley rat's eye was placed in front of the microscope. A vertical slit beam of light from a halogen illumination bulb (German OSRAM Halogen Tungsten Lamp), of 1-2 mm in width, from the illumination part of the illumination system was incident on the lens of the rat at an angle of 45° from visual axis after the pupils of each lens has been dilated as described earlier. The illumination part of the system has a slit which controls the illumination width and reflecting mirrors to change the direction of the illumination beam with respect to the viewing system. With the help of a joystick (elevation knops) which controls the movement of the microscope in the forward, left, right or backwards direction in order obtain a sharp and focused image, the microscope was moved in all direction in order to obtain a well-focused image of the Group Bs lenses. The obliquely illuminated lens was then imaged with an external digital camera (Canon Powershot A800) situated on the visual axis which is fixed beneath the eye pieces. The eye pieces together with a magnification changer form the magnification part of the digital slit lamp microscope. Plate 2 shows a photograph of the Ophthalmic slit Lamp microscope system, with some major parts, which requires an input voltage of 220 V – 240 V and a power of 60 W whiles Plate 3 shows a photograph of the acquisition of the lens images from the Sprague-Dawley rats. The Slit lamp microscope system is housed at the Department of Optometry, School of Allied health Sciences, College of Health and Allied Sciences, University of Cape Coast.

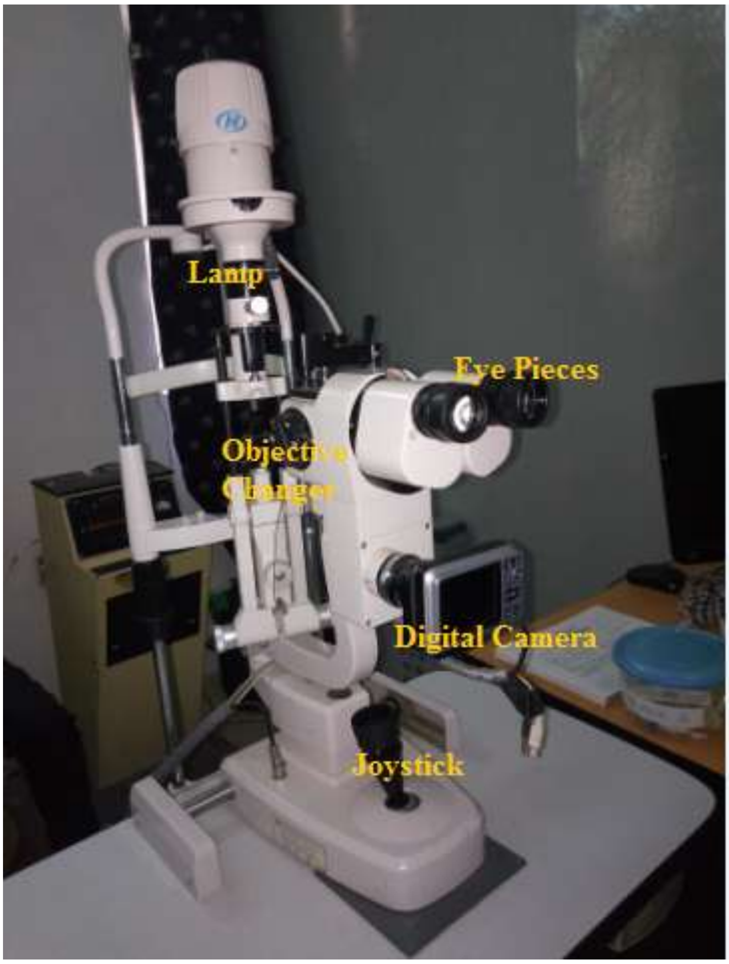

Plate 2: Ophthalmic Slit Lamp Microscope System Showing Some Major Parts Such as the Joystick, the Digital Camera, the Objective Changer, the Lamp and the Eye Piece.

Plate 3: Photograph Depicting the Ophthalmic SLM being used to Assess Cataract Development and Acquire Lens Images from the Sprague –Dawley Rats.

The Sprague- Dawley rats from the Group Bs were graded by two experts (Optometrist) from the Optometry Department of the school of Allied health Sciences, University of Cape Coast. The lenses of the rats were assessed and put into four grades. Table 1 shows the number (in percentage) of Group Bs assessed for grade 1 through to grade 4. In grading the cataractous lenses of Group Bs, slit lamp images were acquired in RGB format for each lens. The images were then saved for processing and analysis. A total of 240 cataractous lens images (60 images from each grade) were processed for analysis based on attributes such as integrated optical densities (IOD) of the lens images.

Table 1: Number of Group Bs Assessed for Cataract Development.

Groups	Grade 1 (%)	Grade 2 (%)	Grade 3 (%)	Grade 4 (%)
B1	11.1	11.2	33.3	44.4
B2	11.1	13.4	20.0	55.5
B3	11.1	17.8	37.8	33.3

Lens Tissue Preparation

The Spague –Dawleys rats in Group Bs with grade 4 cataractous lenses, henceforth referred to as Group BD's were sacrificed together with a selected number of those in Group As by ether inhalation, followed by intracardiac injection of pentobarbital. After enucleation, the lens tissues of Group A's and Group BD's were extracted and kept in different containers with formalin at room temperature.

The lens tissues from Group A1 and BD1 were used for multispectral imaging experiment where forty four point four percent (44.4 %) of Group A1 were selected to match up the number of Group BD1 lens tissues for tissue preparation. The lens tissues were fixed in 10 % phosphate-buffered paraformaldehyde, and embedded in paraffin. Sections of 3 μm thickness were made from each lens tissue and stained with hematoxylin and eosin (H&E) (Maloof et al., 2005) and fixed on microscopic glass slides for image acquisition. Similarly, same number of unstained sectioned lens tissues were also prepared for microscopic image acquisition.

The whole lens tissues from the Group A2 and BD2 were used for laser-Induced autofluorescence spectra measurement. Here fifty five point five percent (55.5 %) of Group A2 were also selected to match up the number of Group BD2 lens tissues for autofluorescence spectra measurement. Attenuated total reflectance Fourier transform infra-red spectroscopy (ATR-FTIR) measurement was performed with the final group of lens tissues. Thirty three point three percent (33.3 %) of Group A3 lens tissues were also selected to match up the number of Group BD3 lens tissues for infrared spectra measurement.

Multispectral Light Emitting Diode Imaging Microscope System

Multispectral light emitting diodes imaging microscope system (MSLEDIM) was used for image acquisition. The MSLEDIM system as presented in Opoku-Ansah et *al*. and Brydegaard et *al.* (Opoku-Ansah et al., 2012; Brydegaard et al., 2011), is housed at the Laser and Fibre Optics Centre (LAFOC), Department of Physics, School of Physical Sciences, College of Agriculture and Natural Sciences, University of Cape Coast, Cape Coast, Ghana. This MSLEDIM system employs nine (9) LEDs each in three (3) optical geometries (Reflection, transmission and Scattering), emitting a total of thirteen (13) spectral bands. One of the LEDs is a triple-band (470 nm, 525 nm and 810 nm) and two others are dual-bands (375 nm, 400 nm and 625 nm, 850 nm) whiles the remaining six are of single-bands (435 nm, 590 nm, 660 nm, 700 nm, 750 nm, and 940 nm). The spectra bands ranges from Ultra-Violet (UV) to Near Infrared (NIR).

The MSLEDIM system consists of mechanical, optical and optoelectronic components. The mechanical components are LED holders and a brass tube. The optical components are fibre ring, a ReflX objective, a beam splitter (BS), an optical diffuser and LEDs whereas the components making up the optoelectronic part are an imager, a (Data Acquisition) DAQ, current driver, multiplexer, LED battery and a stripboard. A laptop computer (a 32-bit Intel (R) Core (TM) 2 Duo CPU Toshiba Satellite Pro laptop with processing speed of 2.00 GHz) was used for controlling the signals from the camera and the DAQ. Plate 4 shows a photograph of the set- up of the MSLEDIM system showing some major components

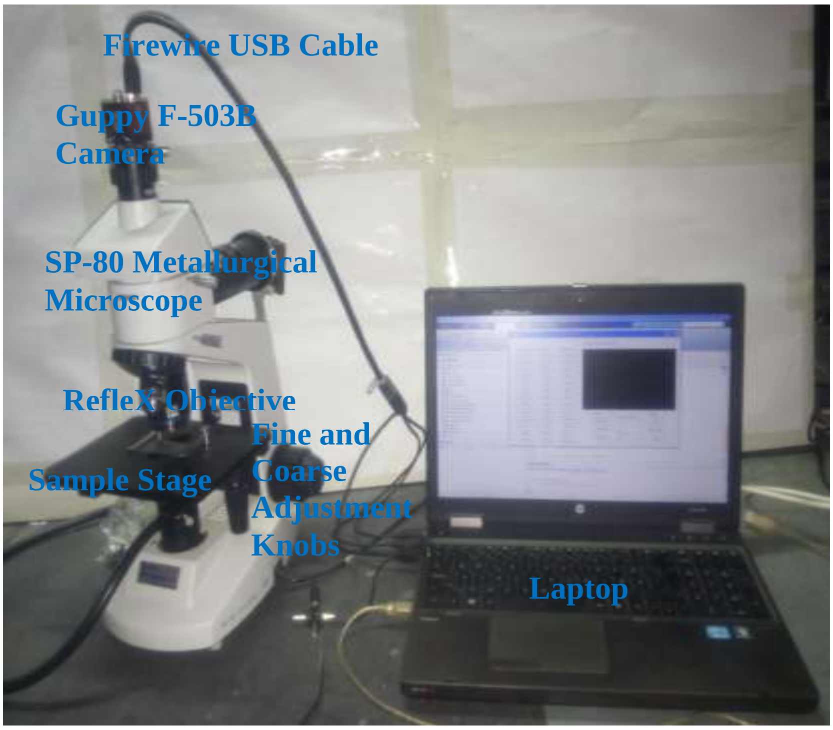

Plate 4: Photograph of the Multispectral Light Emitting Diode (LED) Imaging (MSLEDI) Microscope (MSLEDIM Set-Up) at the Laser and Fibre Optics Centre (LAFOC), Department of Physics, School of Physical Sciences, College of Agriculture and Natural Sciences, University of Cape Coast, Cape Coast.

Multispectral Image Acquisition

Multispectral images of the stained sectioned lens tissues, hence forth referred to as SSLT, were acquired in reflection, scattering and transmission modes using the MSLEDIM system. In acquiring the images, the power supply to the MSLEDIM system was checked with a multimeter to ensure that there was 9 V being supplied. A firewire universal serial buses (USBs) cable from the imager (Guppy F-503B camera) and the DAQ were plugged into their respective USB ports. The power supply and the laptop computer were then switched on, and a developed Matlab (R2014a Matlab 7.10.0, Mathworks Inc., USA) Graphical User Interphase (GUI) program as shown in Plate 5 was launched to control the LEDs, and imager for image acquisition (Opoku-Ansah, et al., 2017). In acquiring images in the reflection mode, one of the microscopic slides prepared from the Group BD1 SSLT was placed on the sample stage (SS) after which the reflection mode was selected from the *geometry icon*.

Light from 590 nm LED source was selected from the LED icon for focusing in reflection mode. The required gain and exposure time were set from the *gain* and *exposure time* icons (not shown). In order to focus on an image, the fine and coarse adjustment knobs of the MSLEDIM system were used interchangeably. In acquiring the image in the reflection mode, light from the LED sources was incidence on the beam splitter (BS) from which half of the light was reflected towards the Group BD1 SSLT on the SS and the other half transmitted. The reflected light then illuminates the Group BD1 SSLT on the SS and backscattered after passing through the ReflX objective. The backscattered light was collected again through the Reflx towards the BS and brought onto focus by a convex lens towards the imager for an image to be acquired. Images were saved in a folder as *tagged image file* (TIF) by selecting *save image* icon.

Plate 5: Graphical User Interface (GUI) of Matlab Program for Controlling the Light Emitting Diodes (LEDs) and Capturing Images from the Imager with an Image from the 590 nm LED.

Similarly, light from the LEDs in transmission mode is scattered by a diffuser and focused by a convex lens unto the Group BD1 SSLT where the light is transmitted through it on SS. The transmitted light is focused by another lens towards the imager to be detected and captured by the imager using the laptop computer. This procedure for acquiring images from a sample in transmission mode is described in details elsewhere (Opoku-Ansah et al., 2014).

In order to acquire images in the scattering mode, the *geometry icon* was then changed to scattering mode. The scattered light, as a result of the optical diffuser, illuminates the Group BD1 SSLT on the SS. The scattered light was collected and focused by the ReflX objective towards the imager for image signals to be detected. One after the other, the LED light sources were again selected, one at a time with the aid of *add line* icon. The images were acquired using all the 13 spectra bands. This was repeated for the other Group BD1 SSLT as well as those of Group A1.

All the images were acquired in grayscale format. Three (3) images were acquired from each of the 20 SSLT of Group BD1 using all the 13 spectra bands in the transmission mode. This was repeated in the reflection as well as the scattering mode. For each mode, seven hundred and eighty (780) images were obtained from the SSLT of Group BD1 and the image acquisition process was repeated for SSLT of Group A1. The described procedure for acquiring the images was repeated for obtaining grayscale images of unstained sectioned lens tissues (USLT) of Group A1 and Group BD1.

Laser-Induced Autofluorescence Experimental Set-up

The laser-induced autofluorescence set-up as shown in Figure 10 consists of a continuous wave (cw) blue diode laser source (445 nm) (O-Like, China), a mirror, a fibre port micropositioner (PAF-SMA-5-B, Thorlab), a bifurcated optical fibre probe (R400-7-VIS-NIR, OOS 000379-20, Ocean Optics), high pass absorptive edge filter (GG445), a microscope objective (O4OAS016, Melles Griot), spectrometer from ocean optics (USB 2000 Spectrometer, Ocean Optics) and control unit. A photograph of the set-up used for autofluorescence spectra data acquisition is shown in Plate 6. The 445 nm cw laser is equipped with a laser driver which requires an input voltage and current of 12 V and 2 A respectively with TTL modulation of 0 to 20 KHz to operate.

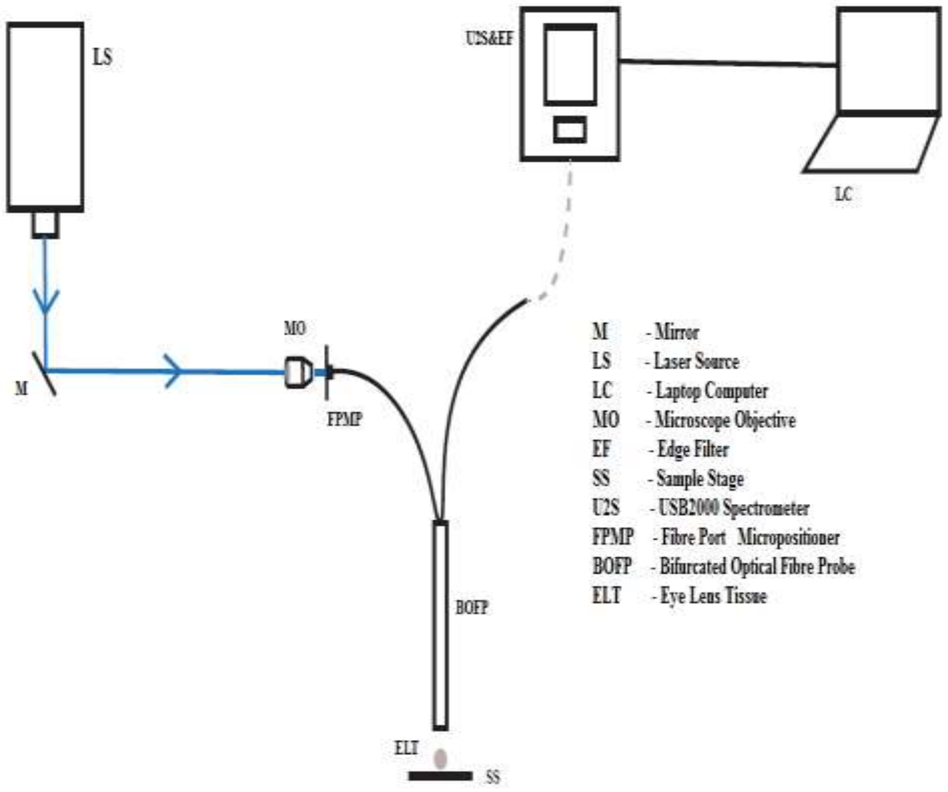

Figure 10: Schematic Diagram of the Laser-Induced Autofluorescence Set–Up for Acquiring Autofluorescence Data from Eye Lens Samples.

The fibre port micropositioner was used to provide an easy platform which aids the coupling of light into the bifurcated optical fibre. The port has a six-degree of freedom fibre collimator and coupler (5 axes plus rotation). Using the fibre port micropositioner enabled stable alignment and maximum coupling of light into the bifurcated optical fibre probe which was achieved with the aid of a 40x magnification with 0.65 NA microscope objective (040AS016, Melles Griot). The USB2000 spectrometer had been configured into a plug-and-play mode with a 2048-element linear silicon CCD array detector (SonybILX511) and a grating system which is optimized for UV-VIS-IR detection.

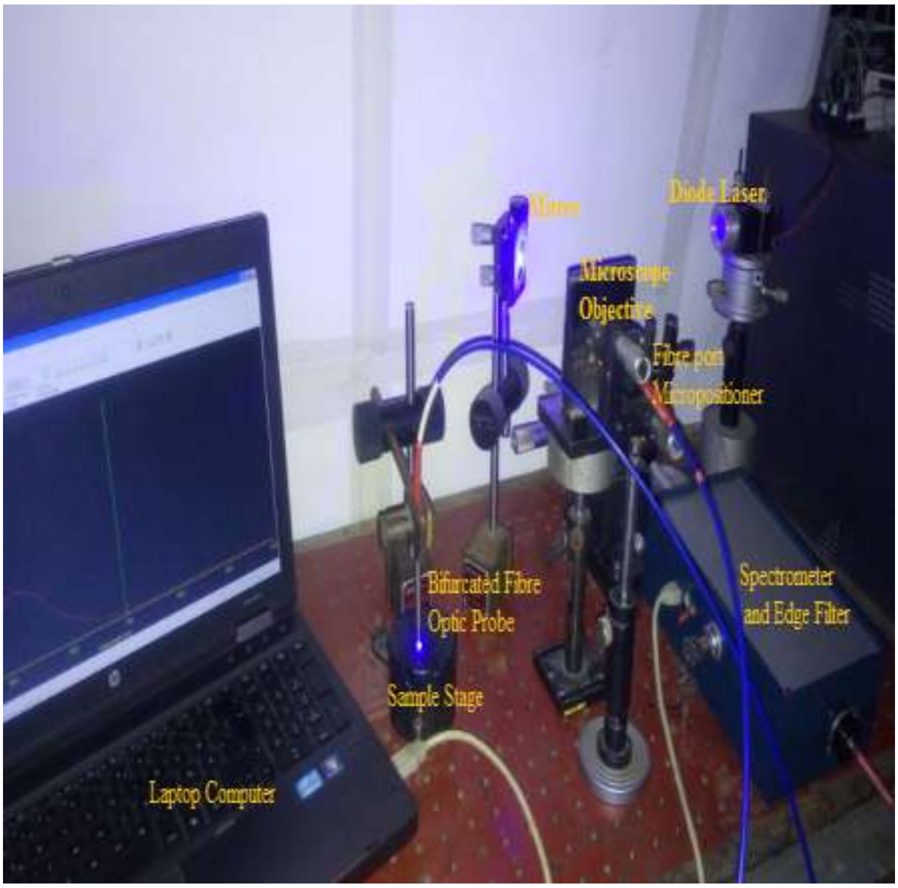

Plate 6: Photograph Showing the Components of the Laser – Induced Autoflourescence (LIAF) Set-Up forAcquiring Autofluorescence (AFS) Spectra Data.

The USB2000 plugs into the USB port of the laptop computer. Wavelength calibration, which was unique to the USB2000 spectrometer, had been programmed into its memory chip (EEPROM). 00IBase32 software (Ocean Optics Inc.) read these values from the output of the spectrometer.

The wavelength calibration coefficients and the spectrometer serial number installed on the memory chip is enabled by this software for the computer to communicate with the USB2000 spectrometer. The software which is a 32-bit user-customizable and advance acquisition program enables a real time display of its data. The OOIBase 32 software helps in evaluating the effectiveness of the experimental setup, data processing selections, making changes to the parameters instantly and ultimately save data either manually or automatically. The software allowed the usage of process functions such as signal averaging and boxcar pixel smoothing. Autofluorescence signals were acquired in the scope mode for full spectra acquisition. This autofluorescence set-up was be used to detect and measure fluorescence of both cataractous and healthy lens tissues.

Autofluorescence Spectra (AFS) Acquisition

The output laser beam of the diode laser source was directed by the mirror and guided unto the lens tissues by a bifurcated fibre optics probe (R400 – 7, Ocean Optics, USA) via a microscope objective (040AS016, Melles Griot) and a fibre port micropositioner (PAF-SMA-5-B, Thor lab). Laser-induced autofluorescence was emitted spatially in all directions from the lens tissues and a fraction of it was collected by the same bifurcated fibre optic probe and guided to an Ocean Optics spectrometer (USB 2000, Ocean Optics, USA) through an absorptive edge filter (GG445; $\lambda > 445$ nm) which cut off the excitation light source. The AFS was then displayed on the monitor with the aid of the OOI Base 32 software.

In acquiring the AFS, the lens tissue from Group BD2 was put onto the sample stage and its spectra was recorded using the cw 455 nm diode laser source. For each of the Group BD2 lens tissue, a total of 100 spectra were recorded for each lens tissue at a room temperature of 24 ^{o}C and later was used for analysis. The same procedure was repeated in acquiring AFS from the Group A2. AFS from Group A2 and Group BD2 was also acquired using a 405 nm cw diode laser.

Attenuated Total Reflectance Fourier Transform Infra-Red (ATR-FTIR) Spectra Data Acquisition

ATR-FTIR spectra were recorded using Spectrum Two FTIR spectrometer (Spectrum two FT IR spectrometer, PerkinElmer, USA), which has 4 cm^{-1} spectra resolution and controlled by spectrum software PerkinElmer. The spectrometer operates by measuring the changes that occur in an internally reflected IR beam when the beam comes into contact with a sample under investigation. An infrared (IR) beam is directed onto an optically dense diamond crystal with a high refractive index where an evanescent wave is created. The wave extends beyond the surface of the diamond crystal and then into the sample held in contact with the crystal.

The sample then absorbs energy in the region of IR spectrum which results in the attenuation of the evanescent wave. The attenuated beam returns to the crystal and then exits at the opposite end of the crystal where it is directed to the detector in the IR spectrometer. An interferogram signal is then recorded by the detector which generated into an IR spectrum. Figure 11 shows a typical ATR optical system which shows a ray path through the system. The IR radiation is redirected by five different mirrors before the radiation incidence on the crystal and continues towards the detector. The setup allows for the IR radiation to probe molecules at the interface of the crystal.

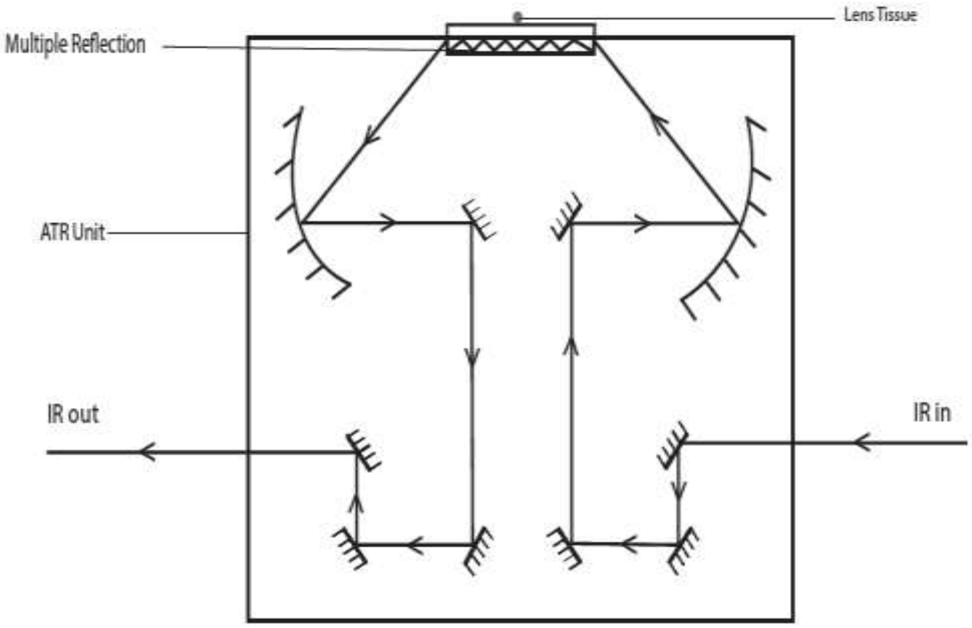

Figure 11: ATR-FTIR Optical System Ray Path Trajectory.

Infra-Red Spectra Acquisition

Infra-red spectra, in the range 8300 cm^{-1} – 350 cm^{-1}, with 1 cm^{-1} of spectral resolution, were recorded using the ATR-FTIR spectrometer system. Lens tissue samples from Group BD3 were pressed unto the diamond crystal of the ATR to ensure maximum contact. For each spectrum, thirty-two (32) scans were co-added to represent the average spectrum obtained for each. The procedure was repeated to obtain IR spectra from Group A3 lens tissues. A photograph of the spectrometer used to measure the IR spectra is shown in

Plate 7.

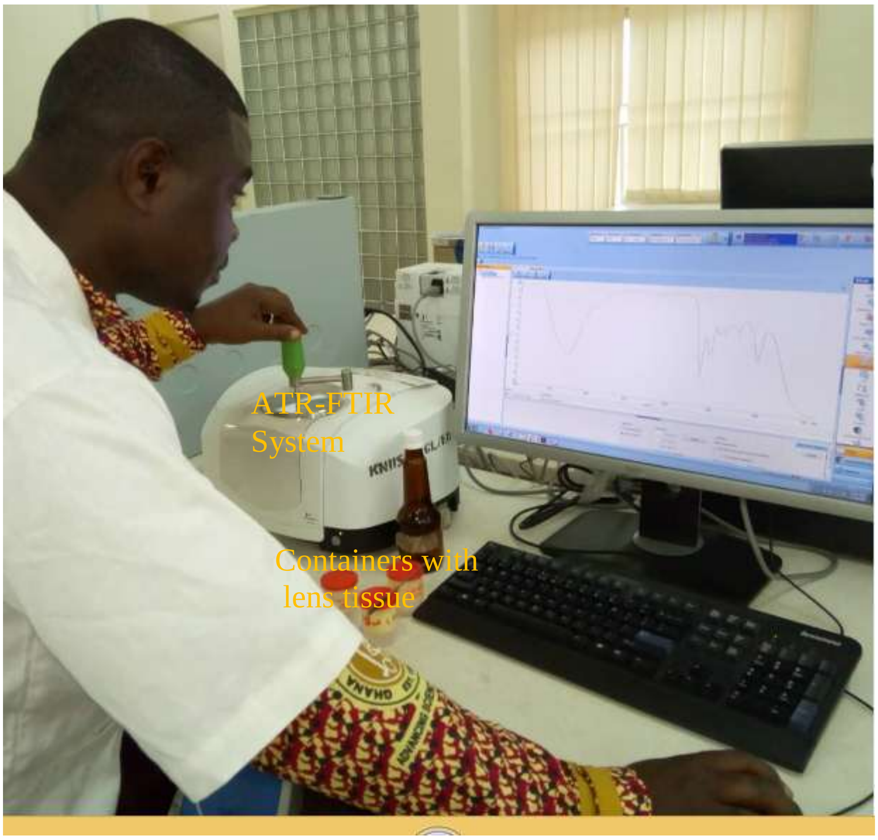

Plate 7: Photograph Depicting the Acquisition of Infrared Spectra from Eye Lens Tissues using Perkin Elmer Spectrum Two ATR_FTIR Spectrometer.

The autofluorescence spectra data from the laser-induced autofluorescence measurement, the infrared spectra data from the ATR-FTIR measurement, the images obtained from the MSLEDI microscope and the SLM Ophthalmic microscope were imported into Matlab platform and other application softwares from the folders in which they were saved for further analysis in order to characterize the cataractous lenses and the lenses from the control, thus healthy lenses. Multivariate analysis were done with the aid of developed codes in Matlab and attributes based on integrated optical density (IOD) (average intensity over density) were retrieved from the slit lamp images using *Image Pro Plus 5.0* software (Media Cybernetics, USA), version 3.1 for windows 3.0 which is dynamically linked to Microsoft's Excel.

Chapter Summary

This chapter described the experimental set-up, methods and procedures used in acquiring data (slit lamp images, spectral images, autofluorescence spectra and infra-red spectra) from lens tissues of Sprague-Dawley rats. Animal husbandry was described in the first part of the chapter which was followed by the procedures involved in the induction of cataract to the eye lens of Sprague – Dawley rats and acquisition of slit lamp images using a slit lamp microscope. Experimental methods and procedure for acquisition of spectral images, autofluorescence spectra and infra-red spectral using a multispectral light emitting diode (LED) imaging microscope system (MSLEDIM) and laser-induced fluorescence spectroscopy technique Attenuated Total Reflectance Fourier transform infra-red spectroscopy technique (ATR-FTIR) were then described.

CHAPTER FOUR

RESULTS AND DISCUSSIONS

Introduction

This chapter presents results, analysis and discussions on the applied experimental optical spectroscopic techniques for discriminating cataractous lens tissues from the healthy lens tissues as well as characterizing cataractous lenses of Sprague –Dawley rat. The first part of this chapter presents results, analysis and discussions of the slit lamp images acquired with the digital slit lamp microscope SLM – 4ER for the grading of cataractous lenses, the second part of this chapter presents results, analysis and discussions on spectral images acquired using the multispectral light emitting diode (LED) imaging microscope (MSLEDIM) system and the third part analyses and discusses the results from the Laser -induced autofluorescence excitation on both healthy and cataractous lenses. The fourth and final part presents results, analysis and discussions on infrared spectra obtained from Attenuated Total Reflectance Fourier Transform infra-Red (ATR - FTIR) spectroscopy measurement.

Grading of Cataract from Slit Lamp Images of Sprague–Dawley Rat Lenses

Slit lamp images of the cataractous lenses for four different grades obtained with the slit lamp microscope are shown in Figure 12. As cataract develops, it becomes denser and it involves greater part of the lens. This results in progressive clouding of the lens as seen in Figures 12 (a-d). Cataract develops from mild to moderate through to pronounce and finally to severe. Figure 12 (a) shows one of the mild cataractous lens images. It can be observed that a small portion of the lens is cataractous and that indicates an early stage of a cataractous lens. One of the moderate cataractous lenses is shown in Figure 12 (b). It can be seen from the figure that the portion of the lens that is cataractous is bigger compared to the mild cataractous lens.

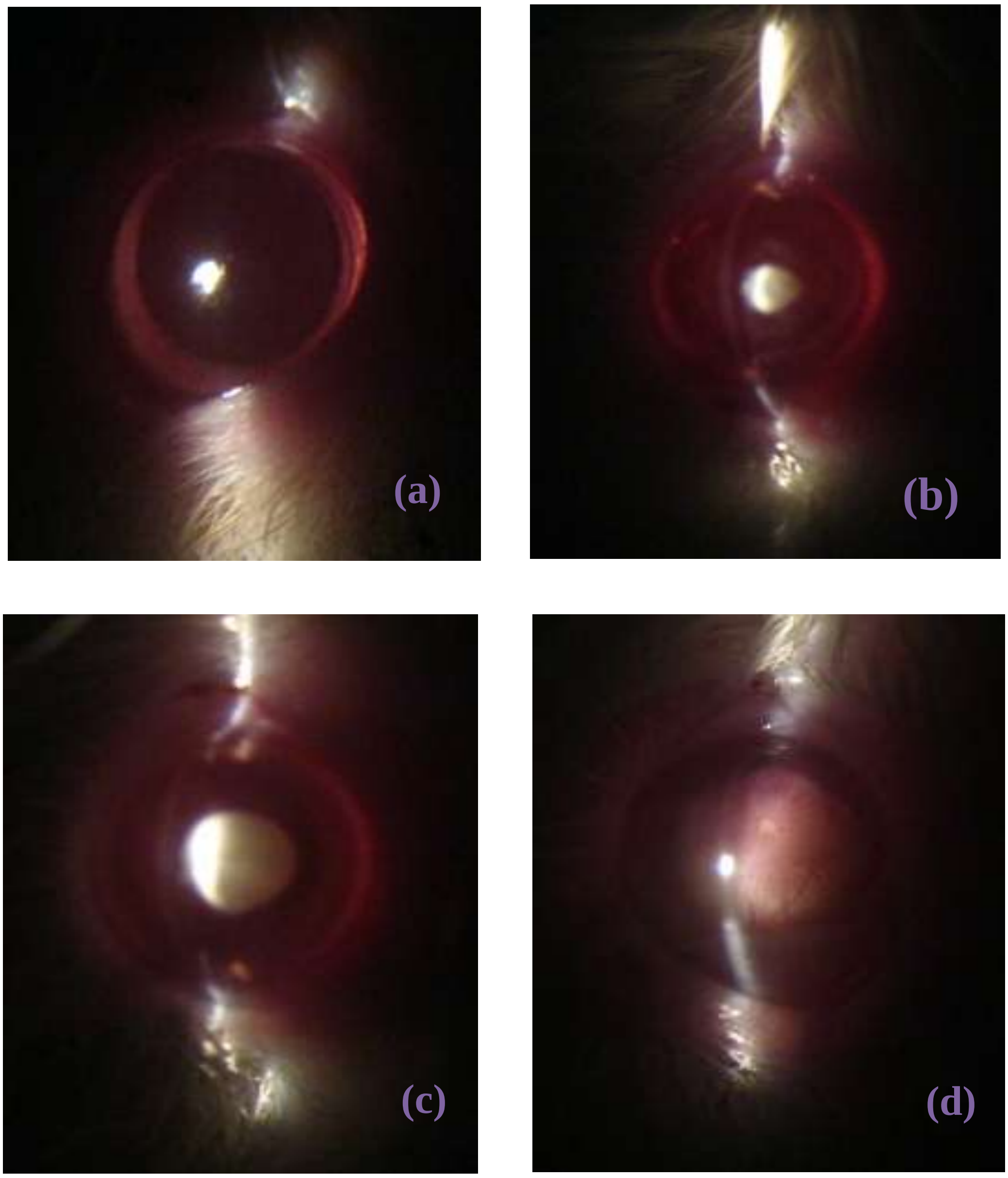

Figure 12: One of the Slit Lamp Images of Cataract from Sprague – Dawley Rats from Each Grade with (a) as Mild, (b) as Moderate, (c) as Pronounce and (d) as Severe.

The portion of the lens clouded with cataract for moderate cataractous lenses are smaller compared to that of the pronounce cataractous lenses. One of the pronounce cataractous lens image is shown in Figure 12 (c). It can be observed that the cataractous portion of the lens is bigger than that of the moderate cataractous lens but smaller compared to the severe cataractous lens with one of the lens images shown in Figure 12 (d).

In view of this, the slit lamp images were imported into *Image Pro Plus 5.0* software (Media Cybernetics, USA), version 3.1 for windows 3.0) for processing and analysis to obtain integrated optical densities (IOD) of the lenses in the images. To obtain the IOD of the graded cataractous lenses, a standard elliptical area of interest (AOI) mask was defined to encompass the lens image. The masked lens image was then converted to an object after which the IOD values were retrieved from the lens image. The standard elliptical mask was then saved and used to define the AOI for all the other lens images. This process was repeated for all the other lens images The *Image Pro* is dynamically linked to Microsoft’s Excel where the data was saved for further analysis. A structure chart showing the process for obtaining the IOD is shown in Figure 13.

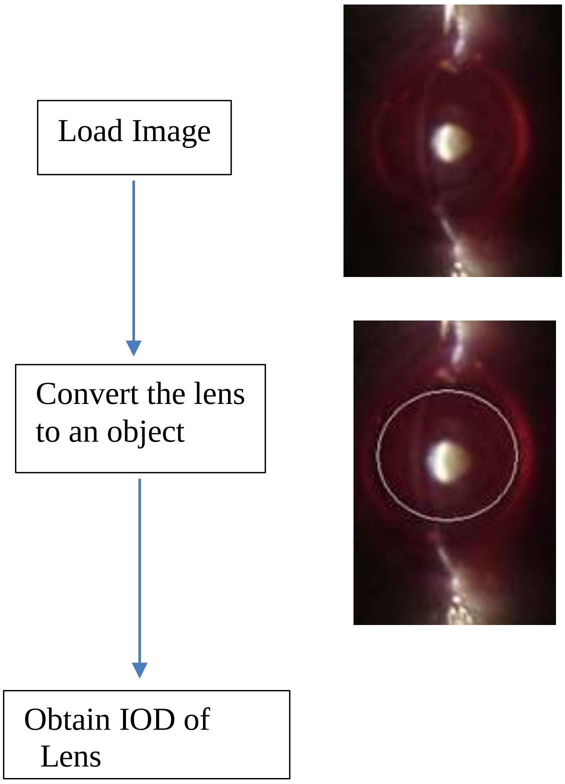

Figure 13: Structure Chart for Processing the Slit Lamp Images using Image Pro-Plus Software.

Histograms representing the number of cataractous lenses counted from the optical attribute (IOD) were plotted with the aid of Origin Pro 9.1 software. Figures 14-17 show plots of the histograms fitted with a Gaussian curve representing the distribution of IOD for the grade 1, grade 2, grade 3 and grade 4 cataractous lenses respectively. Figures 14-17 show plots of the IOD in the abscissa against counted grade 1, grade 2, grade 3 and grade 4 cataractous lenses in the ordinate respectively.

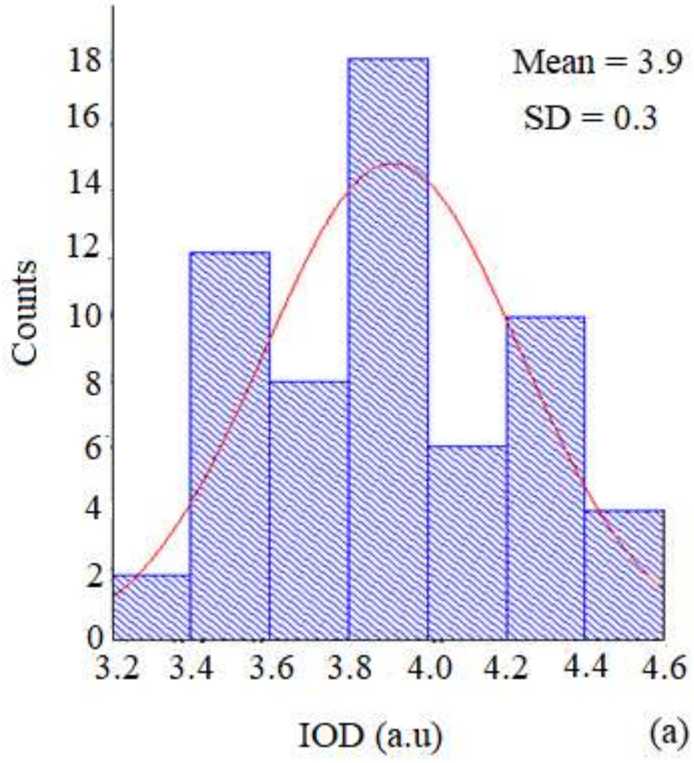

Figure 14: Histograms Representing the Distribution of Integrated Optical Density (IOD) for Grade 1 under Gaussian Fit Curve.

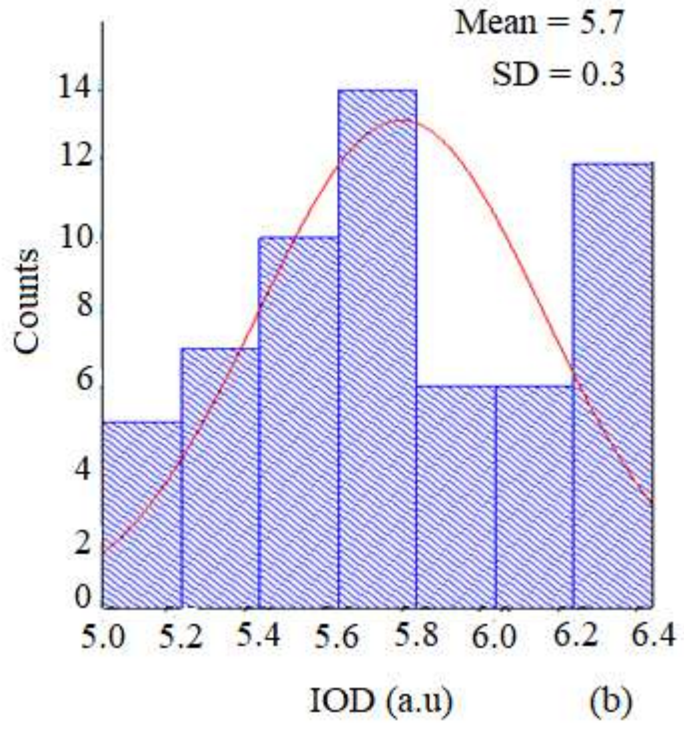

Figure 15: Histograms Representing the Distribution of Integrated Optical Density (IOD) for Grade 2 under Gaussian Fit Curve.

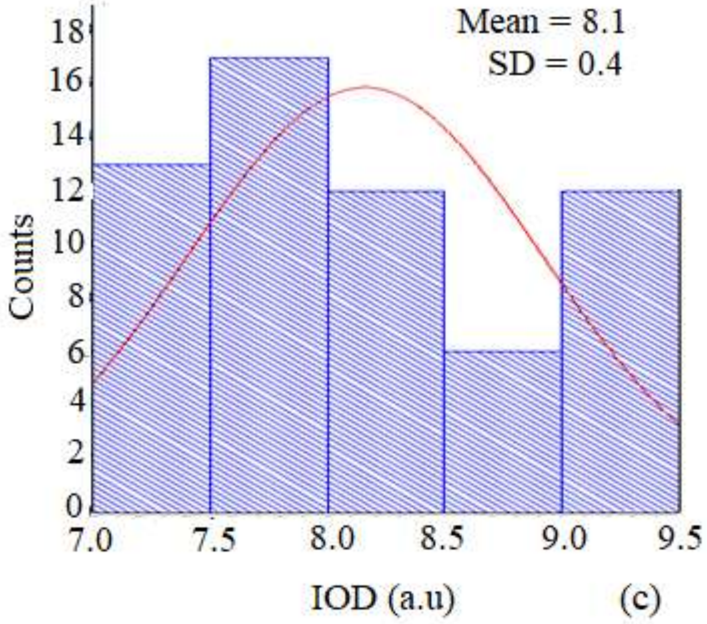

Figure 16: Histograms Representing the Distribution of Integrated

Optical Density (IOD) for Grade 3 under Gaussian Fit Curve.

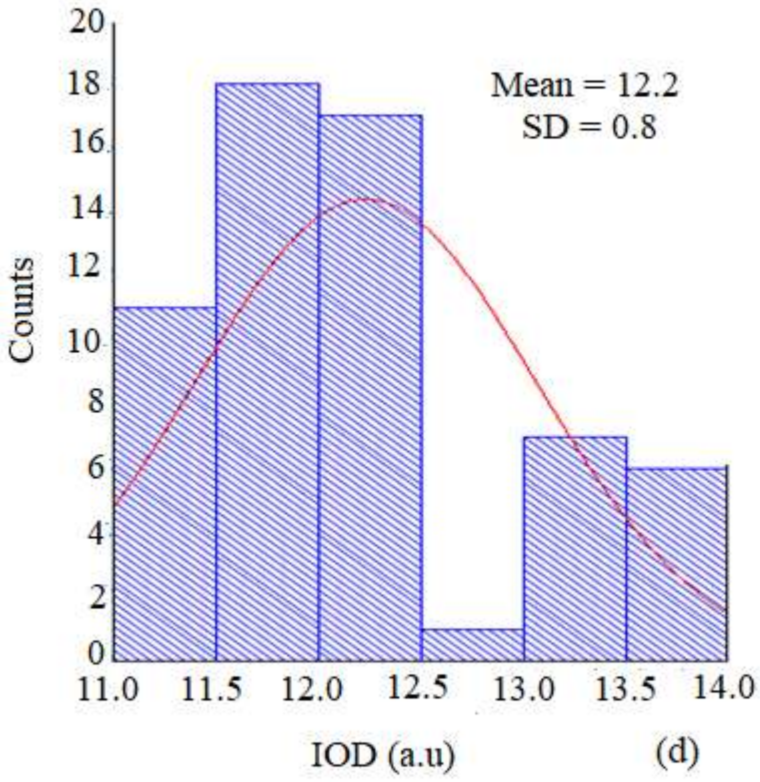

Figure 17: Histograms Representing the Distribution of Integrated

Optical Density (IOD) for Grade 4 under Gaussian Fit Curve.

The Gaussian curve to the histograms exhibits normal distribution of image intensities of cataractous lenses representing the IOD data. It can be observed from Figure 14 that the grade 1 cataractous lenses show IOD values ranging between 3.2 a.u and 4.6 a.u with majority of the cataractous lenses counted between 3.8 and 4.0. The IOD values for grade 2 cataractous lenses ranges between 5.0 a.u and 6.4 a.u with majority of them counted between 5.6 a.u and 5.8 a.u as can be seen in Figure 15. Figure 16 shows IOD values of grade 3 cataractous lenses ranging between 7.0 a.u and 9.5 a.u with majority between 7.5 a.u and 8.0 a.u. As can be observed in Figure 17, the values of IOD for grade 4 cataractous lenses ranges between 11.0 a.u and 14.0 a.u. The majority of grade 4 cataractous lenses were counted between 11. 5 a.u and 12.5 a.u.

The mean IOD values obtained for grade 1 through to grade 4 were found to be 3.9 ± 0.3 a.u, 5.7 ± 0.3 a.u, 8.1 ± 0.4 a.u and 12.2 ± 0.8 a.u respectively. The mean IOD values for the cataractous lenses were found to increase as the cataract develops from grade 1 which is mild through to grade 4 which is severe. This suggest that increased in IOD values correspond to increase in the severity of cataract development. Figure 18 shows a plot of mean IOD values as ordinate with the grades of cataract development as abscissa. The figure shows variation in the mean IOD values of the cataractous lenses. There is a positive correlation between the mean IOD values and the grades of cataracts as can be observed from the figure. The mean IOD of cataractous lenses were found to increase with severity. With the help of the graph in Figure 18 and the generated equation one can obtain mean IOD value knowing the specific grade of cataractous lens and vise versa. Differences in the range of values of IOD as well as the mean IOD values may offer potential optical indicators for assessing the level of cataract development.

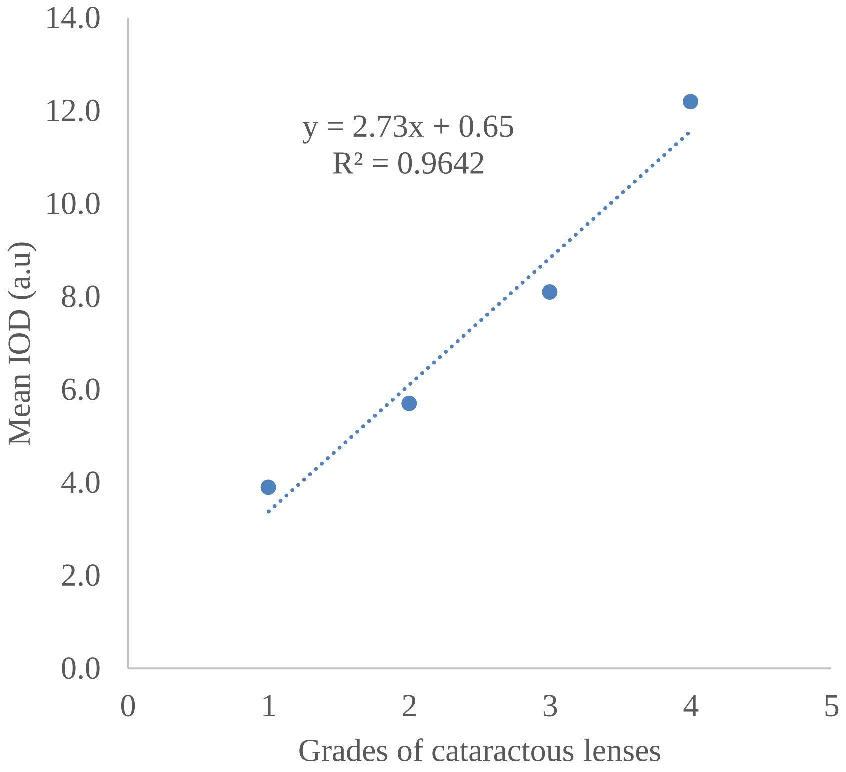

Figure 18. Variation in Mean of Integrated Optical Density (IOD) for the Four Grades of Cataractous Lenses.

Discrimination of Stained and Unstained Sectioned Lens Tissue of Cataractous Lenses (Group BD1) from the Healthy (Group A1)

The images shown in Figures 19 and 20 are grayscale images of stained sectioned lens tissues (SSLT) of Group A1 (healthy lens) and Group BD1 (cataractous lens) respectively captured with 400 nm, 435 nm, 470 nm, 525 nm, 590 nm, 625 nm, 700 nm and 750 nm LED sources in transmission, reflection and scattering modes. The images were taken with the same dimensions but depicted different grayscales. The Group A1 images show no evidence of disruption of the fibre cells that aid in more transmission and

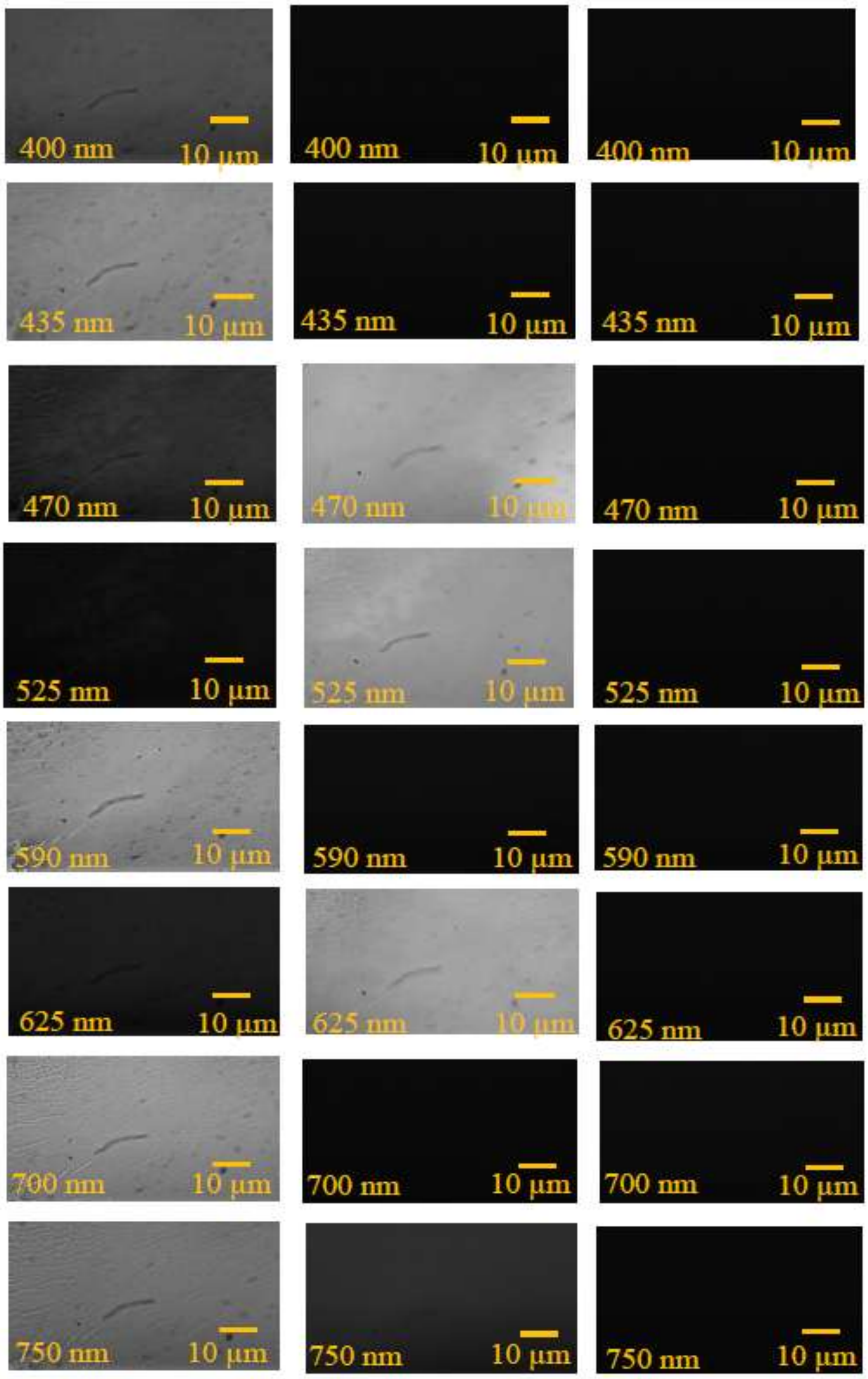

Figure 19: Grayscale Images of Group A1 SSLT Captured in Transmission Mode (First Column), Reflection Mode (Second Column) and Scattering Mode (Third Column) using the MSLEDIM System at 400 nm, 435 nm,470 nm, 525 nm, 590 nm, 625 nm, 700 nm and 750 nm Spectral Band.

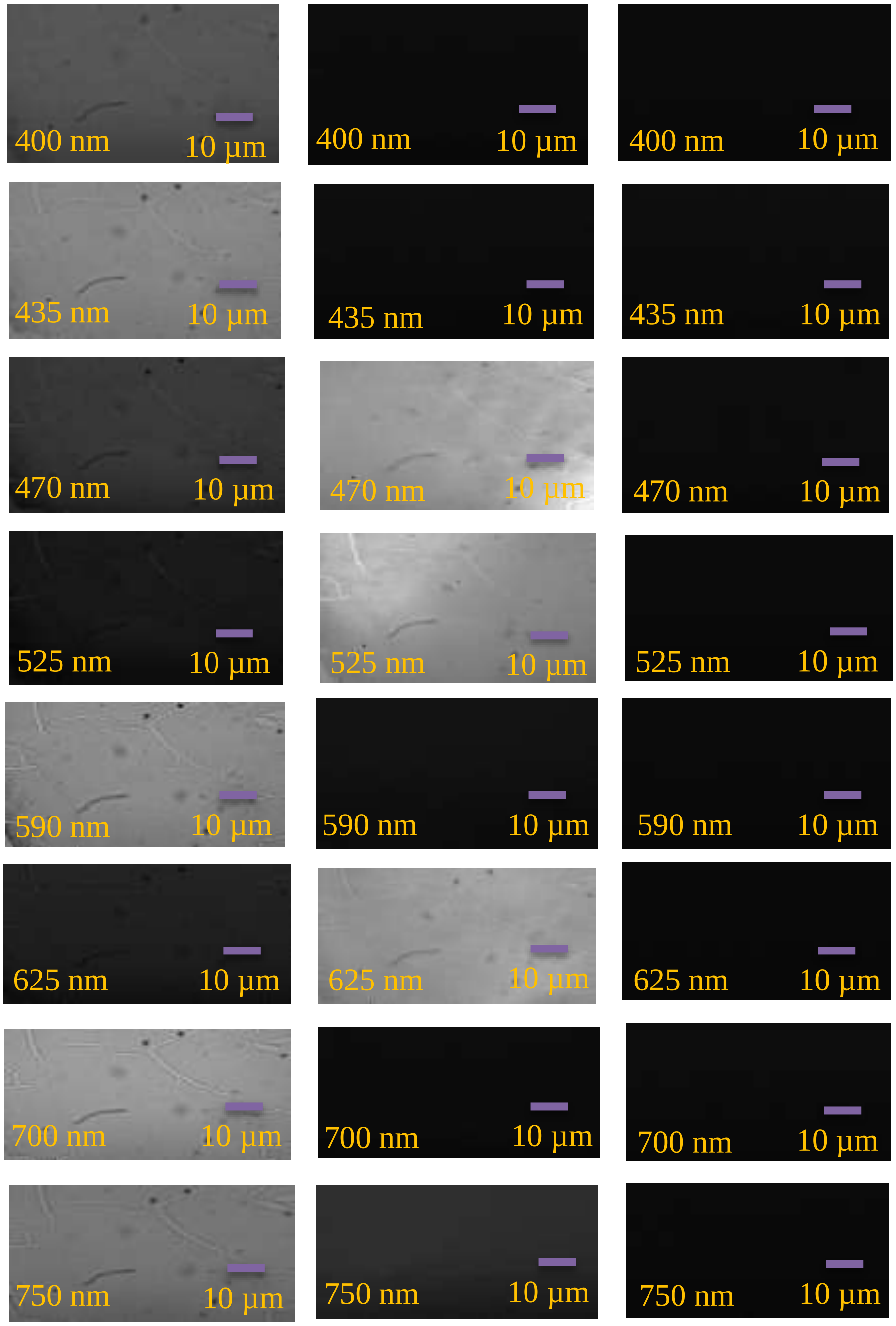

Figure 20: Grayscale Images of Group BD1 SSLT Captured in Transmission Mode (First Column), Reflection Mode (Second Column) and Scattering Mode (Third Column) using the MSLEDIM System at 400 nm, 435 nm,470 nm, 525 nm, 590 nm, 625 nm, 700 nm and 750 nm Spectral Band.

reflection of the light and this contributes to the lens' transparency. The spots found in the images are artefacts.

Since the discrimination between the two groups (Group A1 and Group BD1 of SSLT), in transmission, reflection and scattering modes, cannot be easily assessed by observation of the grayscale images, their averaged pixel intensities in each mode were extracted. The averaged pixel intensity values from Group A1 and BD1 SSLT images in transmission mode are shown in Figure 21. Pixel intensities from the transmitted light from Group A1 SSLT depicts higher values compared to that of Group BD1. This can be attributed to the transparent nature of the Group A1 SSLT. The transparency of the lens depends on its avascularity, paucity of organelles, narrow inter-fibre spaces and the regular organization of its cells and proteins (Bassnett &Vrensen, 2011). At the cellular level, there is limited light-scattering by cellular organelles, which are relatively sparse in the central epithelium and displaced to the equator in the fibres, away from the light path. Within the fibre cells, the crystallins exist with a short-range order less than the wavelength of light, similar to that of glass. This is due to the small size of the protein molecules, less than 10 nm in diameter, and their close packing at high concentration (Michael & Bron, 2011)

The average pixel intensities from 5 spectral bands, 435 nm, 590 nm, 700 nm, 750 nm and 810 nm are observed to be higher (> 100 a.u) in images of both the Group A1 and BD1 SSLT compared to the other spectral bands. This indicates that the SSLT can transmit enough light in all these spectral bands but much higher from the 5 spectra bands (435 nm, 590 nm, 700 nm, 750 nm and 810 nm). The lower opacification of Group BD1 SSLT can be attributed to massive insolubilization of the soluble protein in the lens, which results in light scattering by the lens (David et al., 1987; Cenedella & Fleshner, 1992).

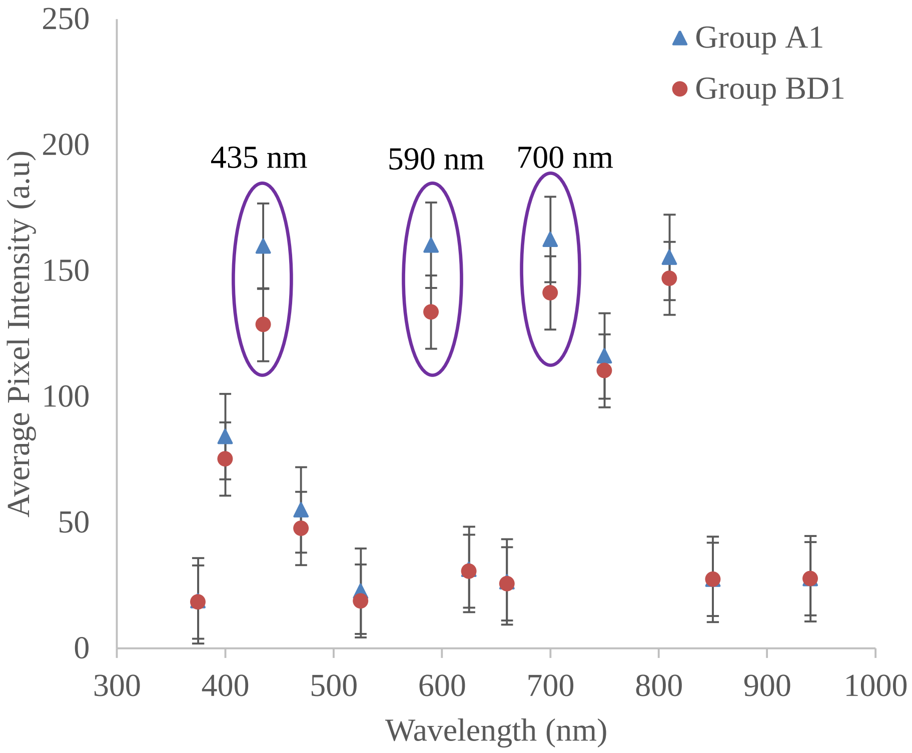

Figure 21: Average Grayscale Pixel Intensities Extracted from the Images of Group A1 and BD1 SLT Stained with H & E in Transmission Mode.

On the other hand, Group BD1 SSLT are characterized by increased absorption and scattering of light resulting in decreased transmission of light to the retina (Kessel et al., 2011). The average transmitted pixel intensities from 435 nm, 590 nm and 700 nm also showed substantial differences between Group A1 and BD1 SSLT. Average pixel intensity difference of 10 a.u was used as a criterion. This is an indication that these 3 spectra bands can be used to discriminate Group BD1 from A1 SSLT using averaged transmitted pixel intensity values.

The averaged pixel intensity values from images of Group A1 and BD1 SSLT in reflection mode are shown in Figure 22. The Figure shows that Group A1 SSLT are much higher at 3 specific spectral bands 470 nm, 525 nm and 625 nm than that of Group BD1. Also, these 3 spectral bands are higher (>150 a.u) in both the Group A1 and BD1 SSLT compared to the other spectral bands. This is an indication that the SSLT do reflect light intensities but much higher from 470 nm, 525 nm and 625 nm. This can be attributed to the smooth, clear and glassy nature of the Group A1 compared to the rough and wrinkled nature of the Group BD1 SSLT. The average pixel intensities from 470 nm and 625 nm also show differences between the Group A1 and BD1 SSLT. All the other spectral bands could not show significant differences between the Group A1 and BD1 SSLT. This is an indication that both 470 nm and 625 nm can be used as markers to discriminate Group A1 from BD1 SSLT using averaged pixel intensity values in the reflection mode.

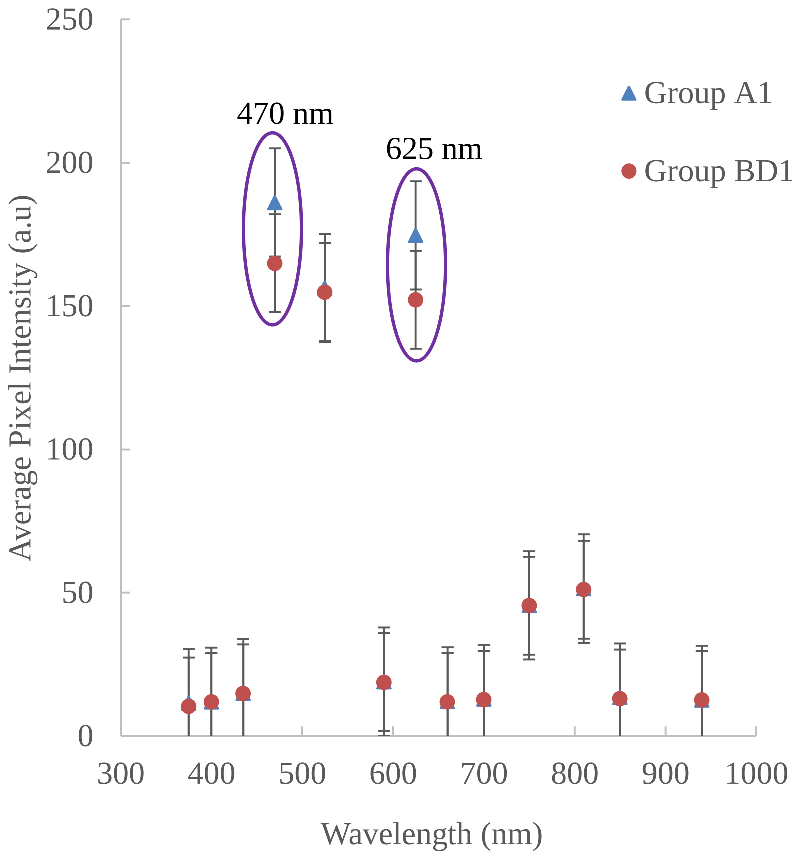

*F*igure 22: Average Grayscale Pixel Intensities Extracted from the Images of Group A1 and BD1 SLT Stained with H & E in Reflection Mode.

The averaged pixel intensity values from all the 13 spectral bands in the scattering mode, as shown in Figure 23, were low (< 20 a.u) in images of both Group A1 and BD1 SSLT. The intensity values ranges from 11 a.u to 17 a.u. These observations may be attributed to the poor scattering properties of the SSLT. This shows the SSLT of both groups exhibit similar characteristics when it comes to light scattering and it is independent of the spectral band. From the intensity values, shown in the insert in Figure 23, the differences between the two groups is insignificant for one to use scattering as a means for discriminating Group A1 from BD1 SSLT. Transmittance (T) and Reflectance (R) by Group A1 and BD1 SSLT were found to be spectra depended. From theory R + T =1 and since the scattering effect is small as compared to Transmittance and Reflectance from the SSLT, one can establish in this work that T =1 − (R * ρ) where ρ is a constant.

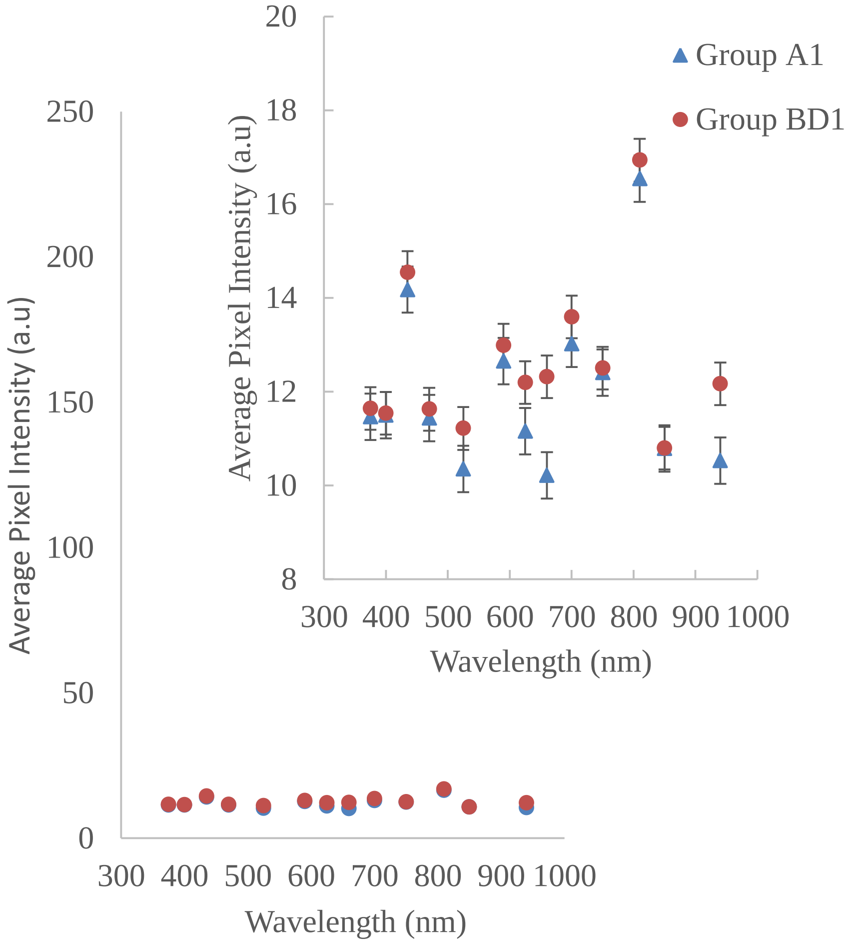

Figure 23: Average Grayscale Pixel Intensities Extracted from the Images of Group A1 and BD1 SLT Stained with H &E in Scattering Mode.

The same procedure used in capturing images of Group A1 and BD1 SSLT was used in obtaining the images of the unstained sectioned lens tissues (USLT) of Group A1 and BD1. The images shown in Figures 24 and 25 are grayscale images of USLT of Group A1 and Group BD1 respectively captured with 400 nm, 435 nm, 470 nm, 525 nm, 590 nm, 625 nm, 700 nm and 750 nm LED sources in transmission mode (first column), reflection mode (second column) and scattering modes (third column). As in the case of images from SSLT, Group A1 and Group BD1 images from USLT have the same dimensions but different grayscales. The same USLT were imaged in the reflection and scattering mode. The images captured in the scattering mode appear very dark as in the case of the SSLT. This is as a result of the fact that very low intensities of light were scattered by the USLT to the imager.

Apart from images captured at 375 nm (not shown), 525 nm, 625 nm, 660 nm (not shown), 850 nm (not shown) and 940 nm (not shown), the rest of the images captured in the transmission mode appear brighter compared to the rest of the images. This indicates that more light intensities were transmitted through the USLT of Group A1 and Group BD1 to the imager at 400 nm, 435 nm, 470 nm, 590 nm, 700 nm, 750 nm, and 810 nm. Similarly images captured at 470 nm, 525 nm and 625 nm in the reflection mode appear brighter compared to those captured at 375 nm (not shown), 400 nm, 435 nm, 590 nm, 625 nm, 660 nm (not shown), 700 nm, 750 nm, 810 nm(not shown), 850 nm (not shown) and 940 nm (not shown), as observed in the case of the SSLT. This goes on to suggest that more light was reflected to the imager at these three spectral bands (470 nm, 525 nm and 625 nm) than at the rest of the spectral bands.

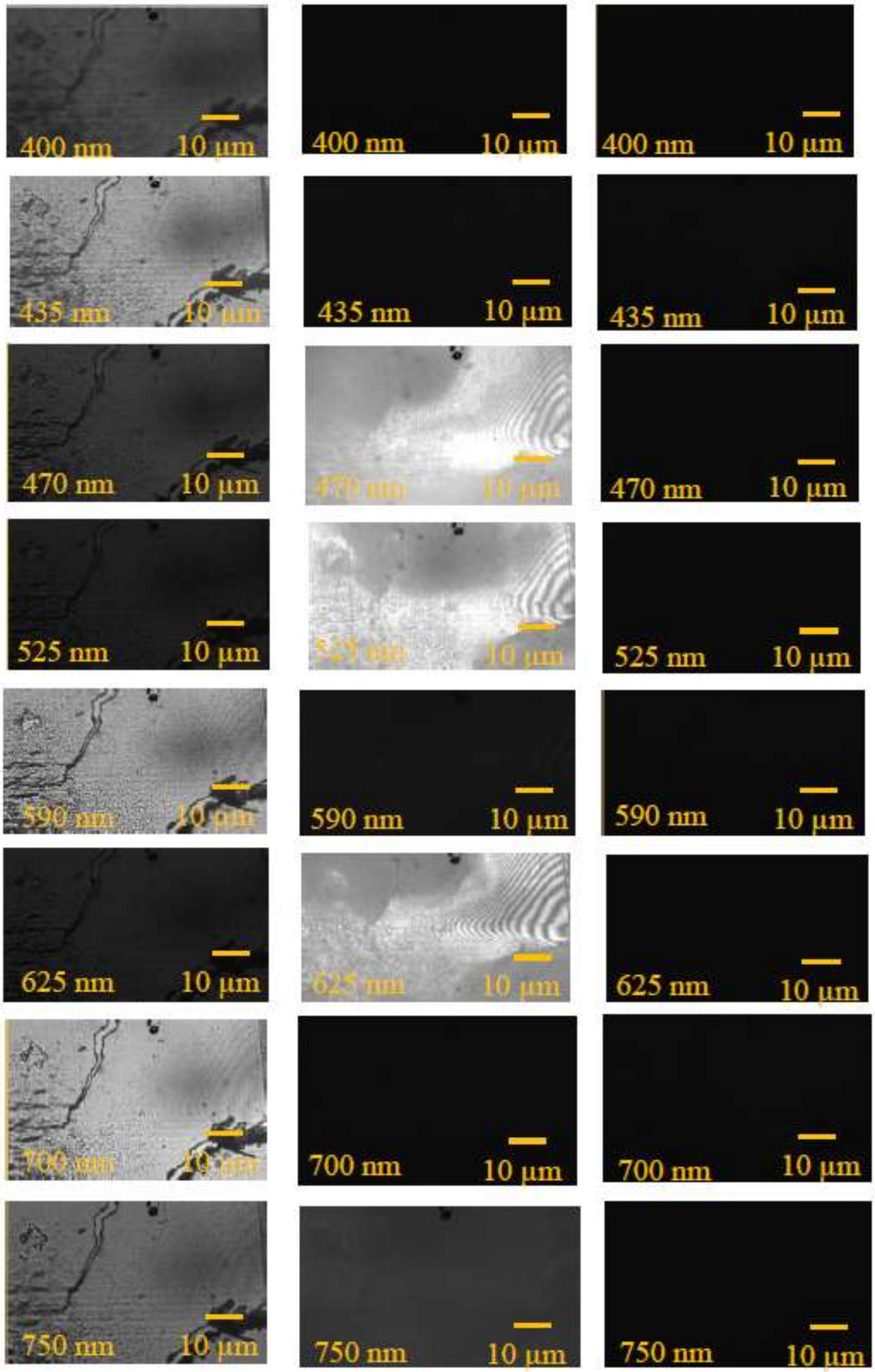

Figure 24: Grayscale Images of Group A1 USLT Captured in Transmission Mode (First Column), Reflection Mode (Second Column) and Scattering Mode (Third Column) using the MSLEDIM System at 400 nm, 435 nm,470 nm, 525 nm, 590 nm, 625 nm, 700 nm, and 750 nm Spectral Band.

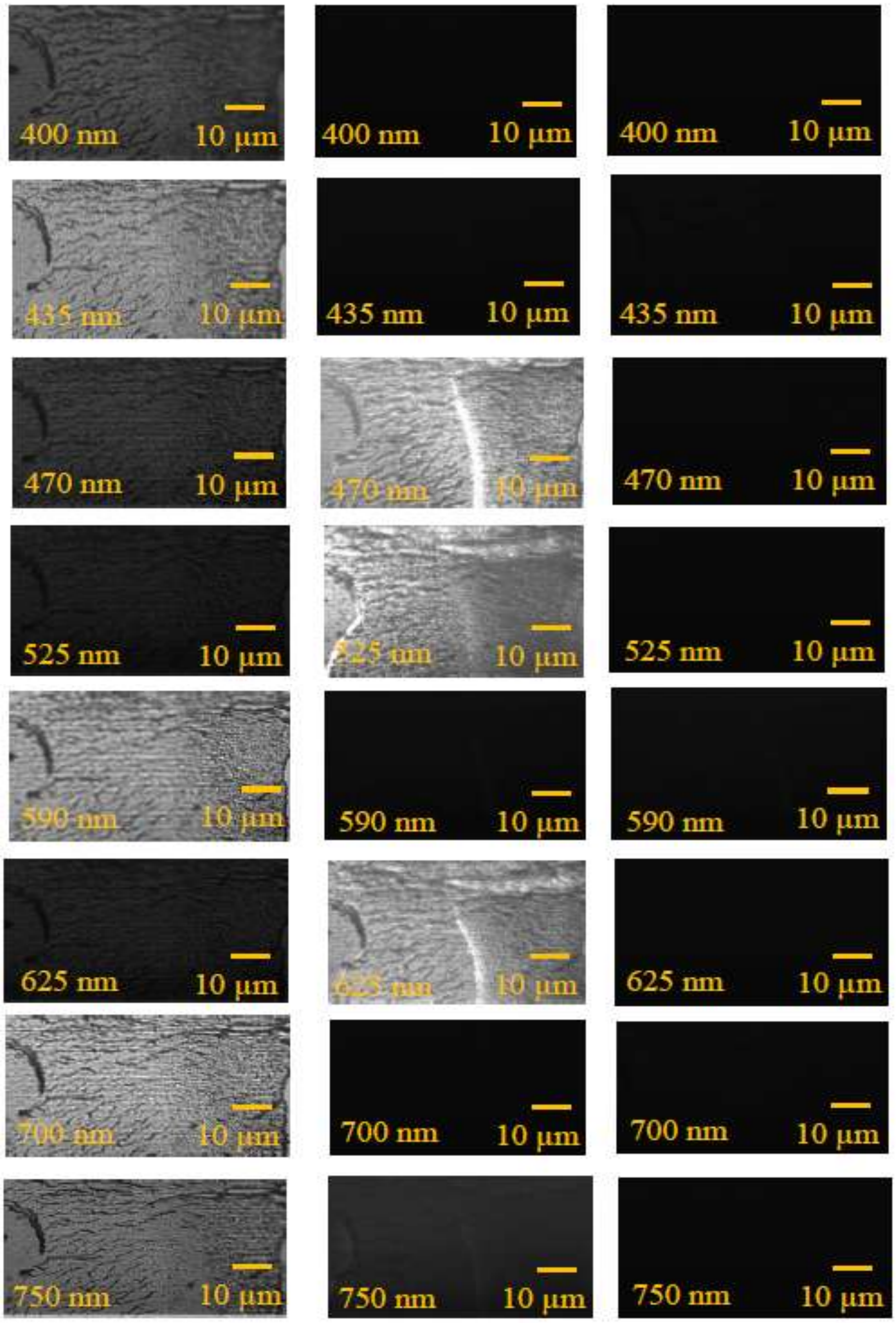

Figure 25: Grayscale Images of Group BD1 USLT Captured in Transmission Mode (First Column), Reflection Mode (Second Column) and Scattering Mode (Third Column) using the MSLEDIM System at 400 nm, 435 nm, 470 nm, 525 nm, 590 nm, 625 nm, 700 nm, and 750 nm Spectral Band.

As in the case of images of SSLT, the discrimination between the two groups, in transmission, reflection and scattering modes, was not easily assessed by observation of the grayscale images of the USLT. Averaged pixel intensities of the images for all the USLT captured at the 13 spectral bands in transmission, reflection and scattering modes were then extracted.

The average pixel intensity values from Group A1 and BD1 SSLT images in the transmission mode are shown in Figure 26. The average pixel intensity values from USLT of Group A1 depicts higher values compared to that of Group BD1. This is attributed to the transparent nature of the USLT of Group A1 which depends on the avascularity, paucity of organelles, narrow inter –fibre spaces and regular organization of it cells and protein (Bassnett & Vrensen, 2011). Within the fibre cells, the crystallins exist with a short-range order less than the wavelength of light, similar to that of glass. The small size of the protein molecules which is less than 10 nm in diameter, and their close packing at high concentration contributes to the transparent nature of the USLT of Group A1 (Michael & Bron, 2011).

It can also be observed that the average pixel intensities from 4 spectral bands in the transmission mode, 435 nm, 590 nm, 700 nm, and 810 nm are higher (> 100 a.u) in both the Group A1 and BD1 USLT compared to the other spectral bands which includes 375 nm, 400 nm, 470 nm, 525 nm, 625 nm, 660 nm, 750 nm, 850 nm and 940 nm. This observation is similar to what was observed in the case of SSLT. This suggest that the USLT can transmit enough light in all these spectral bands but much higher from 435 nm, 590 nm, 700 nm, and 810 nm. The lower opacification of Group BD1 USLT can be attributed to massive insolubilization of the soluble protein in the lens, which results in light scattering by the USLT (David et al., 1987; Cenedella & Fleshner, 1992).

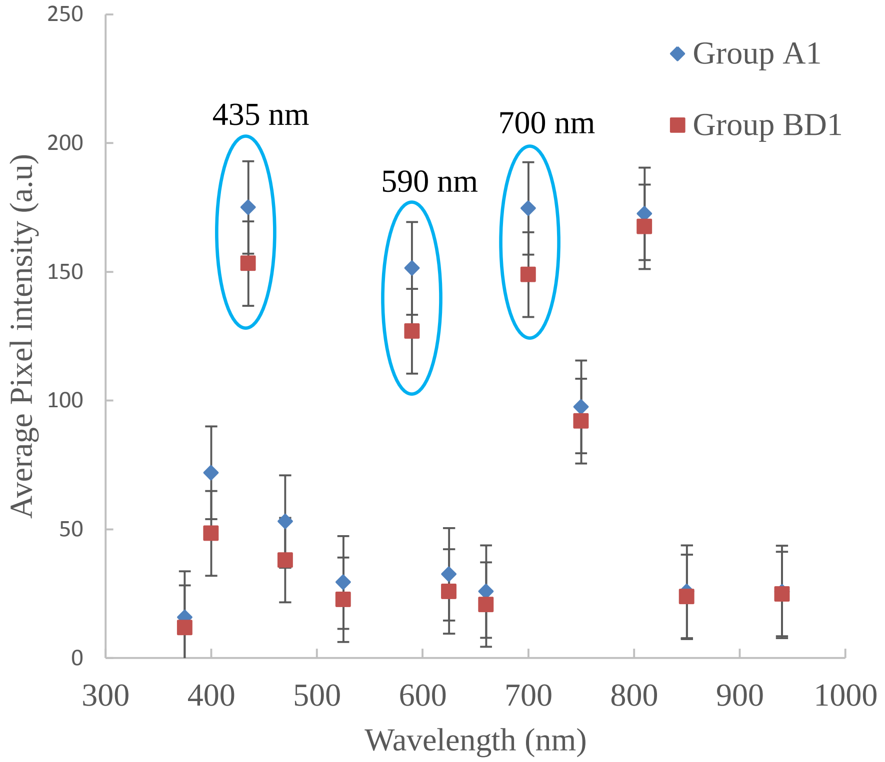

Figure 26: Average Grayscale Pixel Intensities Extracted from USLT Images of Group A1 and BD1 in Transmission Mode.

On the other hand, the USLT of Group BD1 are characterized by increased absorption and scattering of light resulting in decreased in transmission of light to the retina (Kessel et al., 2011). The average transmitted pixel intensities from 435 nm, 590 nm and 700 nm also showed substantial differences between Group A1 and BD1 USLT. Average pixel intensity difference of 10 a.u was used as a criterion. This is an indication that these 3 spectral bands can be used to discriminate USLT of Group BD1 from Group A1 using the averaged pixel intensity values.

The averaged pixel intensity values from USLT images of Group A1 and BD1 in the reflection mode are shown in Figure 27. The Figure shows that the average pixel intensity values from USLT of Group A1 are much higher at 3 specific spectral bands 470 nm, 525 nm and 625 nm than that of Group BD1 as in the case of SSLT. Also, these 3 spectral bands are higher (>150 a.u) in both the Group A1 and BD1 lenses compared to the other spectra bands. This goes to suggest that the lenses do reflects light intensities but much higher from 470 nm, 525 nm and 625 nm as in the case of the SSLT. This can be attributed to the smooth, clear and glassy nature of the Group A1 compared to the rough and wrinkled nature of the Group BD1 USLT as observed in the case of the SSLT.

The average pixel intensities from 470 nm and 625 nm in the reflection mode also show differences between the Group A1 and BD1 USLT. All the other spectral bands could not show significant differences between the Group A1 and BD1 USLT. This is an indication that both 470 nm and 625 nm can be used as markers to discriminate Group A1 from BD1 USLT using averaged pixel intensity values in the reflection mode.

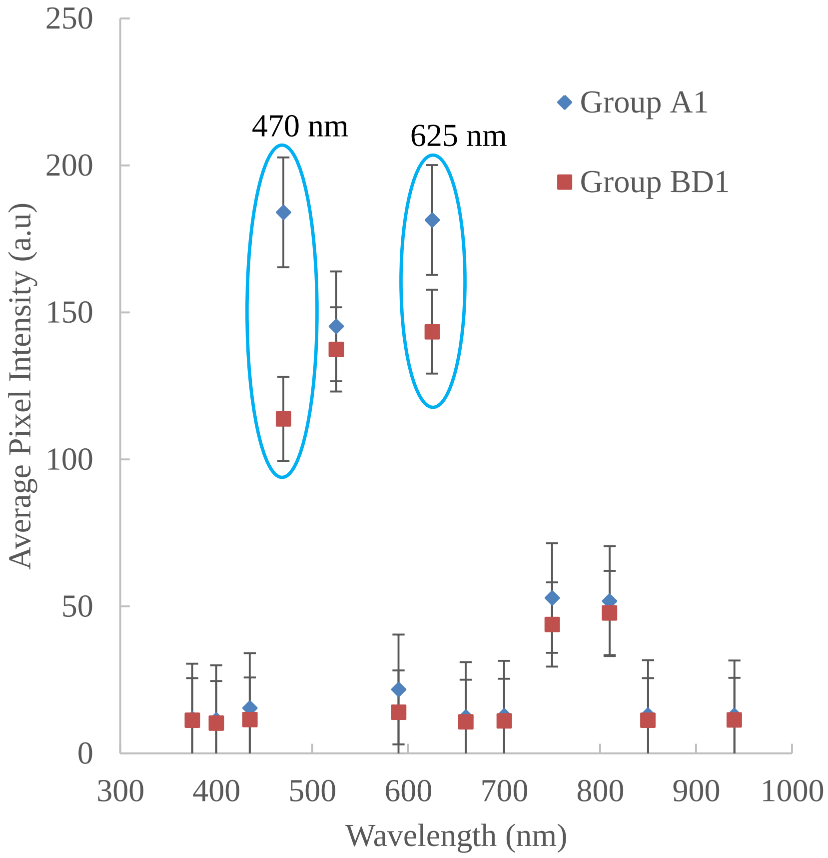

Figure 27: Average Grayscale Pixel Intensities Extracted from USLT Images of Group A1 and BD1 in Reflection Mode.

The averaged pixel intensity values from all the 13 spectral bands in the scattering mode, as shown in Figure 28, were low (< 20 a.u) in both Group A1 and BD1 USLT. The average pixel intensity values ranges from 11 a.u to 17 a.u. These observations may be attributed to the poor scattering properties of the USLT. This shows the USLT of both groups exhibit similar characteristics when it comes to light scattering and are independent of the spectral band. From the intensity values, shown in the insert in Figure 28, the differences between the two groups is insignificant for one to use scattering as a means for discriminating USLT of Group A1 from BD1.

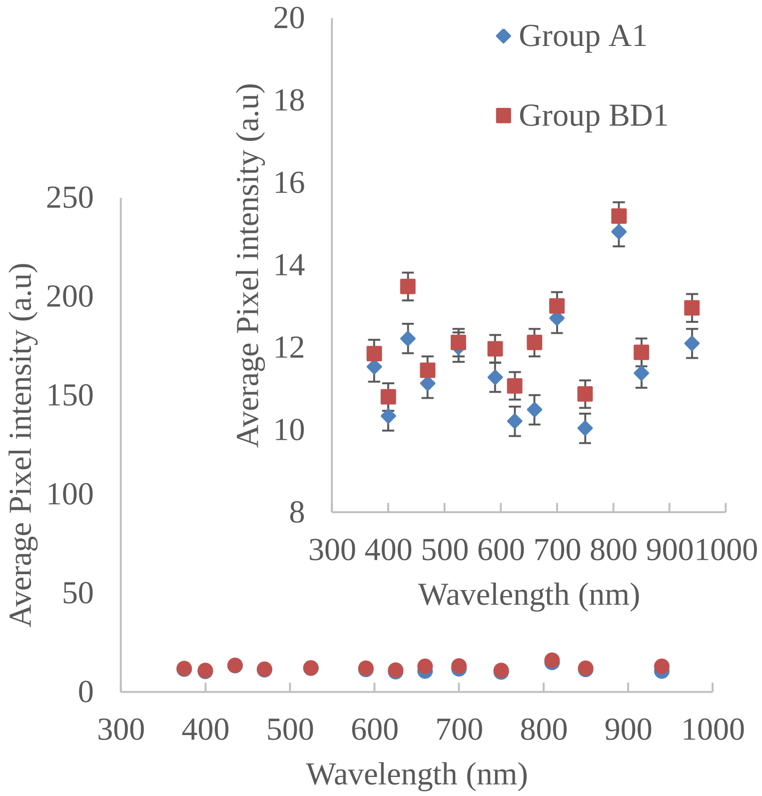

Figure 28: Average Grayscale Pixel Intensities Extracted from USLT Images of Group BD1 and A1 in Scattering Mode.

Similarly as in the case of SSLT, Transmittance (T) and Reflectance (R) by USLT of Group A1 and BD1 were also found to be spectra depended. From theory R + T = 1 since the scattering effect is small as compared to Transmittance and Reflectance from the USLT. It can also establish in this case of USLT that T =1 − (R * ρ) where ρ is a constant**.** The results from both SSLT and USLT showed that the H & E that was used to stain the sectioned lens tissues had no effect on this technique for discriminating Group A1 from Group BD1.

To further the analysis on the average pixel intensity data, principal component analysis (PCA) and Fisher's linear discriminant analysis (FLDA) were performed using developed Matlab codes. This was to discriminate and classify both SSLT and USLT of Group BD1 from A1. In performing the PCA, light intensity extracted from the spectral images captured at 5 spectral bands (435 nm, 590 nm and 700 nm in transmission mode as well as 470 nm and 625 nm in reflection mode) were used. Before the PCA was done, the light intensity data from the 5 spectral bands for all the Group BD1 and A1 were combined and a scree plot (Figure 29) that best explains the PCs to be selected was obtained. The scree plot was obtained with 4999 observations and 5 variables forming 4999 x 5 data points.

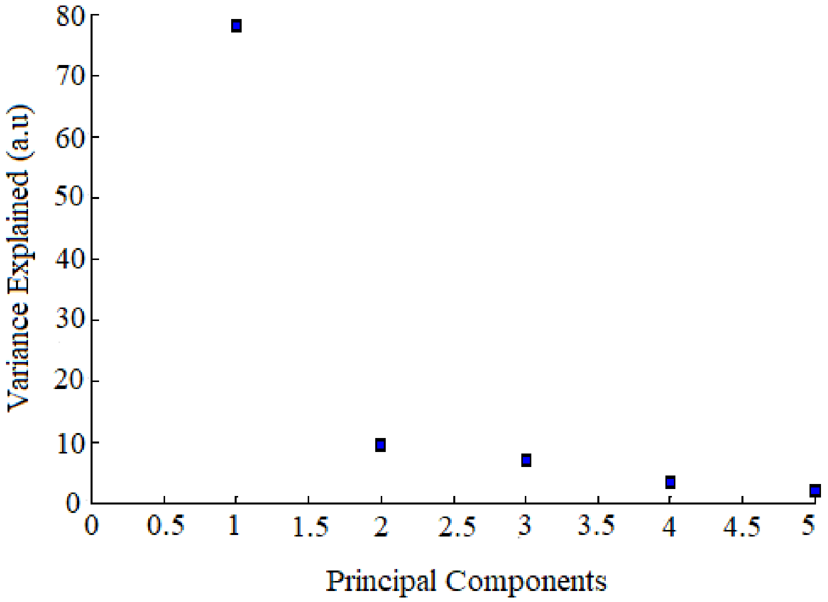

Figure 29: Scree Plot Showing the Eigenvalues of the Five Principal Components (Pcs) Involving the Light Intensity Values from Group A1 and Group BD1 of the Five Spectra Bands.

The PCA plot was used to determine the number of principal components (PCs) appropriate for the discrimination. The PCA reduced the dimensionality of variables, which are the light intensity values at the 5 spectral bands. Martinez and Martinez have suggested that in scree plotting, the point where the points in the curve levels off and becomes almost flat are the ideal PCs (Martinez & Martinez, 2005). The eigenvalues drop off rapidly after the third PC. This suggests that the first three PCs are appropriate for PCA.

Based on the three PCs, the two groups (Group A1 and BD1) were classified using Fisher's linear discriminant function given as

$$P = (\overline{PC}_{GroupA1} - \overline{PC}_{GroupBD1})^{/} S_c^{-/} PC_{xo} \qquad (52)$$

where $\overline{PC}_{\text{GroupA1}}$ and $\overline{PC}_{\text{GroupBD1}}$ are the average values of PC1, PC2 and PC3 from the two groups, $S_c^{-/}$ is the inverse common covariance matrix of the two groups and PC_{xo} is the average PC values of the new light intensity data to be classified.

This new $\text{PC}_{\text{xo,}}$ is allocated to Group A1, if

$$P_0 = (\overline{PC}_{GroupA1} - \overline{PC}_{GroupBD1})^{/} S_c^{-/} PC_{Xo} \geq m \qquad (53)$$

Where *m* is the midpoint between the average PCs of the two group, Group A1 and BD1 and computed from

$$m = \frac{1}{2}(\overline{PC}_{GroupA1} - \overline{PC}_{GroupBD1})^{/} S_c^{-/} (\overline{PC}_{GroupA1} + \overline{PC}_{GroupBD1}) \qquad (54)$$

else PC_{xo} is allocated to Group BD1 if

$$P_0 < m \qquad (55)$$

A structure chart of the Matlab codes developed for processing the light intensities, principal component and Fisher’s linear discriminant analysis is shown in Figure 30.

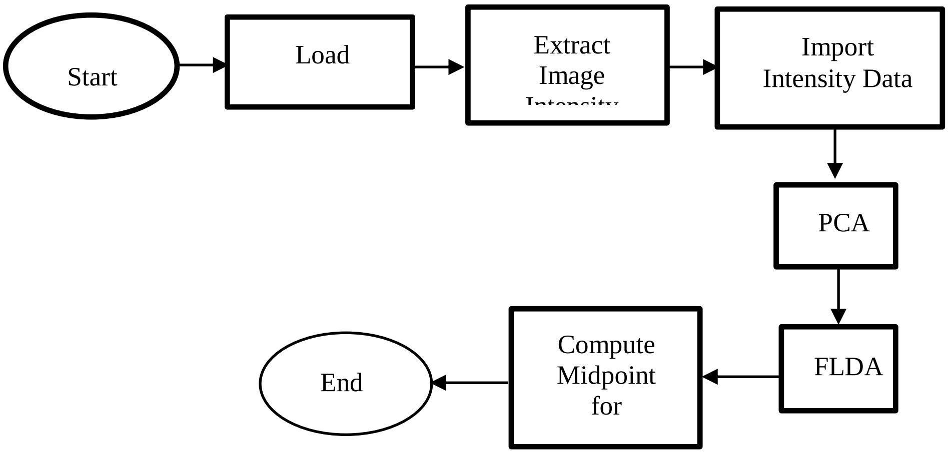

Figure 30: Structure Chat for Processing SSLT and USLT Images of Group A1 and BD1 as well as Performing Principal Component Analysis (PCA) and Fisher’s Linear Discriminant Analysis (FLDA).

Scatter plots of the first three PCs (PC1, PC2 and PC3) of both Group A1 and BD1 SSLT in transmission and reflection mode are shown in Figures 31 and 32 respectively. The three PCs in the transmission mode were obtained from spectral bands of 435 nm 590 nm and 700 nm, with eigenvalues describing 94.53 % of the variability dataset. The first eigenvalue, the one describing the largest amount of variability on the dataset, describes 77.91 % of the overall offset of the transmitted intensity data from the SSLT. The second, 9.54 % of the dataset’s variability was described by the second eigenvalue whiles the third, 7.08 % of the dataset’s variability was describe by the third eigenvalue.

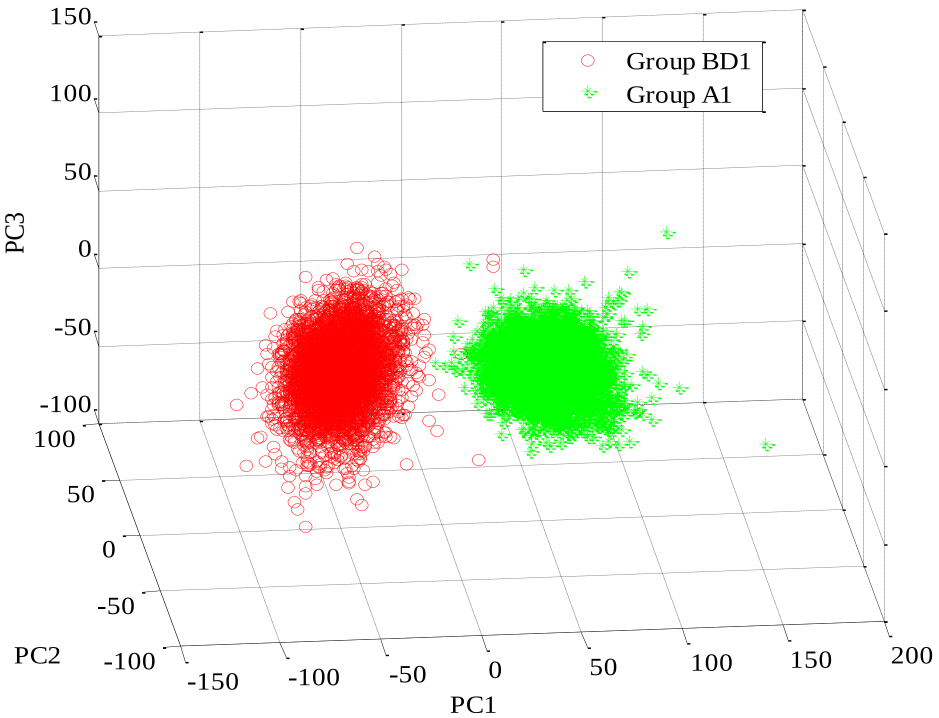

Figure 31: Scatter Plot of the First Three Principal Components of Group A1 and BD1 SSLT for the Three Transmission Spectral Bands (435 nm, 590 nm and 700 nm).

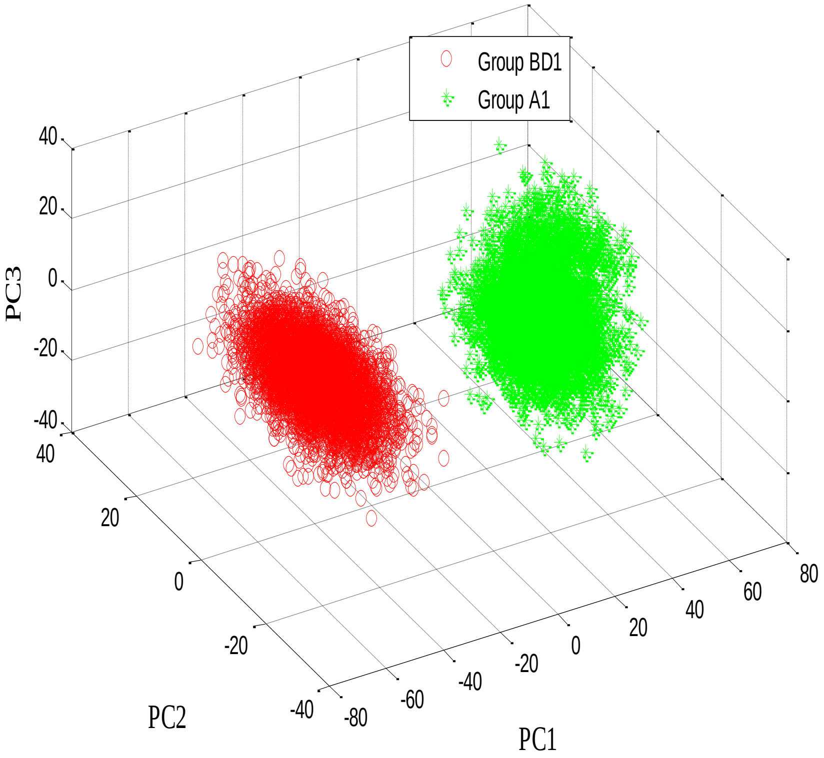

Figure 32: Scatter Plot of the First Three Principal Components of Group A1 and BD1 SSLT for the Two Reflection Spectral Bands (470 nm and 625 nm).

In the case of reflection, the PCs were obtained from 470 nm and 625 nm spectral bands with eigenvalues describing 93 .63 % of the variability of the dataset. As in the previous case, the first eigenvalue represented the overall reflection intensities from the SSLT and described 85. 07 % of the dataset's variability. The second, 5.56 % of the dataset's variability was described by the second eigenvalue whiles the third, 3.00 % of the dataset's variability was describe by the third eigenvalue. The three transmission and two reflection spectral bands showed discrete classification between Group A1 and BD1 SSLT as shown in figures 31 and 32 respectively.

Scatter plot of the first three PCs in the scattering mode could not discriminate between Group A1 and BD1 SSLT. A 3D scatter plot of the first three principal components of Group A1 and BD1 SSLT from combined scattering spectral bands of 660 nm and 940 nm is shown in Figure 33. It is evident that Group A1 SSLT could not be discriminated from the Group BD1 ones upon further analysis. That is, there is no discrete separation pattern between the two groups at the 660 nm and 940 nm scattering spectral band. This is attributed to the low pixel intensity values obtained from both Group A1 and BD1 SSLT.

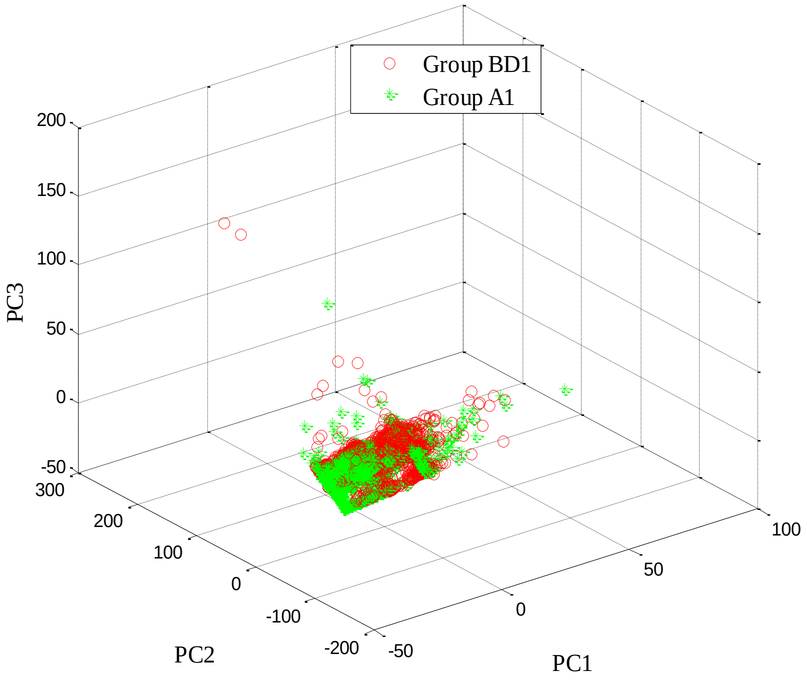

Figure 33: Scatter Plot of the First Three Principal Components of Group A1 and BD1 SSLT for the Two Scattering Spectral Bands (660 nm and 940 nm).

Using trained transmission data from 435 nm, 590 nm and 700 nm, the allocation rule obtained from the Fisher's linear discriminant function with equal cost and equal priors for the SSLT data of the Group A1 and BD1 SSLT and for maximum separation of the two stained sectioned lens tissues is given as

$$P_o = K_1 r_1 + K_2 r_2 + K_3 r_3 \tag{56}$$

with a midpoint m = 3.2374×10^{-14}, where r_1, r_2 and r_3 representing PC1, PC2 and PC3 respectively with K_1, K_2 and K_3 being the co-efficient. In this case K_1, K_2 and K_3 were found to be 0.99, -0.08 and -0.10 respectively. Thus, if $P_o \geq m$, then the SSLT is Group A1, else it is Group BD1. This can be seen in Figure 34 which shows SSLT data in the coordinates of the first two Fisher's discriminants in the transmission mode. The green and red data represents the Group A1 and BD1 SSLT respectively. The plus sign in the middle is the classification midpoint between the Group A1 and BD1 SSLT.

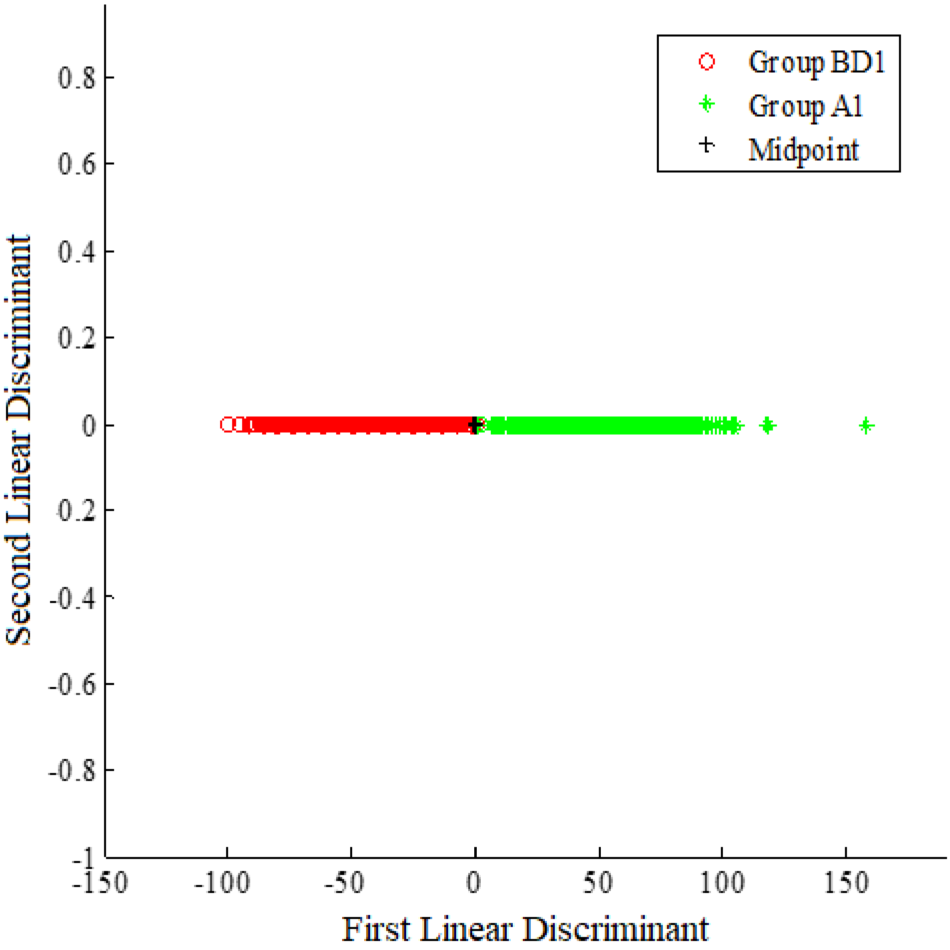

Figure 34: Group A1 and BD1 SSLT Data Plotted in the Coordinates of the First Two Fisher's Discriminants for the Three Transmission Spectral Bands (435 nm 590 nm and 700 nm).

Evaluation of the Fishers' linear discriminant function with 10 transmitted light data showed 90 % success of the discrimination function using the PCs of the Group A1 and BD1 light intensity data. The SSLT data from the reflection mode in the coordinates of the first two Fisher's discriminants is shown in Figure 35**.** The allocation rule obtained using the reflection light intensities from 470 nm and 625 nm and for maximum separation of the two groups of SSLT is given by

$$P_o = L_1 r_1 + L_2 r_2 + L_3 r_3 \tag{57}$$

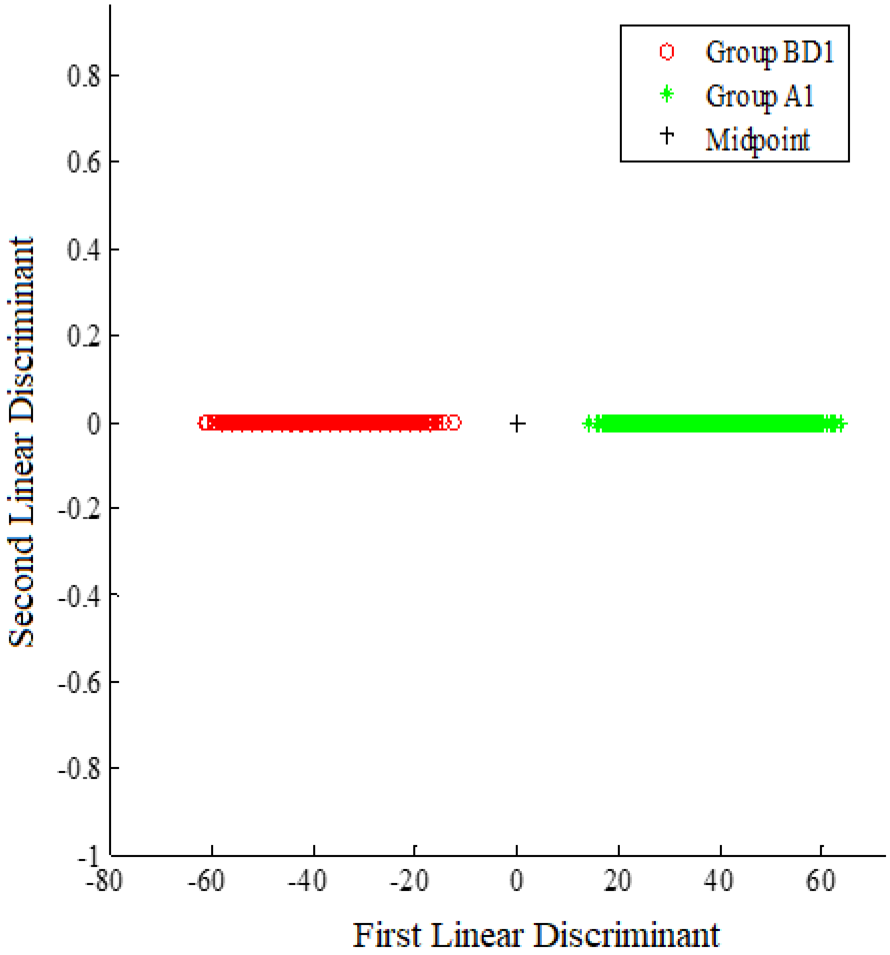

Figure 35: Group A1 and BD1 SSLT Data Plotted in the Coordinates of the First Two Fisher's Discriminants for the Two Reflection Spectral Bands (470 nm and 625 nm).

The values for L_1, L_2 and L_3, which are the coefficients were found to be 0.97, -0.12 and -0.19 respectively. The midpoint values for discriminating Group A1 from BD1 SSLT in both transmission and reflection mode are shown in Table 2. Evaluation of the Fishers' linear discriminant function with 8 reflection data showed 87 % success of the discrimination function using the PCs of the SSLT of Group A1 and BD1 light intensity data.

Table 2. Mid Points Values for Discriminating SSLT of Group A1 from BD1 in Transmission and Reflection Mode.

Mode	Spectral bands (nm)	Midpoint
Reflection	470, 625	14.718×10^{-14}
Transmission	470, 590, 700	3.237×10^{-14}

Similarly, PCA and FLDA were employed in analyzing light intensity data from the Group A1 and BD1 USLT. Figures 36-38 show Scatter plots of the first three PCs (PC1, PC2 and PC3) of Group A1 and BD1 USLT in transmission, reflection and scattering modes. Scatter plots of the first three PCs of USLT of Group A1 and BD1 in transmission and reflection mode are shown in Figures 36 and 37 respectively. The three PCs in the transmission mode were obtained from spectral bands of 435 nm. 590 nm and 700 nm, with eigenvalues describing 94.21 % of the variability dataset. The first eigenvalue, the one describing the largest amount of variability on the dataset, 78.81 %, describes the overall offset of the transmitted intensity data from the USLT. The second, 9.03 % of the dataset’s variability was described by the second eigenvalue whiles the third, 6.37 % of the dataset’s variability was describe by the third eigenvalue. In the case of reflection, the PCs were obtained from 470 nm and 625 nm spectral bands with eigenvalues describing 95 .88 % of the variability of the dataset. As in the previous case, the first eigenvalue represents the overall reflection intensities from the USLT and described 83.81 % of the dataset's variability.

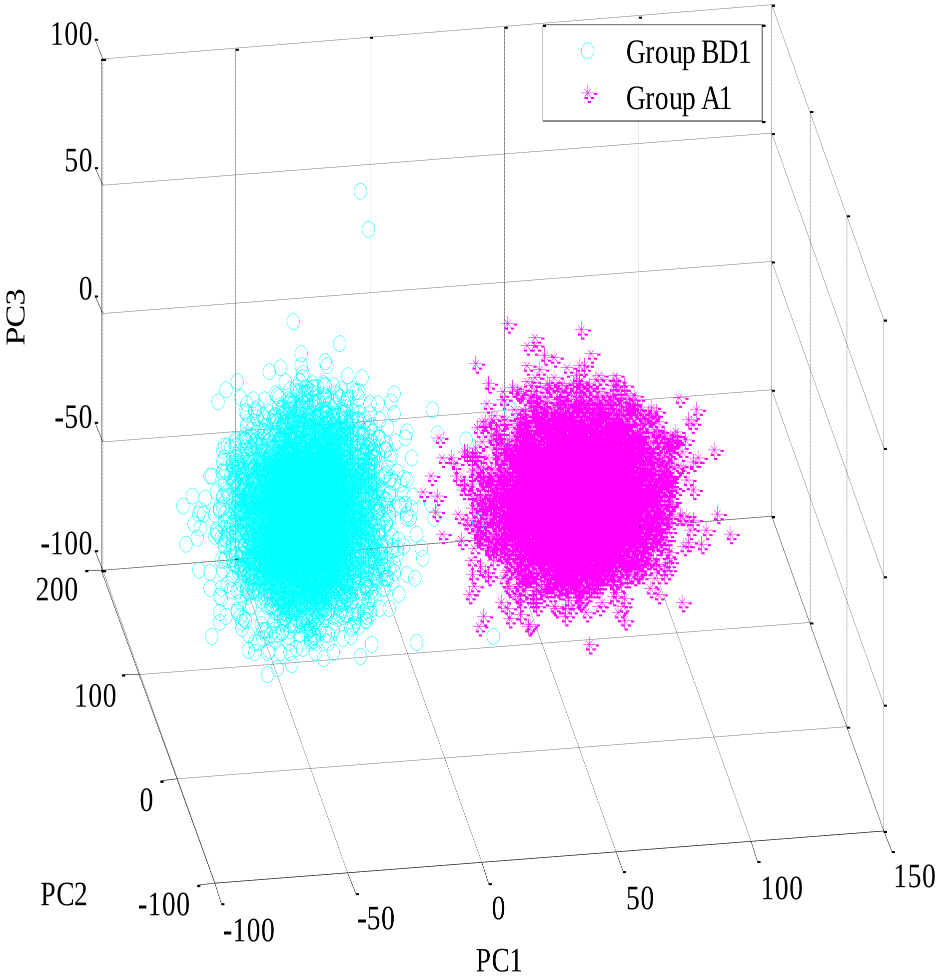

Figure 36: Scatter Plot of the First Three Principal Components of Group A1 and BD1 USLT for the Three Transmission Spectral Bands (435 nm, 590 nm and 700 nm).

The second, 7.22 % of the dataset's variability was described by the second eigenvalue whiles the third, 4.85 % of the dataset's variability was describe by the third eigenvalue.

Transmission and reflection for the three and two spectral bands showed discrete classification between Group A1 and BD1 USLT as shown in figures 36 and 37 respectively.

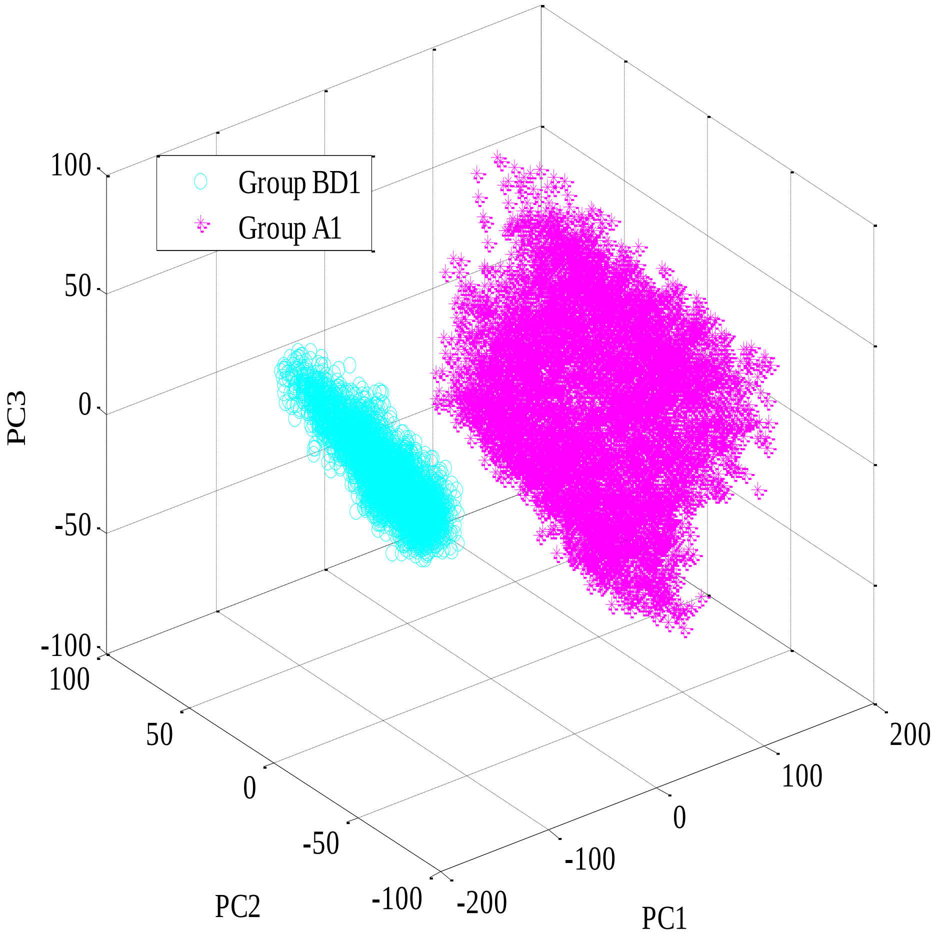

Figure 37: Scatter Plot of the First Three Principal Components of Group A1 and BD1 USLT for the Two Reflection Spectral Bands (470 nm and 625 nm).

Scatter plot of the first three PCs in the scattering mode could not discriminate between unstained Group A1 and BD1 USLT. This is attributed to the similar pixel intensity values obtained from both Group A1 and BD1 USLT. A 3D scatter plot of the first three principal components of Group A1 and

BD1 USLT from combined scattering spectra band of 660 nm and 940 nm is shown in Figure 38. It is evident that Group A1 could not be discriminated from the Group BD1 USLT upon further analysis. That is there is no discrete separation pattern between the two groups at the 660 nm and 940 nm scattering spectral bands. This is attributed to the low pixel intensity values obtained from both Group A1 and BD1 USLT as observed in the case of SSLT.

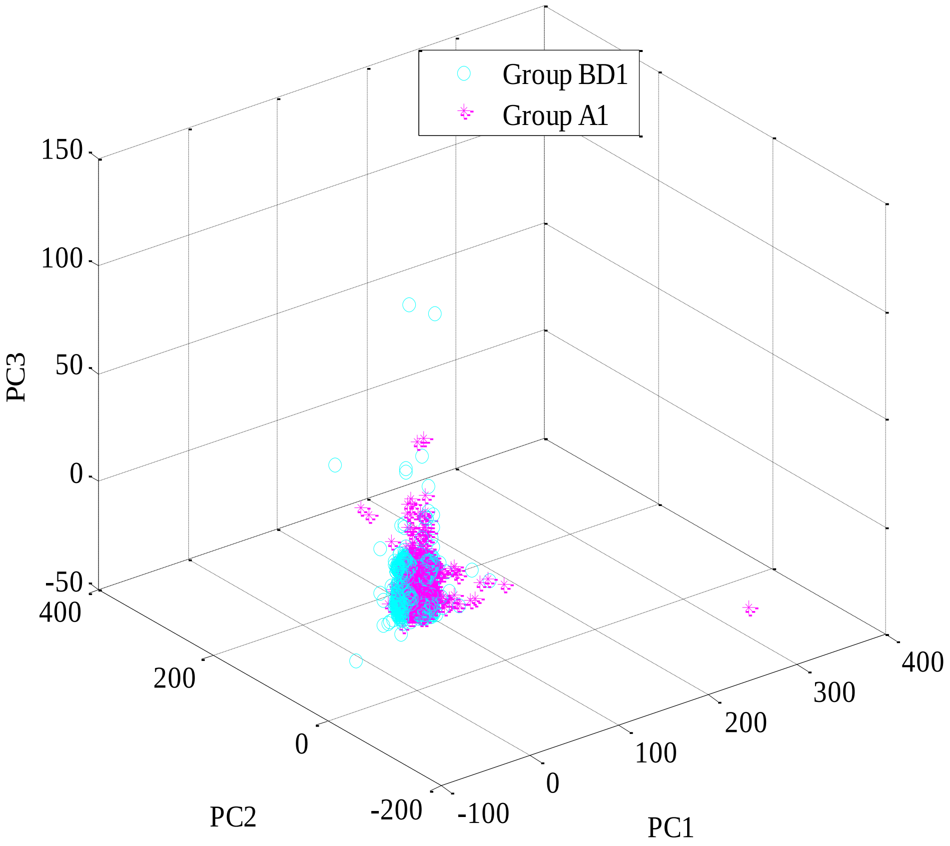

Figure 38: Scatter Plot of the First Three Principal Components of Group A1 and BD1 USLT for the Two Scattering Spectral Bands (660 nm and 940 nm).

The allocation rule obtained from the Fisher's linear discriminant function with equal cost and equal priors for the sample data of Group A1 and BD1 USLT using trained transmission data from 435 nm, 590 nm and 700 nm given as

$$P_o = U_1 r_1 + U_2 r_2 + U_3 r_3 \tag{58}$$

with a midpoint m = 0.5526, where r_1, r_2 and r_3 representing PC1, PC2 and PC3 respectively with U_1, U_2 and U_3 being the co-efficient. In this case U_1, U_2 and U_3 were found to be 0.99, -0.08 and -0.02 respectively. Thus, if $P_o \geq m$, then the USLT is Group A1, else it is Group BD1. This can be seen in Figure 39 which shows USLT data in the coordinates of the first two Fisher's discriminants in the transmission mode. The magenta and cyan data represents the Group A1 and BD1 USLT respectively. The plus sign in the middle is the classification midpoint between the Group A1 and BD1 USLT. Evaluation of the Fishers' linear discriminant function with 9 transmitted data showed 88.8 % success of the discrimination function using the PCs of the USLT of Group A1 and BD1 light intensity data.

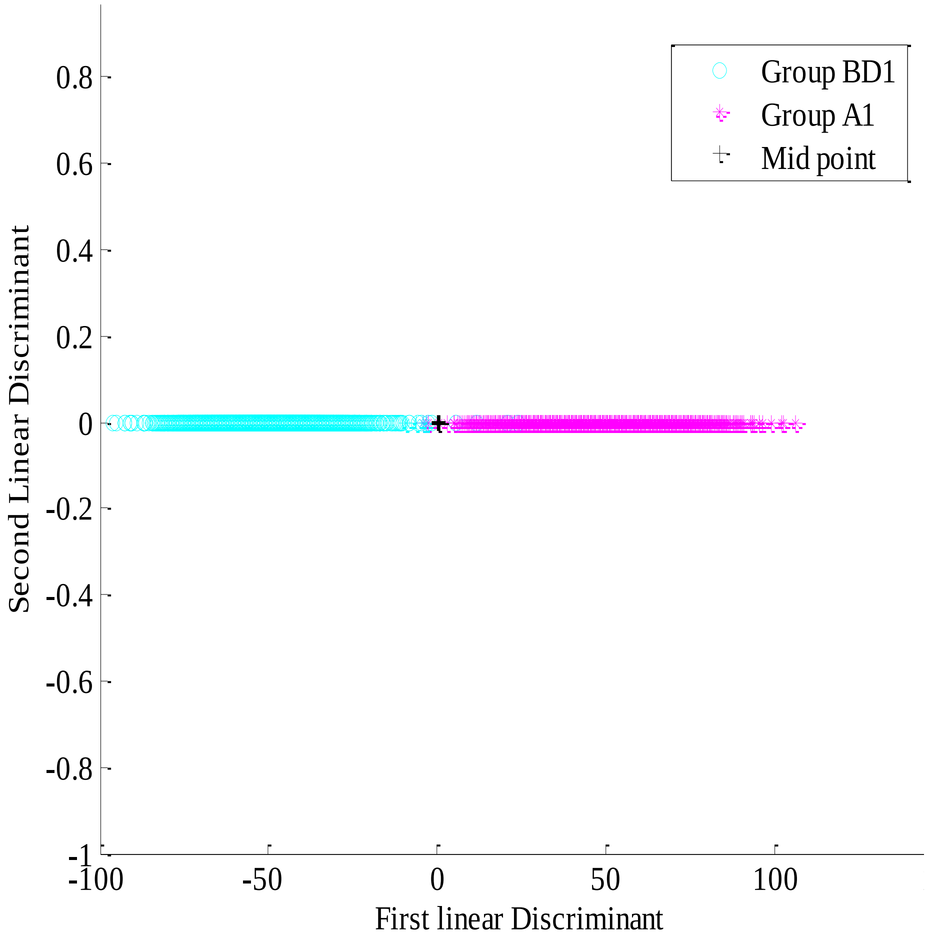

Figure 39: Group A1 and BD1 USLT Data Plotted in the Coordinates of the First Two Fisher's Discriminants for the Three Transmission Spectral Bands (435 nm 590 nm and 700 nm).

The USLT data from the reflection mode in the coordinates of the first two Fisher's discriminants is shown in Figure 40. The allocation rule obtained using the reflection intensities from 470 nm and 625 nm and for maximum separation of the two lenses is given by

$$P_o = V_1 r_1 + V_2 r_2 + V_3 r_3 \tag{59}$$

The values for V_1, V_2 and V_3, which are the coefficients were found to be 0.98, -0.05 and -0.16 respectively.

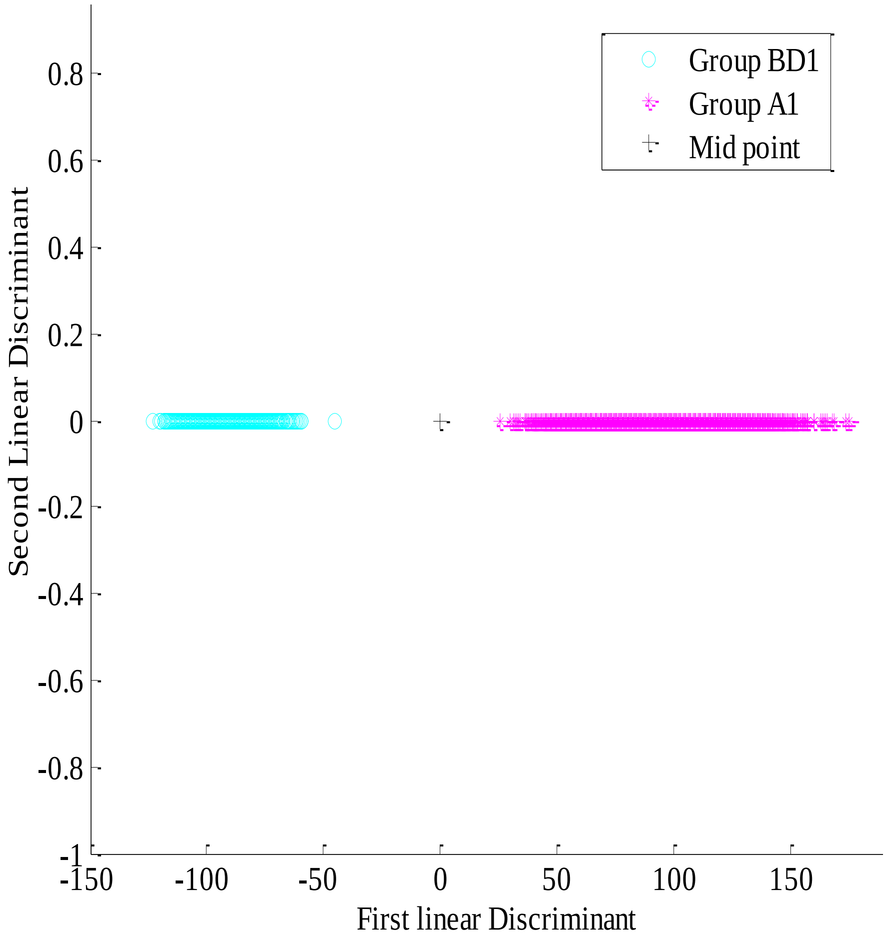

Figure 40: Group A1 and BD1 USLT Data Plotted in the Coordinates of the First Two Fisher's Discriminants for the Two Reflection Spectral Bands (470 nm and 625 nm).

The midpoint values for discriminating unstained Group A1 from BD1 sectioned lens tissues in both transmission and reflection mode are shown in Table 3. Evaluation of the Fishers' linear discriminant function with 7 reflection data showed 85.7% success of the discrimination function using the PCs of USLT of Group A1 and BD1 light intensity data.

Table 3. Mid Points Values for Discriminating USLT of Group A1 from BD1 in Transmission and Reflection Mode.

Mode	Spectral bands (nm)	Midpoint
Reflection	470, 625	-1.675×10^{-13}
Transmission	470, 590, 700	0.5526

Laser-Induced Autofluorescence Spectra Processing of Cataractous Lenses (Group BD2) and the Healthy (Group A2)

The 100 autofluorescence spectra (AFS) data for each of Group A2 and BD2 lens tissues were imported into Matlab platform via developed Matlab codes. Mean spectra of each 100 AFS data of Group A2 and BD2 lens tissues was obtained and then plotted. The mean AFS were then loaded into Origin software (Origin Pro 9.1) for analysis where the peak wavelength of each mean AFS spectra was determined.

In the Matlab platform, PCA as implemented in Adueming *et al* (Adueming et al., 2017) was applied in analysing the AFS data using a developed Matlab codes. The AFS intensity data, Z of $r = 3800$ observations and $q = 2048$ variables was centered, Z_c , such that the elements of the matrix of dimension $r \times q$ are around the sample mean of zero. A scree plot (Figure 41) which gave three PCs (PC1, PC2 and PC3) contributing a total of 99.6% of variability in the autofluorescence intensity data was obtained.

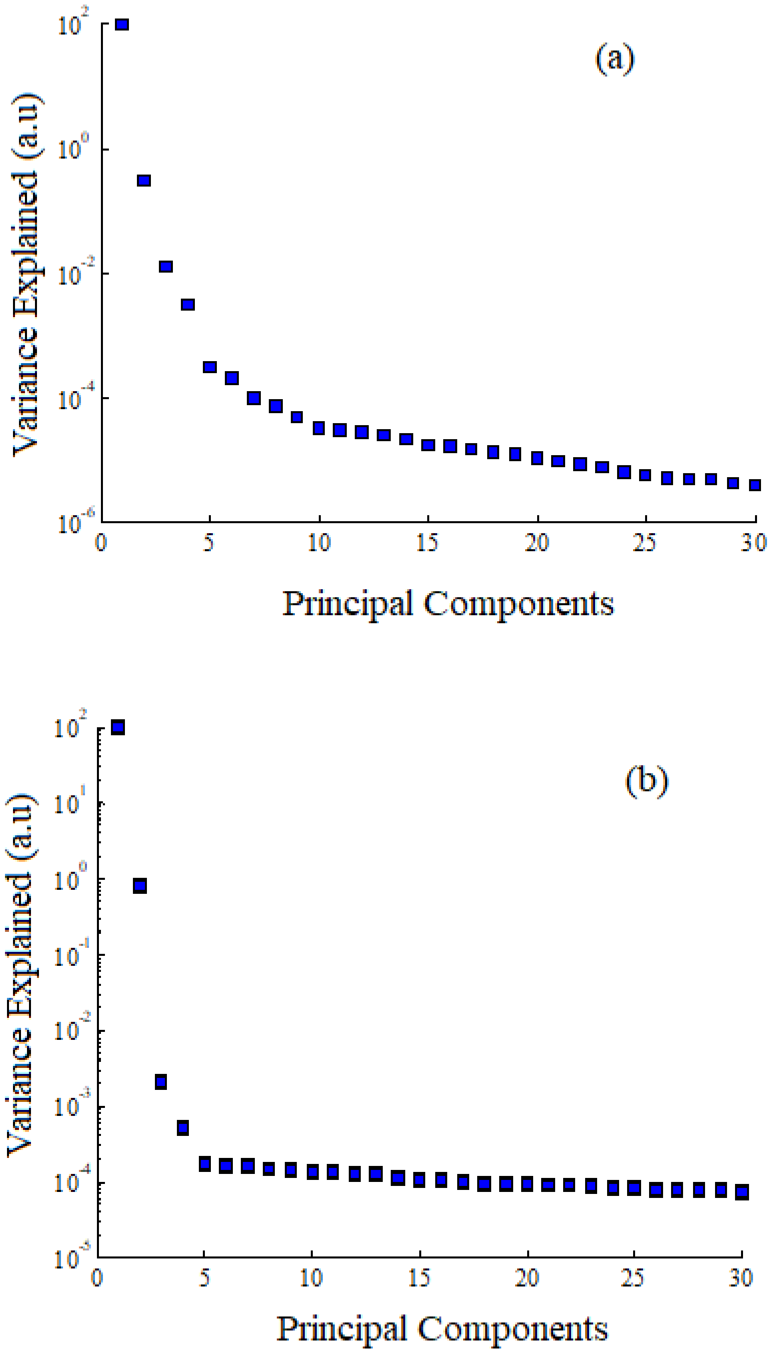

Figure 41: Scree Plot Showing the Eigenvalues of the First 30 Principal Components (Pcs) Out of the 2048 Pcs Contributing to the Total Variance of the AFS for (a) 405 nm (b) 445 nm Wavelength.

Based on the three PCs, the two groups (Group A2 and BD2) were classified using Fisher’s linear discriminant function as in equation 52. Here the

PC_{xo} is the average PC values of the new AFS data to be classified. This new PC_{xo}, is allocated to Group A2, if $P_o \geq m$ according to equation 53 else PC_{xo} is allocated to Group BD2 if $P_o < m$. A structure chart of the Matlab codes developed for processing the AFS and principal component and Fisher's linear discriminant analysis is shown in Figure 42.

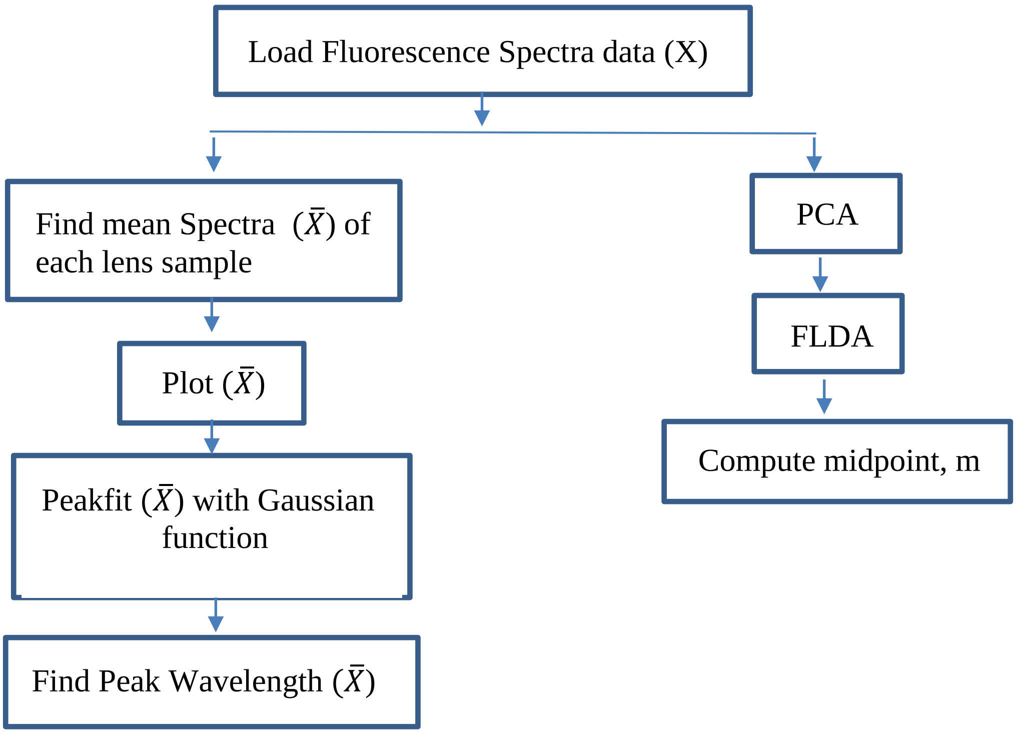

Figure 42: Structure Chat for Processing AFS of Group A2 and BD2 Lens Tissues as well as Performing Multivariate Analysis.

Figures 43(a) and (b) show one of the normalized mean AFS of Group A2 and BD2 lens tissues obtained with 405 nm and 455 nm respectively. Figure 43(a) and (b) reveal changes in the AFS intensity and spectral shape of the lens tissues. The figures show AFS signature of the lens tissues which range from 450-750 nm. It can be observed from Figure 43(a) and (b) that,

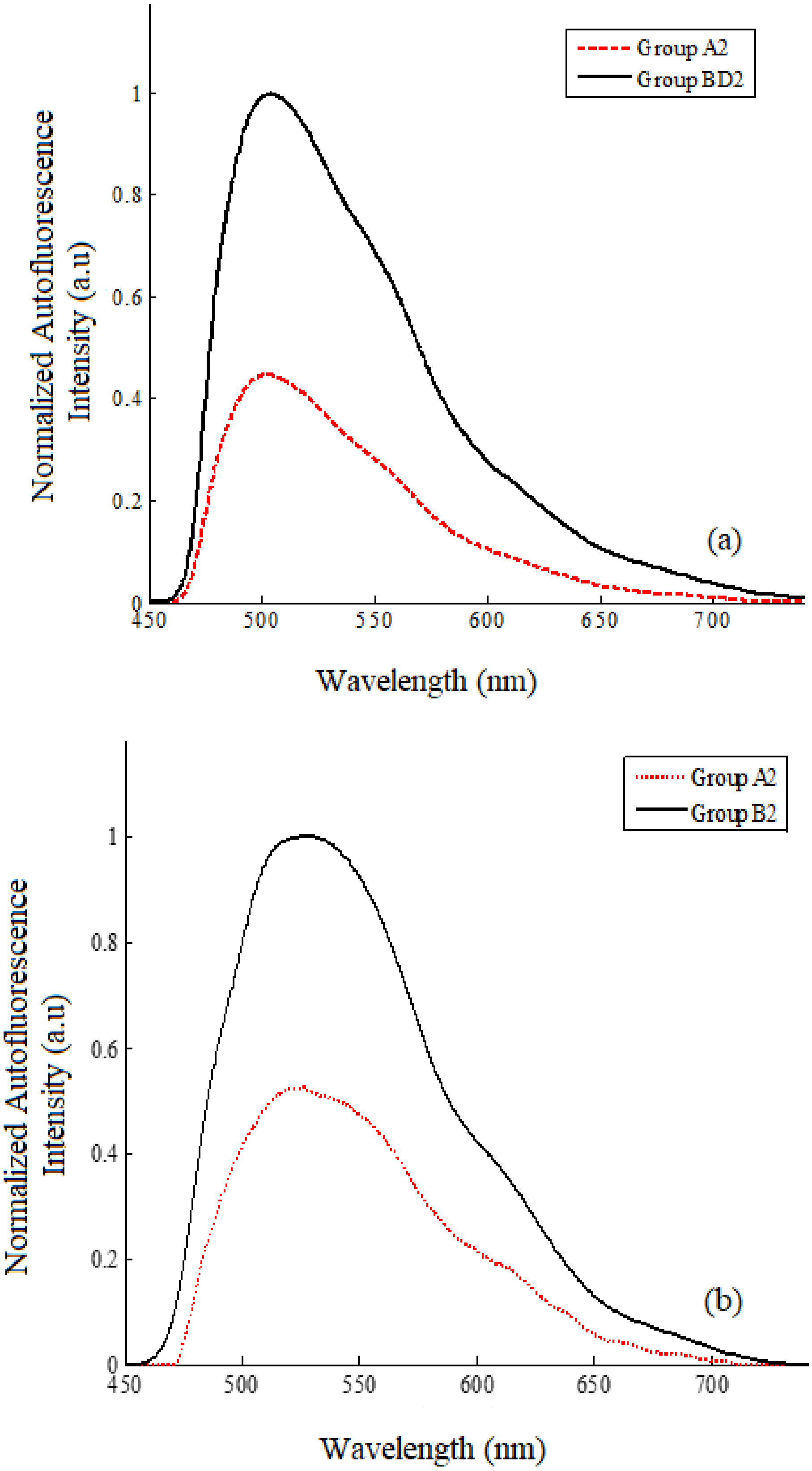

Figure 43**:** Normalized Mean Autofluorescence Spectra of One of the Group A2 and BD2 Lens Tissues at Excitation Light Source of (a) 405 nm and (b) 445 nm.

autofluorescence intensities are high from Group BD2 lens tissues than from the Group A2.

Cataract interferes with retinal imaging by scattering and absorbing light as well as by increasing the lenses autofluorescence (Lerman & Borkman, 1976). The high intensity spectra observed in the Group BD2 lens tissues can be attributed to massive insolubilization of the soluble protein in the lens, resulting in high autofluorescence (David et al., 1987; Cenedella & Fleshner, 1992). In cataract, there is overhydration of the lens due to an imbalance in electrolytes and disruption of the lens fibers. This is followed by an irregular protein distribution in the lens and fluctuation in the refractive index which aids light scattering (Philipson, 1973; Duncan et al., 1997). In the lens, there are increases in selective spectra absorption, in pigmented chromophores and in cross-linked protein aggregates (Philipson, 1973; Weale, 1985).

A slight shift in wavelength of 0.9 nm was observed in the autofluorescence peakfit spectra of Group BD2 and A2 as shown by peak 1 in Figure 44 after their autofluorescence spectra were fitted with Gaussian function using the Origin software. The peak wavelength of the AFS of Group BD2 lens tissues was found to be 505.40 nm and appear to be red shifted from the AFS from the Group A2 whose peak wavelength was found to be 504.50 nm when the samples were excited with a 405 nm light source. The peakfit analysis brought out latent shoulder peaks in the AFS which also showed wavelength shift of 1.8 nm as shown by peak 2 in Figure 44.

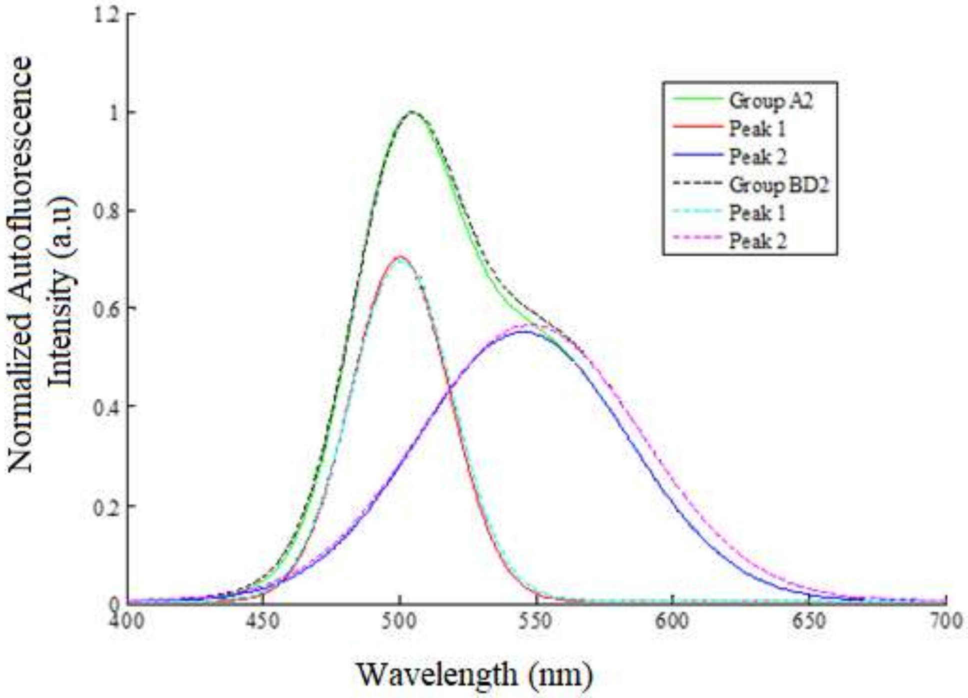

Figure 44**:** Autofluorescence Intensity Distribution of One of the Group BD2 and Group A2 Lens Tissues Fitted with Gaussian Function at 405 nm Excitation Wavelength.

A wavelength shift of 1.2 nm was also observed in the autofluorescence spectra of Group BD2 and A2 as depicted by peak 1 in Figure 45 with 445 nm as an excitation source. Group BD2 lens tissues exhibited autofluorescence peak wavelength at 519.48 nm while Group A2 lens tissues fluoresces at a peak wavelength of 518.60 nm. This red-shifted phenomenon of fluorescence spectra peak wavelengths in Group BD2 lens samples could be due to changes in characteristics of the fluorophores found in Group BD2. Both Group A2 and BD2 lens tissues showed similar AFS with differences in the intensities of their autofluorescence as well as shifts in the peak positions. The peakfit analysis brought out latent shoulder peaks in the AFS which also showed wavelength shift of 2.1 nm as shown in peak 2 in Figure 45.

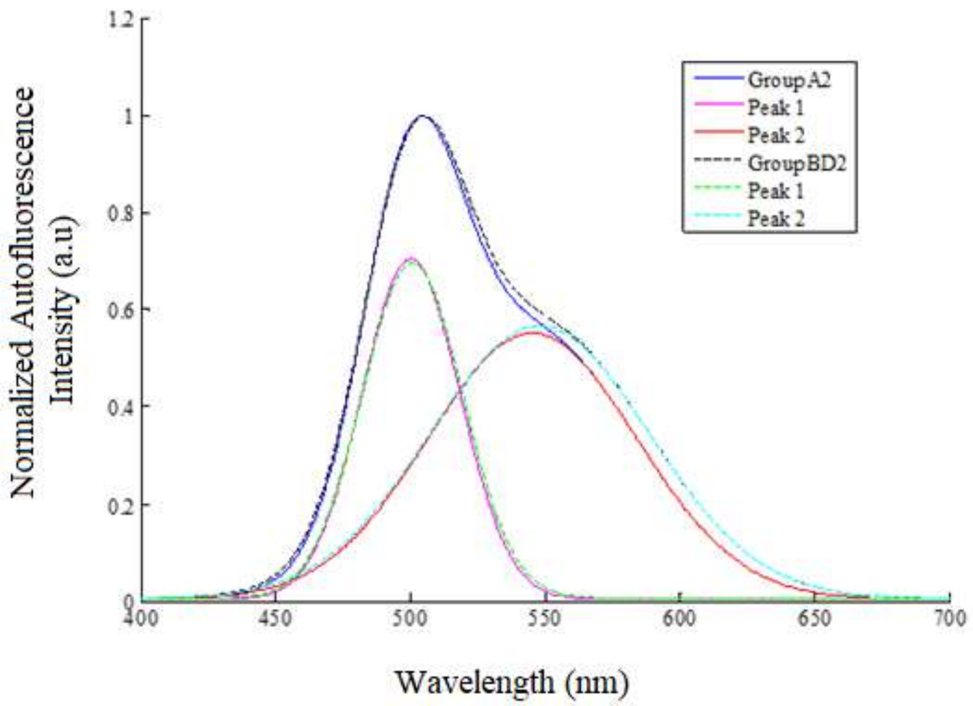

Figure 45**:** Autofluorescence Intensity Distribution of One of the Group BD2 and Group A2 Lens Tissues Fitted with Gaussian Function at 445 nm Excitation Wavelength.

To further ascertain the differences in the peak wavelength of the AFS of Group A2 and BD2 lens tissues, independent *t*-test was used to determine whether the peak wavelengths of Group BD2 lens tissues vary from that of Group A2 with significant level of *p*- value .0001. Tables 4 and 5 show that the autofluorescence peak position of both Group A2 and BD2 lens tissues obtained from 405 nm and 455 nm are statistically different as identified in the fingerprint region. The mean peak wavelengths and their respective standard deviation are presented in the second and third columns respectively, and the last column shows the p values, thus indicating the differences between the peak wavelength positions.

Table 4: Peak Wavelengths, Statistical Comparison between Group A2 and BD2 and *P*- Values Obtained from 405 nm Excitation Wavelength.

Peak	Group A2	Group BD2	*P*-value
1	504.5 ± 0.26	505.4 ± 0.30	.0001
2	558.8 ± 0.57	560.6 ± 1.06	.0001

Table 5: Peak Wavelengths, Statistical Comparison between Group A2 and BD2 and *P*- Values Obtained from 445 nm Excitation Wavelength.

Peak	Group A2	Group BD2	*P*-value
1	518.7 ± 0.15	519.9 ± 0.03	.0001
2	571.5 ± 0.38	573.6 ± 0.34	.0001

Scatter plots of the first three (3) PCs (PC1, PC2 and PC3) of both Group A2 and BD2 AFS obtained with 445 nm and 405 nm light sources are shown in Figures 46 and 47 respectively. Three (3) PCs were obtained from AFS data with 405 nm laser source with eigenvalues describing 99.98 % of the variability dataset. The first eigenvalue, the one describing the largest amount of variability on the dataset, 99.67 %, describes the overall offset of the auto-fluorescence intensity data from the lenses. The second, 0.30 % of the dataset's variability, was described by the second eigenvalue whiles the third, 0.01 % of the dataset's variability, was describe by the third eigenvalue. With AFS data obtained with the 445 nm laser source, the eigenvalues of the PCs obtained describes 99.81% of the variability of the dataset.

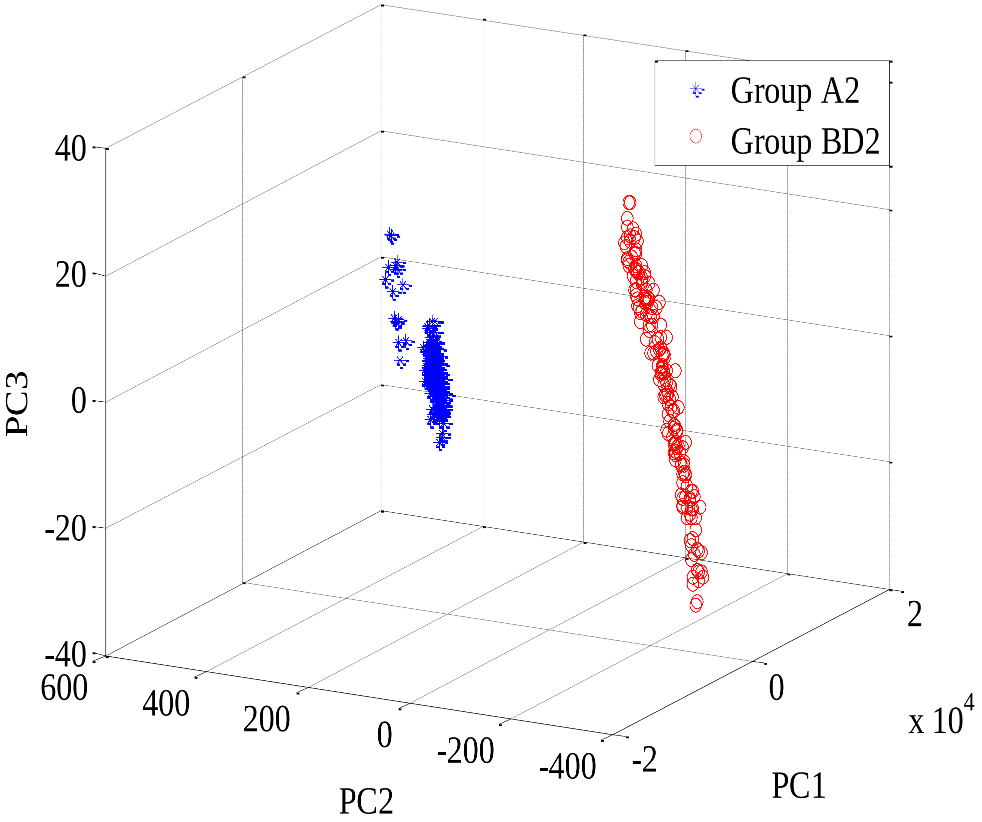

Figure 46: Scatter Plot of the First Three Principal Components of Group A2 and BD2 Lens Tissues for Autofluorescence Spectra Obtained from 445 nm.

As in the previous case, the first eigenvalue represented the overall autofluorescence intensities from the lens tissues and described 99.19 % of the dataset's variability. The second, 0.60 % of the dataset's variability was described by the second eigenvalue whiles the third, 0.02 % of the dataset's variability was described by the third eigenvalue. AFS from 445 nm and 405 nm laser sources showed discrete classification between Group A2 and BD2 lens tissues as shown in Figures 46 and 47 respectively.

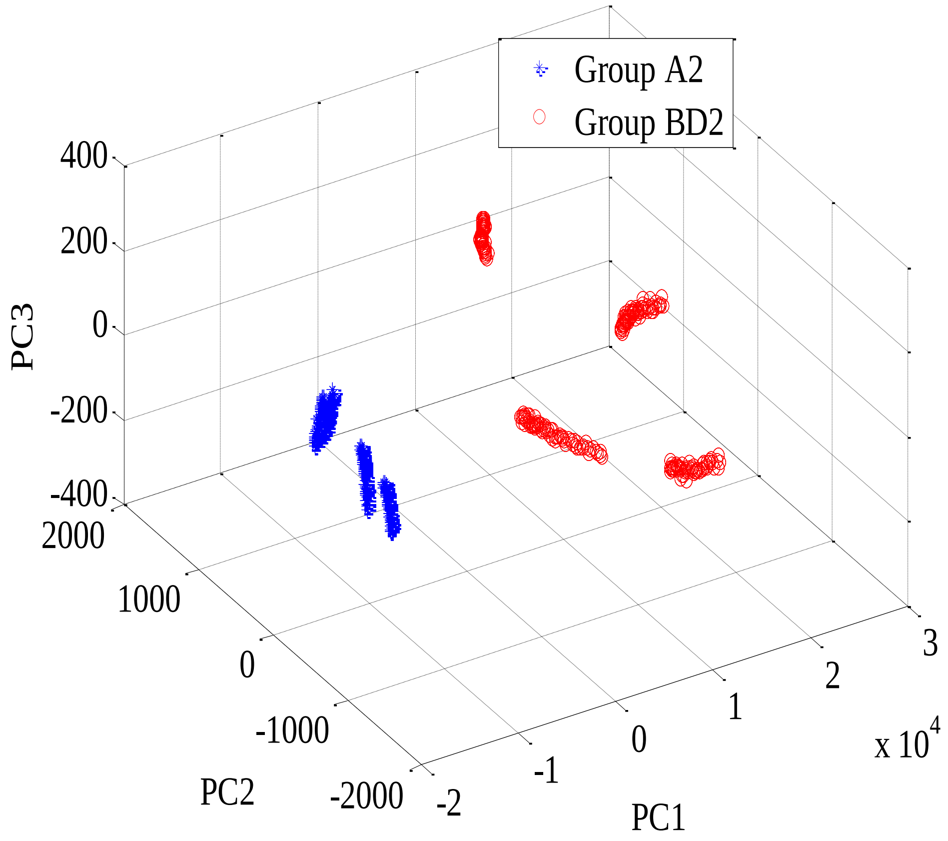

Figure 47: Scatter Plot of the First Three Principal Components of Group A2 and BD2 Lens Tissues for Autofluorescence Spectra Obtained from 405 nm.

Using trained autofluorescence data from 405 nm as excitation source, the allocation rule obtained from the Fisher's linear discriminant function with equal cost and equal priors for the Group A2 and BD2 lens tissues and for maximum separation of the two lens tissues is given as

$$P_o = M_1 r_1 + M_2 r_2 + M_3 r_3 \tag{60}$$

where r_1, r_2 and r_3 represents PC1, PC2 and PC3 respectively with M_1, M_2 and M_3 being the co-efficient. In this case M_1, M_2 and M_3 were found to be 0.0556, -0.0850 and 0.9948 respectively and the midpoint m, was found to be -9.69×10^{-14}. Thus, if $P_o \geq m$, then the lens tissue is Group A2, else it is Group BD2. The autofluorescence lens data from the 405 nm light source is in the coordinates of the first two Fisher's discriminants as shown in Figure 48. The blue and black data represents the Group A2 and BD2 lens tissues respectively. The red circle in the middle is the classification midpoint between the Group A2 and BD2 lens tissues. Evaluation of the Fishers' linear discriminant function with 8 (eight) lens AFS data showed 100 % success of the discrimination function using the PCs of the Group A2 and the BD2 lens tissues.

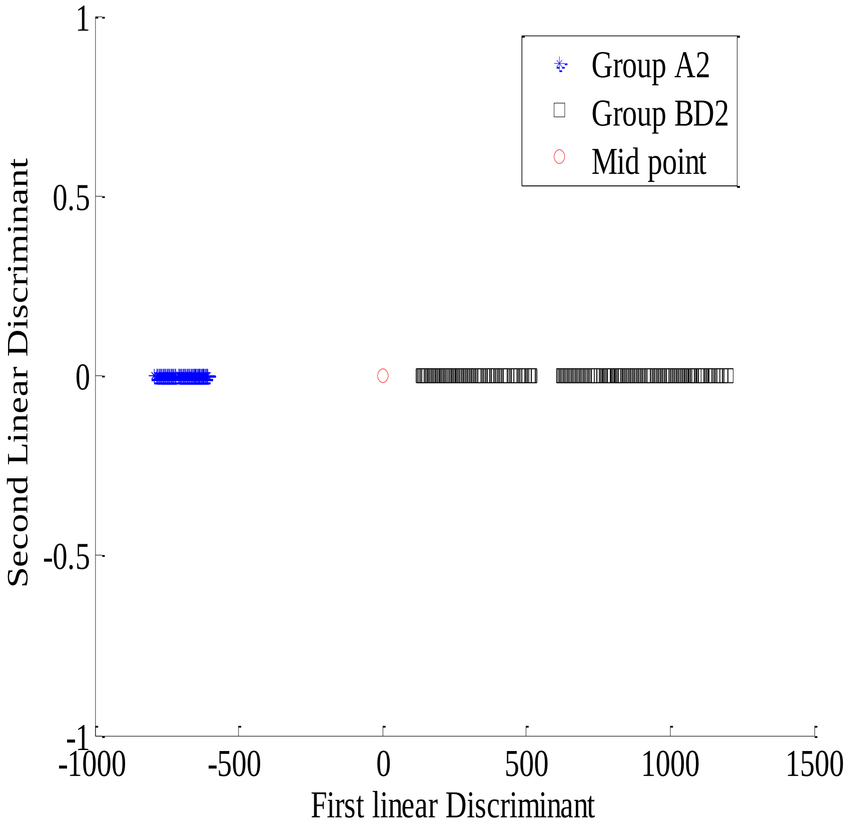

Figure 48: Group A2 and BD2 Lens Tissue Data Plotted in the Coordinates of the First Two Fisher's Linear Discriminants AFS Obtained from 405 nm. The Red Circle Represent the Classification Midpoint.

The AFS data from the 445 nm light source in the coordinates of the first two Fisher's linear discriminants is shown in Figure 49. The allocation rule obtained using the autofluorescence intensities from 445 nm and for maximum separation of the two groups of lens tissues is given by

$$P_o = N_1 r_1 + N_2 r_2 + N_3 r_3 \tag{61}$$

The values for N_1, N_2 and N_3, which are the coefficients were found to be 0.0066, -0.3566 and 0.9342 respectively. The midpoint value was found to be -379.28 x

10^{-14}. Evaluation of the Fishers' linear discriminant function with 10 AFS lens data also showed 100 % success of the discrimination function using the PCs from the Group A2 and BD2 lens tissues.

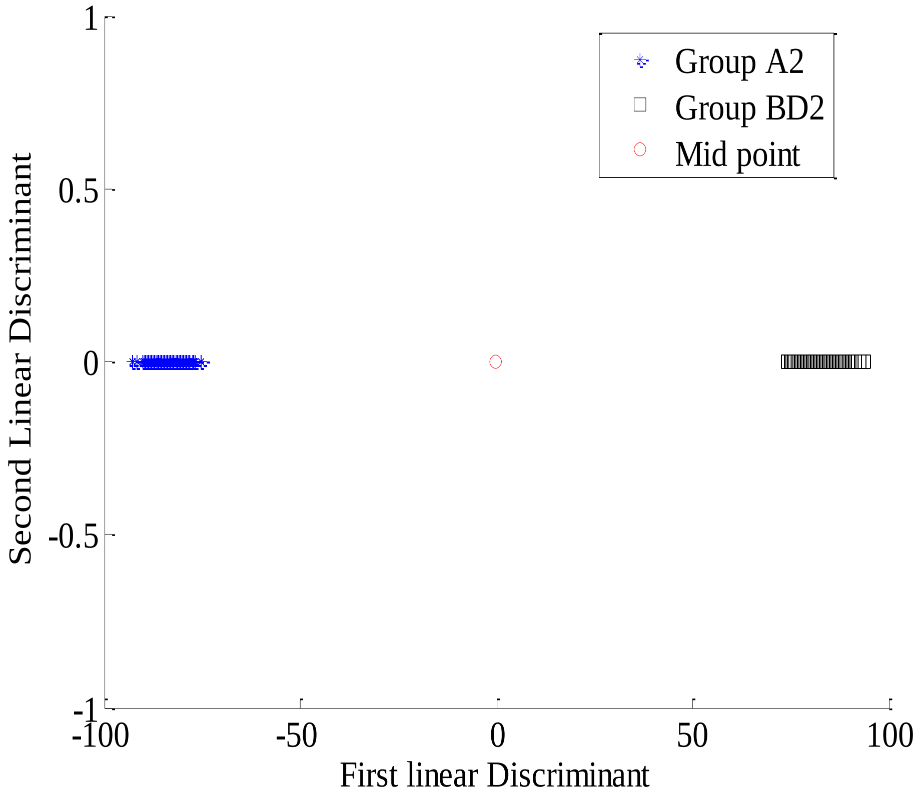

Figure 49**:** Group A2 and BD2 Lens Tissue Data Plotted in the Coordinates of the First Two Fisher's Linear Discriminants AFS Obtained from 455 nm. The Red Circle Represent the Classification Midpoint.

Infrared Spectra of Group A3 and Group BD3 Lens Tissues

The spectra from the fingerprint region (2000 – 600 cm^{-1}), which provides information of vibrational modes associated with important lens tissue content, is shown in Figure 50. Both Group A3 and BD3 lens tissues showed similar vibrational modes, in which some differences in the absorption intensities were observed, as well as shifts in the peak position. Substantial difference is evident in the infrared spectra between the Group BD3 and A3 lens tissues in some specific bands. Band peaking at 1083.14 cm^{-1} is related to symmetric phosphate in healthy lens (Dovbeshko et al, 1997). Increase in absorbance was observed in Group BD3 lens compared to Group A3, as well as a slight shift for 1084.06 cm^{-1} as can be seen in Figure 50.

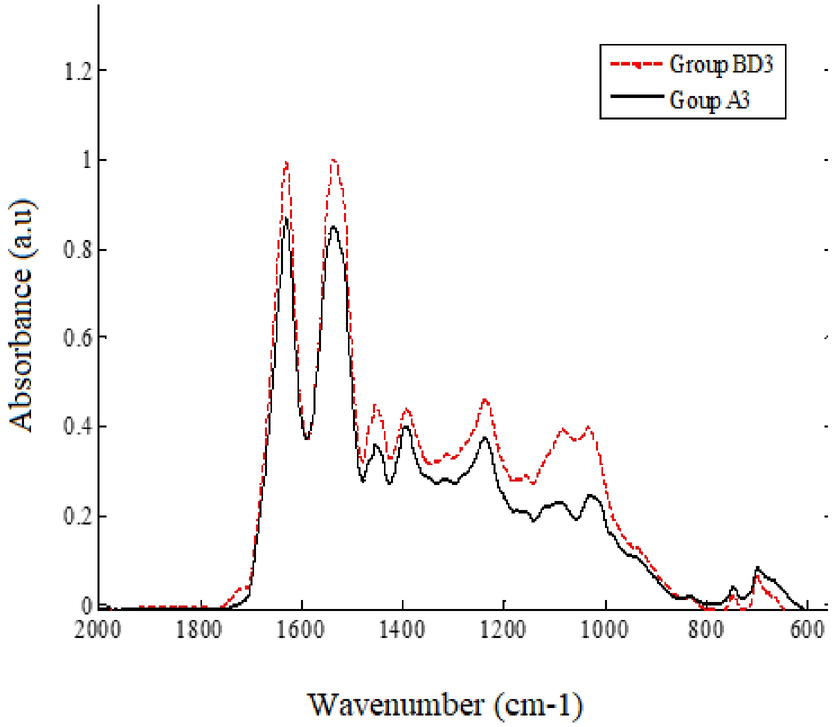

Figure 50. Fingerprint Region (2000–600 cm^{-1}) of Group A3 and BD3 Lenses.

Band position of vibrational modes identified in the fingerprint region are shown in Table 6. The peak position for Group A3 and BD3 lens tissues are presented in the first and second columns whiles the wavelength shift difference is presented in the third column.

Table 6: Identified Wavenumber Values for Group A3 and BD3 Lenses and Wavenumber differences.

Band Peak Position (cm^{-1})

Group A3	Group BD3	Wavenumber shift
1628.86	1628.63	0.23
1536.99	1536.81	0.18
1453.23	1453.70	0.47
1394.04	1392.84	1.20
1313.70	1313.53	0.17
1237.07	1236.73	0.34
1083.14	1084.06	0.92
745.25	746.16	0.91
697.96	698.31	0.35

Spectral band peaking at 1237.07 cm^{-1} is also related to PO_2^- asymmetric (phosphate I) in Group A3 lens tissues (Dovbeshko et al, 1997). It is observed that there was an increase in absorbance in Group BD3 lens compared to Group A3 lens, as well as a slight shift for 1236.73 cm^{-1}. Spectral range from 1500–1700 cm^{-1} (amide I and amide II region) provide information about peptide bonding in proteins and its secondary structure. Changes in the intensities and shifts as observed in the vibrational modes are associated with protein indicating changes in the lens tissue. Band peaking at 1536.99 cm^{-1} and 1628.86 cm^{-1} arise in the Group A3 lens tissue which results from stretching of C=N and C=C (Dovbeshko et al., 1997) whereas a slight shift of 1536.99 cm^{-1} and 1628.86 cm^{-1} was observed for Group BD3 lens tissues respectively. Spectral range from 1307 - 1317 cm^{-1} (amide III) also provides information about the component of proteins in the lens tissues (Movasaghi et al., 2008). These specific band peaks from ATR-FTIR spectra can be used to distinguish Group BD3 lens tissues from Group A3.

To further ascertain the differences between the infrared spectra of Group A3 and BD3 lens tissues, Analysis of Variance (ANOVA) was used to determine whether the means of the absorbed intensities are all equal. Homogeneity of variance was used to determine equal variance between the groups. Homogeneity of variance tests the following hypotheses: H0 = There are no differences between two or more variances and H1 there are differences between two or more variances. With significance level of $p \leq 0.050$, H0 should be rejected and H1 supported. Equal variances was assumed when conducting ANOVA, therefore if homogeneity of variance is violated and the desire is to use the results provided, Table 7 shows spectral band position of vibrational modes of Group A3 and BD3 lens tissues, the mean absorbed intensity at each spectral band and their standard deviation are presented in the third and fourth columns respectively. The last column shows the *P*-values, thus indicating significant differences in the absorbed intensities at seven spectral bands.

Table 7: Identified Wavenumber Values and Statistical Comparison between Group A3 and BD3 Lens Tissues and *P*-values.

ATR-FTIR Bands Position		Band Absorbed Intensity		$p \leq 0.05$
Group A3	Group BD3	Group A3	Group BD3	
1628.86	1628.63	0.187 ± 0.008	0.017 ± 0.007	.029
1536.99	1536.81	0.182 ± 0.007	0.207 ± 0.013	.006
1453.23	1453.70	0.077 ± 0.002	0.095 ± 0.010	.006
1394.04	1392.84	0.085 ± 0.003	0.093 ± 0.003	.006
1313.70	1313.53	0.061 ± 0.001	0.070 ± 0.004	.003
1237.07	1236.73	0.080 ± 0.003	0.098 ± 0.012	.015
1083.14	1084.06	0.051 ± 0.002	0.077 ± 0.011	.001
745.25	746.16	0.007 ± 0.002	0.014 ± 0.028	.630
697.96	698.31	0.017 ± 0.002	0.025 ± 0.035	.613

The table shows significant differences in the absorbed intensities at seven spectra bands (1628.86 cm^{-1}, 1536.99 cm^{-1}, 1453.23 cm^{-1}, 1394.04 cm^{-1}, 1313.70 cm^{-1}, 1237.07 cm^{-1}, and 1083.14 cm^{-1}) since their p values were less than 0.05. The *P*-values of the rest were higher than 0.05 which indicate insignificant differences between the two groups of lens tissues.

Hierarchical cluster analysis (HCA) was also applied on the infrared spectra in order to sort them into two categories. HCA was used as an unsupervised classification technique aiming at sorting the spectra into two categories. HCA was performed to evaluate the potential of the technique to differentiate the spectra of Group A3 and BD3. Results of the clustering are displayed in a tree-like diagram called dendrogram, so that infrared spectra within the same cluster describe spectra with similar characteristics. Results of infrared spectra classification of Group A3 and BD3 lens tissues are shown in Figure 51.

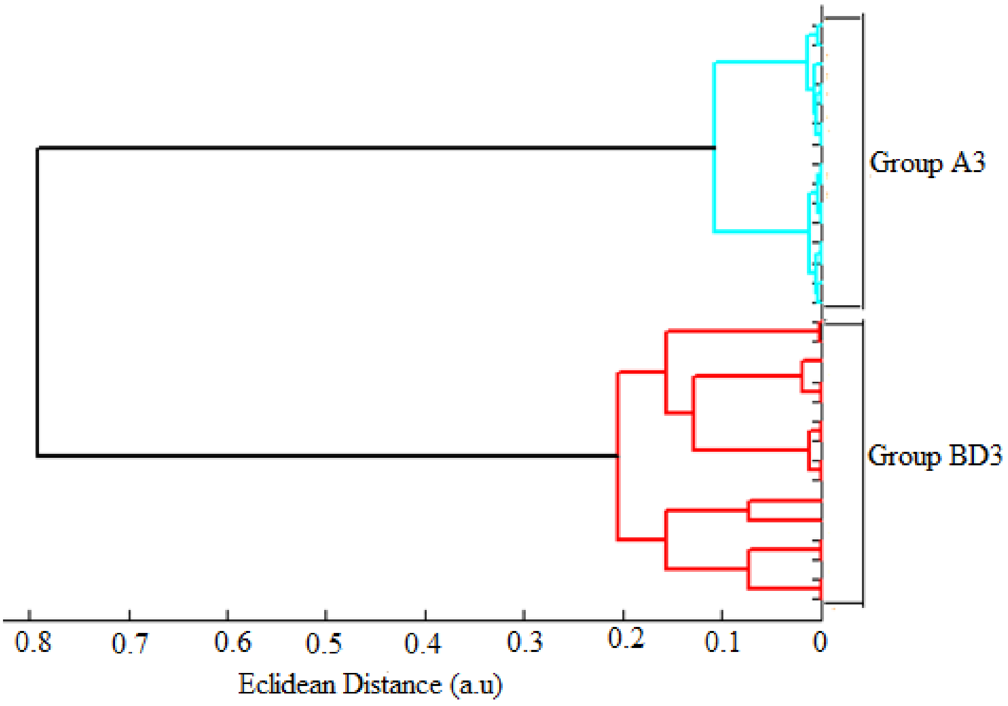

Figure 51: Dendrogram Representing Absorbed Intensity Values of Group A3 (Cyan Colour) and BD3 (Red Colour) Lens Tissues.

The dendrogram shown in Figure 51 classifies all data into two groups. Group A3 correspond to the infrared spectra obtained from the normal lens tissues, whereas Group BD3 represent the spectra obtained for the cataractous lens tissues. The distribution of the infrared spectra data in the groups is shown on the abscissa axis and the distance of spectra within the same cluster is shown on the ordinate axis. From Figure 51, it can be deduced that there are two main clusters resulting from the intensities of both Group A3 and BD3 lens tissues.

Group BD3 lens tissues which is the first main cluster is made up of two sub-clusters. The first sub-cluster of Group BD3 lens tissues consists of six leaf nodes and the second sub-cluster of Group BD3 consists of nine leaf nodes. The second main cluster (Group A3) also has two sub-clusters which are made of eight and seven leaf nodes in first and second sub-cluster respectively. It can also be observed from Figure 51 that the sub-clusters of Group BD3 lens tissues are joined at a higher distance than the sub-clusters of Group A3. These observations may be attributed to increase absorption by Group BD3 compared to the Group A3 lens tissues. The formation of two clusters in the dendrogram indicates absorbed intensities of Group A3 and BD3. Finally, the two clusters were joined together to form a single cluster because they represent absorbed intensities of lens tissues.

Chapter Summary

This chapter has analyzed and discussed the results on the applied experimental optical spectroscopic techniques for discriminating cataractous lens tissues from the healthy lens tissues as well as characterized cataractous lenses of Sprague –Dawley rat. The results of the cataractous lens images acquired with the digital slit lamp microscope SLM – 4ER for the grading of cataractous lenses have been analyzed and discussed in the first part of this chapter. The second part of this chapter analyzed and discussed multispectral imaging results acquired using the multispectral light emitting diode (LED) imaging microscope (MSLEDIM) system. Autofluorescence spectra and infrared spectra of both healthy and cataractous lenses have been analyzed and discussed in the third and final part of this chapter respectively.

CHAPTER FIVE

SUMMARY, CONCLUSIONS AND RECOMMENDATIONS

Overview

The summary and conclusions from the thesis are presented in the first part of this chapter whereas suggested recommendations for future work are presented in the last part of this chapter.

Summary

In summary, the possibility of using optical spectroscopic techniques to characterize and discriminate cataractous lenses from healthy lenses using lens samples obtained from Sprague –Dawley rats has been shown. The research work employed four optical techniques, namely, digital slit lamp microscopy, multispectral light emitting diode (LED) imaging microscope (MSLEDIM), laser-induced autofluorescence (LIAF) and attenuated total reflectance Fourier Transform Infra-Red (ATR-FTIR) spectroscopy.

With the aid of slit lamp images, mean integrated optical density (IOD) of the cataractous lenses were obtained and found to increase with severity. Multispectral imaging technique was used to discriminate stained as well as unstained sectioned cataractous lens from healthy lens tissues. Multispectral images were captured in three modes (transmission, reflection and scattering). In all, five wavelengths in transmission and reflection modes were found to be markers for discriminating healthy lens tissues from cataractous lens tissues. An accuracy of more than 85 % was obtained in classifying the lens tissues using Fisher’s linear discriminant analysis.

Laser-induced autofluorescence (LIAF) was also used to characterize and discriminate cataractous lens from healthy lens tissues with 405 nm and 445 nm as excitation sources. Results show high autofluorescence intensity in cataractous lens tissues than in healthy ones. Cataractous lens tissues show a red shift of 0.9 nm and 1.2 nm at 405 nm and 445 nm excitations, respectively. Using principal component analysis (PCA), three (3) principal components (PCs) gave more than 99 % variability for both 405 nm and 445 nm excitation sources. Based on the 3 PCs, Fisher's linear discriminant model was developed and an accuracy of 100 % was obtained in classifying the lens tissues using Fisher's linear discriminant analysis (FLDA). Attenuated Total Reflectance Fourier transform infrared spectroscopy was finally used to distinguish and discriminate cataractous lens from healthy lens tissues. Infrared spectra from cataractous lens tissues show wavenumber shift in vibrational modes associated with proteins. Hierarchical cluster analysis classified the infrared spectra data as cataractous or healthy.

Conclusions

This work has shown that it is feasible to use optical spectroscopic techniques to study, characterize and discriminate cataractous lenses from healthy lenses using lens samples obtained from Sprague –Dawley rats. Four optical techniques, namely, multispectral light emitting diode (LED) imaging microscope (MSLEDIM), laser-induced autofluorescence (LIAF), attenuated total reflectance Fourier Transform Infra-Red (ATR-FTIR) spectroscopy and digital slit lamp microscopy, were applied in this research work.

Employing the MSLEDI microscope, it has been possible to discriminate stained and unstained sectioned cataractous lens tissues from the healthy ones.

Using extracted average pixel intensities from grayscale multispectral images of stained sectioned lens tissues of healthy lenses (Group A1) and cataractous lenses (Group BD1) from the Spague-Dawley rat, five (5) spectral bands were found to be markers for discriminating stained sectioned lens tissues of Group A from Group B: 470 nm and 625 nm discriminated in reflection mode whereas 435 nm, 590 nm and 700 nm discriminated in transmission mode. MSI technique was used to confirm that Group A1 stained sectioned lens tissues transmit and reflect more light than that of Group BD1. From the scattering intensity values, the differences between the two groups was insignificant for one to use scattering as a means for discriminating stained sectioned lens tissues of Group A1 from Group BD1. Upon further analysis with principal component and Fisher Linear discriminant, three (3) PCs confirmed these five (5) spectral bands as markers for discriminating stained sectioned lens tissues of Group A1 from Group BD1 in the scatter plot. The Fisher's linear discriminant analysis showed 87 % and 90 % success of the discrimination function for the 470 nm and 625 nm spectra bands with reflected light intensities and 435 nm, 590 nm and 700 nm spectral bands with transmitted light intensities respectively. The midpoint for classifying stained sectioned lens tissue of Group A1 from that of Group BD1 for the two reflection spectral bands was found to be 14.718×10^{-14} whereas that from the three transmission spectral bands were found to be 3.2374×10^{-14}. The scattering spectral bands could not discriminate the stained sectioned lens tissues of Group BD1 from Group A1.

Similarly, the same five spectral bands (470 nm and 625 nm in the reflection mode and 435 nm, 590 nm and 700 nm in the transmission mode) were found to be makers for discriminating unstained sectioned lens tissues of Group

A1 from that of Group BD1. The discrimination between unstained sectioned lens tissues of Group A1 and that of Group BD1 was confirmed by 3 PCs in the scatter plot. Fisher's linear discriminant analysis on the light intensities from the two reflection spectral bands and the three transmission spectral bands showed 85.7 % and 88.8 % success of discrimination between the two groups of unstained sectioned lens tissues respectively. The midpoint for classifying unstained sectioned lens tissues of Group A1 from that of Group BD1 for the two reflection markers was found to be -1.675×10^{-13} whereas that from the three transmission markers was found to be 0.5526. The scattering mode could not discriminate between the two groups of unstained sectioned lens tissues as observed in the case of stained sectioned lens tissues.

The five wavelength markers can offer a potential diagnostic tool for discriminating stained or unstained sectioned lens tissues of cataractous lenses of Sprague-Dawley rats from the healthy lenses for ophthalmic applications. MSI technique in combination with multivariate analysis has therefore been used to discriminate sectioned lens tissue of healthy lenses (Group A1) of Sprague-Dawley rats from that of cataractous lenses (Group BD1). The technique has shown that the staining of the tissue with H & E has no effect in discriminating sectioned lens tissues of cataractous lenses from the healthy lenses. MSI has more advantages in terms of rapidity, objectivity and the ability to provide more information on a single sample. It is possible for trained personnel to be able to implement this technique together with the analysis in this field especially in veterinary Ophthalmology.

Laser-induced autofluorescence (LIAF) technique was also applied to detect, discriminate and classify cataractous lens tissues from the healthy lens tissues. The results show high autofluorescence intensity in cataractous lens tissues than the healthy ones with 405 nm and 445 nm as excitation light sources. PeakFit analysis of the autofluorescence spectra (AFS) fitted with Gaussian function showed a peak wavelength shift of 0.9 nm and 1.2 nm from cataractous lens tissues when the lens tissues were excited with the 405 nm and 445 nm respectively. *P*-values obtained from independence T-test showed significant differences in the peak wavelengths. The mean AFS highest peak wavelength for the healthy lens tissues using 445 nm as excitation was found to be 518. 7 nm and that of the cataractous was found to be 519.9 nm. There is approximately 1.2 nm redshift from the healthy lens tissues. The peak wavelength of the AFS of Group A2 lens tissues was found to be 504.5 nm and appear to be red shifted from the AFS of Group BD2 lens tissues whose peak wavelength was found to be 505.4 nm when the lens tissues were excited with a 405 nm light source. Approximately 0.9 nm redshift in wavelength was observed from the healthy lens tissues.

Using principal component analysis, 3 PCs confirmed the discrimination of cataractous lens tissues from the healthy and the Fisher's linear discriminant analysis showed 100 % success of the discrimination function for the LIAF data obtained with the 405 nm and 445 nm laser sources. The midpoint for classifying cataractous lens tissues from the healthy lens tissues with autofluorescence data obtained from 405 nm laser source was found to be

-9.69×10^{-14} whereas that from the 445 nm laser source was found to be

-379.28×10^{-14}. LIAF technique using the two excitation laser sources in the visible region offer an objective discrimination of cataractous lens tissues of Sprague-Dawley rat from that of the healthy lens tissues. The technique can be used to discriminate between the two lens tissues during pre-clinical studies with the help of trained personnel in this field most especially in veterinary ophthalmology.

Infrared spectra from ATR-FTIR measurement was able to objectively distinguish and discriminate cataractous lens tissues from that of the healthy lens tissues. Infrared spectra from cataractous lens tissues showed some wavenumber shifts in vibrational modes associated with proteins from the healthy lens tissues. *P*-values obtained from independence T-test showed significant differences in absorbed intensities at 7 peak wavenumbers. Upon applying Hierarchical cluster analysis, the infrared lens spectra data were classified as cataractous or healthy.

By means of the digital slit lamp microscopy and image processing, an Integrated optical density (IOD) has been used to assess the severity of nuclear cataract. The mean IOD of cataractous lenses were found to increase with severity. The mean IOD values obtained for grade 1 through to grade 4 were found to be 3.9 ± 0.3 a.u, 5.7 ± 0.3 a.u, 8.1 ± 0.4 a.u and 12.2 ± 0.8 a.u respectively. Differences in the values of the mean IOD may offer potential optical indicators for assessing the severity of cataract as it develops from mild through to severe.

Each of the applied optical technique could be potentially used separately or collectively for improved cataract diagnosis. The four optical spectroscopic discrimination of the cataractous lenses from the healthy lenses may together offer new diagnostics methods for the detection of cataract in lenses. This study shows that, cataractous lens samples could be distinguished and discriminated with high precision from the healthy lenses.

Recommendations

There are other types of cataract and it is recommended that the LIAF and MSI techniques be applied on them to characterize and possibly discriminate them from the healthy lenses. The MSI and LIAF could also be applied to discriminate between the other / various types of cataract. These techniques could also be applied to determine the severity of cataract in lenses. It is also recommended that other optical techniques such as polarization microscopy, fluorescence microscopy and confocal microscopy be applied to the cataract lens detection and possibly to determine the level of severity as well. The possibility of insitu measurement with these optical techniques will also be considered in the future for detecting and discriminating cataractous lenses from the healthy lenses of live rats. Employing these techniques to the cataractous lenses would aid in controlling cataract formation and management of cataract patients.

REFERENCES

Abraham, A. G., Condon, N. G. & West Gower, E. (2006). The new epidemiology of cataract. *Ophthalmol Clin North Am.*, *19*, 415-425.

Abraham, A. G., Duncan, D. D., Gange, S. J. & Sheila, W. (2009). Computer-aided assessment of diagnostic images for epidemiological research. *BMC Medical Research Methodology*, *9*(74), 1-8.

Abrardo, A., Alparone, L., Cappellini, V. & Prosperi, A. (1999). Color Constancy from Multispectral Images. *Proc. IEEE Int'l Conf. Image Processing*, *3*, 570-574.

Acharya, R. U., Ng, L. Y., Wong, E. Y. K. & Suri, J. S. (2007). Automatic identification of anterior segment eye abnormality. *IRMB*, *28*(1), 35-41.

Adueming, P. O. -W., Eghan, M. J., Anderson, B., Kyei, S., Opoku-Ansah, J., Amuah, C.L.Y., Sackey, S.S. & Buah - Bassuah, P. K. (2017). Multispectral Imaging in Combination with Multivariate Analysis Discriminates Selenite Induced Cataractous Lenses from Healthy Lenses of Sprague-Dawley Rats. Open Journal of Biophysics, *7*, 145-156. Retrieved from https://doi.org/10.4236/ojbiphy.2017.73011

Anderson, R. & Parrish, J. (1981). The optics of human skin. *Journal of Investigative Dermatology*, *77*(1), 13-19.

Anderson, B., Buah-Bassuah, P. K. & Tetteh, J. P. (2004). Using violet laser-induced chlorophyll fluorescence emission spectra for crop yield assessment of cowpea (*Vigna unguiculata (L) Walp*) varieties. *Meas. Sci.Technol.*, *15*, 255-1265. Retrieved from http://doi.org/10.1088/0957-0233/15/7/005

Andersson-Engels, S., Berg R., Jarlman, O. & Svanberg S. (1990). Time-resolve Transillumination for medical diagnostics. *Optics Letters, 15*, 1179-1181.

Andor Technology. (2006). Absorption, Transmission and Reflectance (ATR) Spectroscopy. Retrieved from www.andor.com.

Alfano, R., Tata, D., Cordero, J., Tomashefsky, P., Longo, F. & Alfano, M. (1984). Laser Induced Fluorescence Spectroscopy from Native Cancerous and Normal Tissue. *IEEE*, *20*, 1507-1511,

Al-Salhi, M., Masilamani, V., Vijmasi, T., Al-Nachawati, H. & Vijaya Raghavan, A. P. (2011). Lung cancer detection by native fluorescence spectra of body fluids-a preliminary study. *Journal of fluorescence, 21*(2), 637-645.

Amuah, C. L. Y., Eghan, M. J., Anderson, B., Osei Wusu Adueming, P & Opoku-Ansah J. (2017). Laser Induced fluorescence in combination with Multivariate analysis classifies anti – malarial herbal plants. *Conference proceedings, OSA publishing, Frontiers in Optics*.

Anidjar, M., Cussenot, O., Blais, J., Bourdon, O., Avrillier, S., Ettori, D., Villette J. M., Fiet, J., Teillac, P, & Le Duc, A. (1996). Argon laser induced autofluorescence may distinguish between normal and tumor human urothelial cell: A microspectrourometric study. *J. Urol., 155*, 1771-1774.

Anil, K, & Anand, A. (2007). *Fundamentals and applications of biophotonics in dentistry*. London Imperial College Press; Hackensack, NJ.

Antunes, A., Gozzo, F. V., Borella, M. I., Nakamura, M., Safatle, A. M. V., Barros, P. S. M. & Toma, H. E. (2007). Atomic Force Imaging of Ocular Tissues: Morphological Study of Healthy and Cataract Lenses. *Modern Research and Educational Topics in Microscopy*, 29-36.

Aparicio, R & Harwood, J. (2013). *Handbook of olive oil* (163-395). New York, USA: Springer.

Atchison, D. A., Collins, M. J., Wildsoet, C. F., Christensen, J. & Waterworth, M. D. (1995). Measurement of monochromatic ocular aberrations of human eyes as a function of accommodation by the howland aberroscope technique. *Vision Res*, *35*(3), 313–323.

Banyay, M., Sarkar, M., & Graslund, A. (2003) A library of IR bands of nucleic acids in solution. *Biophys. Chem.*, *104*, 477-488.

Baranska M. (2014*). Optical Spectroscopy and Computational Methods in Biology and Medicine*. Springer 14.

Barócsi, A., Kocsányi, L., Várkonyi, S., Richter, P., Csintalan, Z. & Szente, K. (2000). Two wavelength, multipurpose, truly portable chlorophyll fluorometer and its application in field monitoring of phytoremediation. Meas. Sci. Technol. *11*, 717-729.

Bassnett, S., Shi, Y. & Vrensen, G. F. J. M. (2011) Biological Glass: Structural Determinants of Eye Lens Transparency. *Philosophical Transactions of the Royal Society B*, *366*, 1250-1264. Retrieved from https://doi.org/10.1098/rstb.2010.0302

Bautista, P.A. & Yagi, Y. (2011). Localization of Eosinophilic Esophagitis from H&E stained images using multispectral imaging. *Diagnostic Pathology*, *6*, 1-8.

Beer, A. (1852). Determination of the absorption of red light in coloured liquids. *Ann. Phys. Chem.*, *162*, 78-88.

Belliveau, J. W., Kennedy, D. N., McKinstry, R. C., Buchbinder, B. R., Weisskoff, R. M., Cohen, M. S., Vevea, J. M., Brady, T. J. & Rosen, B. R. (1991). Functional mapping of the human visual cortex by magnetic resonance imaging. *Science*, *254*(5032), 716-719.

Bengtsson, M., Wallström, S., Sjöholm, S., Grönlund, R., Anderson, B., Larsson A., Karlsson, S., Kroll, S., & Svanberg, S. (2005). Fungus covered insulator materials studied with laser-induced fluorescence and principal component analysis. *Appl. Spec*., *59*, 1037-1041.

Benveniste, H. & Blackband, S. (2002). MR microscopy and high resolution small animal MRI: Applications in neuroscience research. *Prog Neurobiol.*, *67*(5), 393-420.

Berg, R., Jarlman, O. & Svanberg, S. (1993). Medical transillumination imaging using short-pulse diode lasers. *Appl. Opt. 32*, 574-579.

Bersha, K.S. (2010). *Spectral Imaging and Analysis of Human Skin*. Master Thesis Report, Master Erasmus Mundus in Colour in Informatics and Media Technology (CIMET), University of Eastern Finland.

Bigio, I. J. & Mourant, J. R. (1997). Ultraviolet and visible spectroscopies for tissue diagnostics: fluorescence spectroscopy and elastic-scattering spectroscopy. *Phys. Med. Biol.*, *42*, 803–814.

Bloemendal, H., De Jong, W., Jaenicke, R., Lubsen, N. H., Slingsby, C. & Tardieu, A. (2004). Ageing and vision: structure, stability and function of lens crystallins. *Prog. Biophys. Mol. Biol.*, *86*, 407-485. (doi:10.1016/j.pbiomolbio.2003.11.012).

Böhnke, M. & Barry, M. R. (1999). Confocal Microscopy of the Cornea. *Progress in Retinal and Eye Research.*, *18*(5), 553 - 628.

Bohren, C. & Huffman, D. (1983). *Absorption and scattering of light by small particles*. Wiley, New York.

Bouguer, P. (1729). *Essai d'optique sur la gradation de la lumière*. Claude Jombert, Paris, France.

Brandenburg, K. & Seydel, U. (1998) Infrared spectroscopy of glycolipids. *Chem. Phys. Lipids*, *96*, 23-40.

Bremard, C., Girerd, J. J., Kowalewski, P., Merlin, J. C. & Moreau, S. (1993). Spectroscopic investigations of malaria pigment. *Appl. Spectrosc.*, *47*, 1837-1842.

Brown, N. P., Harris, M. L., Shunshin, G. A., Vrensen, G. F. J. M., Willekens, B. & Bron, A. J. (1993). Is Cortical Spoke Cataract due to Lens Fibre Breaks? The Relationship between Fibre Folds, Fibre Breaks, Water Clefts and Spoke Cataracts. *Eye*, *7*, 672-679. Retrieved from https://doi.org/10.1038/eye.1993.154

Brydegaard, M., Guan, Z., & Svanberg, S. (2009). Broad-band multispectral microscope for imaging transmission spectroscopy employing an array of light-emitting diodes. *American Association of Physics Teachers*,*77*, 104-110.

Brydegaard, M., Haj-Hosseini, N., Wårdell, K., & Andersson-Engels, S. (2011). Photobleaching-Insensitive Fluorescence Diagnostics in Skin. *IEEE Photonics Journal*, *3*, 407-412.

Brydegaard, M., Merdasa, A., Jayaweera, H., Ålebring, J. & Svanberg, S. (2011). Versatile multispectral microscope based on light emitting diodes. *Review of Scientific Instruments*, *82*, 1106-1113.

Buxton, R.B. (2002). *Introduction to Functional Magnetic Resonance Imaging: Principles & Techniques*. Cambridge: Cambridge University Press.

Campbell, M. C. (1984). Measurement of refractive index in an intact crystalline lens. *Vision Res*, *24*(5):409-415.

Carter III, W. D. (2007). *Raman spectroscopic study of single red blood cells infected by the malaria parasite plasmodium falciparum*. Doctoral dissertation, University of Central Florida Orlando, Florida. Retrieved from http://etd.fcla.edu/CF/CFE0001780/Carter_William_D_200708_MAST.pdf.

Castro, A., Siedlecki, D., Borja, D., Uhlhorn, S. Parel, J. M., Manns, F. & Marcos, S. (2011). Age-dependent variation of the gradient index profile in human crystalline lenses. *Journal of Modern Optics*, *58*(19-20),1781-1787.

Cenedella, R. J. & Fleshner, C. R. (1992) Selective Association of Crystallins with Lens "Native" Membrane during Dynamic Cataractogenesis. Current Eye Research, *11*, 801- 815. Retrieved from https://doi.org/10.3109/02713689209000753

Chen, Y. C., Galpern, W. R., Brownell, A. L., Matthews, R. T., Bogdanov, M., Isacson, O., Keltner, J. R., Beal, M. F., Rosen, B.R. & Jenkins, B.G. (1997). Detection of dopaminergic neurotransmitter activity using pharmacologic MRI: Correlation with PET, microdialysis, and behavioral data. *Magn Reson Med.*, *38*(3), 389-398.

Chylack, L. T. Jr., Leske, M. C., Sperduto, R., Khu P. & McCarthy, D. (1988). Lens opacities classification system. *Arch Ophthalmol.*, *106*, 330-334.

Chylack, L, T. Jr., Leske, M. C., McCarthy, D., Khu, P., Kashiwagi, T. & Sperduto, R. (1989). Lens opacities classification system II (LOCS II). *Arch Ophthalmol*; *107*, 991-997.

Chylack, L. T. Jr, Wolfe, J., Singer, D., McCarthy, D., Carmen, J. & Rosner, B. (1993). Quantitating Cataract and Nuclear Brunescence, The Harvard and LOCS System. *Optometry and Vision Science*, *70*(11) 886-895.

Chuck, R. S., Shehada, R. E. N., Taban, M., Tungsiripat, T., Sweet, P. M., Mansour, H. N. & McDonnell P. J. (2004). *Arch. Ophthalmol. 122*, 1693.

Chylack, L., Leske, M., Sperduto, R., Khu, P. & McCarthy, D. (1998). Lens opacities classification system. *Arch Ophthalmol.*, *106*,330-4.

Clark, R. N. (1999). *Spectroscopy of rocks and minerals, and principles of spectroscopy*. Remote Sensing for the Earth Sciences. American Society for Photogrammetry and Remote Sensing, John Wiley and Sons Inc. New York, New York, USA.

Coffey V. C. (2012). Multispectral Imaging Moves into the Mainstream. *Opt. and Photo News*, *23*, 124. http://dx.doi.org/10.1364/OPN.23.4.000018.

Colarusso, P., Kidder, K. L., Levin, I. W., Fraser, J. C., Arens, J. F. & Lewis, E. N. (1998). Infrared spectroscopic imaging: from planetary to cellular system. *Applied Spectroscopy*, *52*,106-120.

Colthup, N. (2012). *Introduction to infrared and Raman spectroscopy*. New York: Elsevier Science.

Contag, C. H., Contag, P. R., Mullins, J. I., Spilman, S. D., Stevenson, D. K. & Benaron, D. A. (1995). Photonic detection of bacterial pathogens in living hosts. *Mol. Microbiol*., *18*,593-603.

Cooper, E. A. & Knutson, K. (1995). Fourier transform infrared spectroscopy investigations of protein structure. *Pharm. Biotechnol.*, *7*, 101 143.

Cosentino, A. (2013). A practical guide to panoramic multispectral imaging. *e-Conservation Magazine*, *25*, 64-73.

David, L. L., Dickey, B. M. & Shearer, T. R. (1987). Origin of Urea-Soluble Protein in the Selenite Cataract, the Role of β-Cristalline Proteolysis and Calpain II. *Investigative Ophthalmology & Visual Science*, *28,* 1148-1156.

Davies, A. M. C. (2005). Back to basis: applications of principal component Analysis. *Spect. Euro*., *17*, 30-31.

Davies, A. M. C. and Fearn, T. (2005). Back to basis: the principles of principal component analysis. *Spect. Euro*., *16*, 20-23.

Dickinson, E. & Davidson, W. (2010). Introduction to Spectral Imaging. Retrieved from: http://zeiss-campus.magnet.fsu.edu/print/spectralimaging/introduction-print.html.

De Goes Rocha, F. G., Barbosa Chaves, K. C., Gomes, C. Z., Campanharo, C. B., Courrol, L. C., Schor, N. & Bellini, M. H. (2010). Erythrocyte Protoporphyrin Fluorescence as a Biomarker for Monitoring Antiangiogenic Cancer Therapy. *Journal of fluorescence*, *20*(6), 1225-1231.

Demtroder, W. (2003). *Laser spectroscopy-Basic concepts and instrumentation*, 3rd ed., Springer-Verlag, Berlin.

Demtroder, W. (2008). *Laser spectroscopy*. Vol. 1: Basic Principles, Springer-Verlag, Berlin, Heldelberg, GmbH.

Demtroder, W. (2013). *Laser spectroscopy*: *Spectroscopy with Lasers*. Springer-Verlag, Berlin.

De Oliveira Silva, F. R., Bellini, M. H., Tristao, V. R., Schor, N., Vieira, N. D. Jr. & Courrol, L. C. (2010). Intrinsic fluorescence of protoporphyrin IX from blood samples can yield information on the growth of prostate tumours. *Journal of fluorescence*, *20*(6), 1159-1165.

Diem, M., Chiriboga, L., Lasch, P., & Pacifio, A. (2002). IR spectra and IR spectral maps of individual normal and cancerous cells. *Biopolymers (Biospectroscopy)*, *67*, 349–53.

Dovbeshko, G. I., Gridina, N. Y., Kruglova, E. B., & Pashchuk, O. P, (1997). FTIR spectroscopy studies of nucleic acid damage. *Talanta*, *53*, 233-246.

Dubbelman, M., Van der Heijde R. G. L. & Weeber, H. A. (2005). Change in shape of the aging human crystalline lens with accommodation. *Vision Res*, *45*(1):117–132.

Duncan, G., Wormstone, I. M. & Davies P. D. (1997). The aging human lens: structure, growth and physiological behaviour. *Br J Ophthalmol, 81,* 818-823.

Edwards, H. G., & Chalmers, J. M. (2005). Raman spectroscopy in archaeology and art history (Vol. 9). Cambridge, UK: Royal Society of Chemistry.

Ellis, A. M., Feher, M., & Wright, T. G. (2005). *Electronic and photoelectron spectrocopy; fundermentals and case studies*. New York:Cambidge university Press.

Esbensen, K. H. (2002). *Multivariate Data Analysis – In Practice*. Camo Process AS, Oslo, Norway.

Everitt, B. S. & Dunn, G. (2001). *Applied Multivariate Data Analysis*. 2nd ed. Oxford University Press, London.

Fauaz, G., Miranda, A. R., Gomes, C. Z., Courrol, L. C., de Oliveira Silva, F. R., de Goes Rocha, F. C. & Bellini, M. H. (2010). Erythrocyte Protoporphyrin Fluorescence as a Potential Marker of Diabetes. *Applied Spectroscopy, 64*(4), 391-395.

Fawzy Y., Lam S. & Zeng H. (2015) Rapid Multispectral Endoscopic Imaging System for eal-Time Mapping of the Mucosa Blood Supply in the Lung, *Biomedical optics express, 6*(8). DOI:10.1364/BOE.6.002980.

Feride, S., Toyran, N., Nese, K. & Belma, T. (2000). Fourier Transform Infrared Study of the Effect of Diabetes on Rats Liver and Heart Tissues in the C-H region. *Talanta, 52*, 55-59.

Fisher, R. A. (1936). The use of multiple measurements in taxonomic problems. Ann. of Euge. ***7***, 179-184.

Frey, F. S. & Warda, J. (2008). *American Institute for Conservation of Historic and Artistic Works, Digital Photographic Documentation Task Force: The AIC guide to digital photography and conservation documentation*. Washington, D.C.

Fujikado, T., Kuroda, T., Maeda, N., Ninomiya, S., Goto, H., Tano, Y., Oshika, T., Hirohara, Y. & Mihashi T. (2004). Light scattering and optical aberrations as objective parameters to predict visual deterioration in eyes with cataracts. *Journal of Cataract & Refractive Surgery*, *30*(6), 1198-1208.

Gat, N. (1999). Hyperspectral Imaging. *Spectroscopy*, *14*(3), 28-32.

Gat, N. (2000). Imaging spectroscopy using tunable filters: A Review. *The International Society of Optical Engineering (SPIE)*, *4056*, 50-64.

Gierl, C., Kondo, T., Voos, H., Kongprawechon, W. & Phoojaruenchanachai, S. (2007). Automatic Focusing of a Motorized Photo Slit Lamp Microscope. *Proceedings of the 29th Annual International, Conference of the IEEE EMBS.*, 23-26.

Glasser, A. & Campbell, M. C. (1998). Presbyopia and the optical changes in the human crystalline lens with age. *Vision Res*, *38*(2):209-229.

Graves, E. E., Ripoll, J., Weissleder, R., & Ntziachristos, V. (2003). A Submillimeter Resolution Fluorescence Molecular Imaging System for Small Animal Imaging. *Med. Phys.*, *30*, 901-911. http://dx.doi.org/10.1118/1.1568977.

Greenberg, R. R., Bode, P., & Fernandes, E. A. D. N. (2011). Neuron activation analysis: a primary method of measurement. *Spectrochimica Acta part B: Atomic Spectroscopy*, *66*(3), 193- 241.

Griffiths, P. R. & De Haseth, J. A. (1986) *Fourier Transform Infrared Spectrometry*. John Wiley & Sons: New York.

Griffiths, P. R. & De Haseth, J. A. (2007). *Fourier Transform Infrared Spectrometry*. John wiley publication Second Edition. 529 p.

Gustafsson, U., Somesfalean, G., Alnis, J. & Svanberg, S. (2000). Frequency modulation spectroscopy with blue diode lasers. *Appl. Optics*, *39*, 3774-3780.

Guzek, J. P., Anyomi, F. K., Fiadoyor, S. & Nyonator, F. (2005). Prevalence of blindness in people over 40 years in the Volta region of Ghana. Ghana *Med J*., *39*(2), 52-62.

Haka, A. S., Shafer-Peltier, K. E., Fitzmaurice, M., Crowe, J., Dasari, R. R., & Feld, M. S. (2005). Diagnosing breast canser by using Raman spectroscopy. *Proceedings of the National Academy of Sciences of the United States of America, 102* (35), 12371-12376

Harding, J. J. (1980). *Principle and Techniques of Electron Microscopy*. Academic Press, London, 303-305.

Harwood, L. M., Moody, C. J., & Harwood, L. M. (1989). *Experimental organic chemistry: principles and practice*. Oxford, United Kingdom: Blackwell Scientific.551.

Heftmann, E. (Ed.). (2004). *Chromatography: Fundamentals and applications of chromatography and related differential migration methods-part B. Application*. Amsterdam: Elsevier.

Heise, H. M., Kupper, L. & Butvina, L. N. (1998). Attenuated total reflection mid-infrared spectroscopy for clinical chemistry applications using silver halide fibers. *Sensors and Actuators B: Chemical, 51*(1-3), 84-91.

Helmut, H. T., Angel, G. U., & Robert. J. D. (2007). Laser Chemistry: Spectroscopy, Dynamics and applications, John Wiley & Sons, Ltd ISBN: 978-0-471-48570-4 (HB) ISBN: 978-0-471-48571-1 (PB).

Hemenger, R. P., Garner, L. F. & Ooi, C. S. (1995). Change with age of the refractive index gradient of the human ocular lens. *Invest Ophthalmol Vis Sci*, *36*(3),703-707.

Henson, D. B. **(**1983). *Optometric Instrumentation.* s.l.: Butterworths,

Henson, M. J., & Zhang, L. (2006). Drug characterization in low dosage pharmaceutical tablets using Raman microscopic mapping. *Applied Spectroscopy*, *60*(11), 1247-1255.

Higham, A. D., Wilkinson, B. & D. Kahn, A. (1975). Multispectral Scanning Systems and their Potential Application to Earth- Resources Surveys: Basic Physics and Sensing Technology. *ESA Scientific and Technical Review*. *1*(2), 85-118.

Hiraoka, Y., Shimi, T., & Haraguchi, T. (2002). Multispectral Imaging Fluorescence Microscopy for Living Cells. *Cell. Struct.Funct., 27*, 367-374.

Hof, M., Hutterer, V. & Fidler, V. (2005). *Fluorescence spectroscopy in biology: advanced methods and their applications to membranes, proteins, DNA, and cells*: Berlin: Springer: 3-25.

Hollas, J. M. (2004). *Modern spectroscopy*. Chichster, united Kingdom John Wiley & Sons.

Hotelling, H. (1933). Analysis of a Complex of Statistical Variables Into Principal Components, *Journal of Educational Psychology*, *24*, 417-441 and 498-520.

Horwitz, J. (2003). Alpha-crystallin. *Exp. Eye Res*., *76*, 145-153. (doi:10.1016/S0014-4835(02)00278-6)

Hsu, C. P. S. (1997). Infrared Spectroscopy. *Handbook of Instrumental Techniques for Analytical Chemistry*. F.A. Settle, ed. Prentice Hall PTR, Upper Saddle River, NJ., 247-283.

Hu, Y., Wu, Q., Liu, S., Wei, L., Chen, X., Yan, Z., Yu, J., Zeng, L. & Ding, Y. (2005). Study of Rice Pollen Grains by Multispectral Imaging Microscopy, Microscopy Research and Technique, *Wiley-Liss, Inc*., *68*, 335-346.

IAPB Report. (2010). State of the World Sight. Retrieve from http://www.petteri-teikari.com/pdf/Teikari_Multispectral_Imaging.pdf

Institut Scientifique de la Santé Publique. (2006). Enquête de santé par interview Belgique 2004. Livre II - Chapitre 2: Maladies et affections chroniques. 66-7.

Ishimaru, A. (1978). Wave Propagation and Scattering in Random Media and Rough Surfaces. *Proceedings of the IEEE*, *79*(10), 1045-1050.

Jacques, S.L. (1998). Skin Optics Summary. Oregon Medical Laser Center News. Retrieved from http://omlc.ogi.edu/news/jan98/skinoptics.html.

Jacques, S., & Pogue, B. (2008). Tutorial on diffuse light transport. *Journal of Biomedical Optics*, *13*, 302-310.

Jain, A. K. & Dubes, R. C. (1988). *Algorithms for Clustering Data*. New Jersey, Prentice Hall.

Jain, A. K., Murthy, M. N. & Flynn, P. J. (1999). Data clustering: a review. *ACM Computing Reviews*, **31**(3), 264-323.

Jalil, B. (2008). *Multispectral Image Processing Applied to Dermatology*. MSc thesis, Le2i laboratory, Université de Bourgogne.

Johnson, R. A. & Wichern, D. W. (2002). *Applied Multivariate Statistical Analysis*, 5th ed. Prentice Hall, Upper Saddle River, NJ.

Jones, C. E., Atchison, D. A., Meder, R. & Pope, J. M. (2005). Refractive index distribution and optical properties of the isolated human lens measured using magnetic resonance imaging (MRI). *Vision Res*, *45*(18), 2352-2366.

Jongelbloed, W. L., Van der Want, J. J. L., Worst, J. G. F. & Kalicharan, D. (1998). Stereoscopic Images of Human Cataractous Lens Fibres Obtained with Field Emission Scanning Electron Microscopy Scanning Microscopy*, 11*(4), 653-665.

Kalnina, I., Kurjane, N., Kirilova, E., Klimkane, L., Kirilov, G. & Zvagule, T. (2010). Correlation of altered blood albumin characteristics and lymphocyte populations to tumor stage in gastrointestinal cancer patients. *Cancer biomarkers, 7*(2), 91-99.

Kane, K. E. & Lee, W. S. (2007). Multispectral imaging for in-field green citrus identification. *In ASAE Annual International Meeting*, Minneapolis, MN, Paper 073025.

Kappelhof, J. P., Vrensen, G. F. J. M., de Jong, P. T. V. M., Pameyer, J. H. & Willekens, B. L. J. C. (1986). An Ultrastructural Study of Elschnig's Pearls in the Speudophakic Eyes. *American Journal of Ophthalmology, 101*, 56. Retrieved from https://doi.org/10.1016/0002-9394(86)90465-4

Katzir, A. (1993). *Lasers and optical fibres in medicine*. Academic Press, New York.

Karadaglic, D., Wood, A. D., McRobbie, M., Stojanovic, R. & Herrington, C. S. (2009). Fluorescence spectroscopy of an in vitro model of human cervical neoplasia identifies graded spectral shape changes with neoplastic phenotype and a differential effect of acetic acid. *Cancer epidemiology*, *33*(6), 463-468.

Kaufman, L. and Rousseeuw, P. J. (2005), Finding Groups in Data: An Introduction to Cluster Analysis, John Wiley & Sons Inc., New Jersey.

Kauranen, P., Hertz, H. M., & Svanberg, S. (1994). Tomographic imaging of fluid flows using two-tone frequency-modulation spectroscopy. *Opt. Lett.*, *19*, 1489-1491.

Kessel, L., Eskildsen, L., Lundeman, J.H., Ole Bjarlin Jensen, O.B. & Larsen, M. (2011) Optical Effects of Exposing Intact Human Lenses to Ultraviolet Radiation and Visible Light. *BMC Ophthalmology*, *11*, 41. Retrieved from https://doi.org/10.1186/1471-2415-11-41.

Klein, B., Klein, R., Linton, K., Magli, Y. & Neider, M. (1990). Assessment of Cataracts from Photographs in the Beaver Dam Eye Study. *Ophthalmology*, *97*, 1428-1433

Kluczynski, P., Lindberg, A. M. & Axner, O. (2001). Characterization of background signals in wavelength-modulation spectroscopy in terms of a Fourier based theoretical formalism. *Appl. Opt.*, *40*, 770-782.

Knee, J. L. (1996). Spectra of Atoms and Molecules by Peter F. Bernath. *Am. J. Phy.*, *64*, 93-93

Kwong, K. K., Belliveau, J. W., Chesler, D. A., Goldberg, I. E., Weisskoff, R. M., Poncelet, B. P., Kennedy, D. N., Hoppel, B. E., Cohen, M. S., Turner, R., Cheng, H-M, Brady, T. J. & Rosen, B. R. (1992). Dynamic magnetic resonance imaging of human brain activity during primary sensory stimulation. *Proc. Natl. Acad. Sci. U.S.A.*, *89*(12), 5675-5679.

Kyei, S., Kuffuor, G. A., Ramkissoon, P., Afari, L. & Asiamah, E. A. (2015). The Claim of Anti-Cataract Potential of Heliotropium Indicum: A Myth or Reality? *Ophthalmology and Therapy*, *4*, 115-128. https://doi.org/10.1007/s40123-015-0042-2

Lakowicz, J. R. (1999) *Principles of Fluorescence Spectroscopy*, 2nd ed. Kluwer, Academic /Plenum publishers, New York.

Lakowicz, J. R. (2006). *Principles of Fluorescence Spectroscopy*. New York: Springer Science & Business Media.

Lambert, J. H. (1760). *Photometry, or, On the measure and gradations of light, colors, and shade*. Augsburg, Germany: Eberhardt Klett.

Lang, M., Lichtenthaler, H. K., Sowinska, M., Summ, P., Heisel, F., Miehe, J. A. & Tomasini, F. (1995). *Application of laser-induced fluorescence imaging in the detection of plant stress Proc*. 2nd Int. Symp. Exhibition on Environmental Contamination in Central and Eastern Europe (Budapest, 1994*)*, P. I. Richter and R. C. Herndon (Ed.), Rockville, USA: Government Institutes. 88–90.

Lerman, S. & Borkman, R. (1976). Spectroscopic evaluation and classification of the normal, aging and cataractous lens. *Ophthalmol Res.*, *8*, 335-353.

Levenson, R. M. & Hoyt, C. C. (2000). Spectral imaging and microscopy. *Am Lab*, *32*, 26-33.

Levenson, R. M. & Mansfield, J. R. (2006). Multispectral Imaging in Biology and Medicine: Slices of Life.. *Cytometry A*, *69*, 748-758. Retrieved from http://dx.doi.org/10.1002/cyto.a.20319.

Levenson, R. M., Fornari, A. & Loda M. (2008). Multispectral Imaging and Pathology: Seeing and Doing More, *Expert Opin Med Diagn*, *2*(9), 1067-1081.

Liquier, J. & Taillandier, E. (1996). *Infrared spectroscopy of nucleic acids*. InMantsch, H. H. & Chapman, D., eds. *Infrared Spectroscopy of Biomolecules*. New York: Wiley-Liss, 131–158.

Loree, T. R., Johnson, T. M. & Birmingham, B. S. (1988). Fluorescence spectra of corneal tissue under excimer laser irradiation. *Proc SPIE*, *908*, 65.https://doi.org/10.1117/12.945344.

Luker, G. D. & Luker, K. E. (2008). Optical Imaging: Current Applications and Future Directions. *J. Nucl. Med.*, *49*, 1-4.

Lyng, F., Gazi, E. & Gardner, P. (2011). *Preparation of Tissues and Cells for Infrared and Raman Spectroscopy and Imaging*. Biomed Appl Synchrotron Infrared Microspectrosc.145–89.

Maloof, A. J., Pandey, S. K., Neilson, G., & Milverton, E. (2005). Selective Death of Lens Epithelial Cells Using Demineralized Water and Triton X-100 With PerfectCapsule Sealed Capsule Irrigation: A Histological Study in Rabbit Eyes. *Arch Ophthalmol.*, *123*(10),1378-1384.

Mantsch, H. H. & Chapman, D. (1996). *Infrared Spectroscopy of Biomolecules*. John Wiley & Sons Inc.

Marc-Michael, B. & Harald, J. (2012). Historical Perspective and Modern Applications of Attenuated Total Reflectance – Fourier Transform Infrared Spectroscopy (ATR-FTIR). *Drug Test*, *4*, 298–302.

Martens, H. and Naes, T. (1991) *Multivariate Calibration*. John Wiley and Sons Ltd, Chichester.

Martinez, W. L. & Martinez, A. R. (2005). *Exploratory Data Analysis with MATLAB®*. Computer Science and Data Analysis Series, Chapman & Hall/CRC.

Maslov N. A., Larionov P. M., Rozhin I. A., Druzhinin I. B., & Chernykh V. V. (2016). Laser induced fluorescence spectroscopy of the secondary cataract, *Optics and Spectroscopy*, *120*(6), 983–987.

Masilamani, V., Trinka, V., Al Salhi, M., Elangovan, M., Raghavan, V., Al Diab, A. R. & Al-Nachawati, H. (2011). A new lung cancer biomarker-a preliminary report. *Photomedicine and laser surgery*, *29*(3), 161-170.

Matthews, P. M., Honey, G. D. & Bullmore, E. T. (2006). Applications of fMRI in translational medicine and clinical practice. *Nat. Rev. Neurosci.*, *7*(9), 732-744.

Matthias, F. (2006). Spectral image processing in real-time. *J. Real-Time Image Proc*, *1*, 25-32.

McCarty C, A. & Taylor, H. R. (2002). A review of the epidemiologic evidence linking ultraviolet radiation and cataracts. *Dev Ophthalmol.*, *35*, 21-31.

Merdasa, A. (2010). *Multispectral Microscopy with application to Malaria Detection*. Master thesis, Division of Atomic Physics, Lund University.

Michael, R. & Bron, A. J. (2011). The Ageing Lens and Cataract: A Model of Normal and Pathological Ageing. *Philosophical Transactions of the Royal Society B*, *366*, 1278-1292. Retrieved from https://doi.org/10.1098/rstb.2010.0300.

Michaelis, J., Hettich, C., Mlynek, J. & Sandoghdar, V. (2000). Optical microscopy using a single-molecule light source. *Nature*, *405*(6784), 325-328.

Mie, G. (1908). Contributions to the optics of diffuse media, especially colloid metal solutions. *Ann Phys*., *25*, 377-445.

Mikkel, B., Zuguang, G. & Sune, S. (2008). Broad-band multispectral microscope for imaging transmission spectroscopy employing an array of light-emitting diodes, *American Journal of Physics*. *77*(2), 104-110.

Millar, W. J. (2004). Problèmes de vision chez les personnes âgées. Dans: Rapports sur la santé. *16* (1), 49-54.

Milosevic M. & Berets S. L. (1993). *Appl. Spectrosc.47* ,566.

Mirabella, F. M. Ed. (1993). In Internal Refection Spectroscopy: Theory and Applications; Marcel Dekker, Inc.: New York, *15*.

Mitchell, H. S. & Cook, G. M. (1938). Galactose cataract in rats: factors influencing progressive and regressive changes. *Arch Ophthalmol*., *19*(1):22-33.

Mitton, K. P., Hess, J. L. & Bunce, G. E (1995). Causes of decreased phase transition temperature in selenite cataract model. *Invest Ophthalmol Vis Sci*., *36*, 914.

Moll, A. C., Van der Linder, A. J. H., Hogeweg, M., Schader, W. E., Hermans, J. & De, K. (1994). Prevalence of blindness and low vision of people over 30 years in the Wenchi district, Ghana, in relation to eye care programmes. Br *J Ophthalmol*., *78*, 275-279.

Morris, M. D. (1993). *Microscopic and spectroscopic imaging of the chemical State*. New York, Marcel Dekker.

Movasaghi, Z., Rehman, S., & Rehman, I. U. (2007). Raman spectroscopy of biological tissues. Applied Spectroscopy Reviews, 42 (5), 493-541.

Movasaghi, Z., Rehman, S. & Rehman, I. (2008). Fourier Transform Infrared (FTIR) Spectroscopy of Biological Tissues'', *Applied Spectroscopy Reviews*, *43*(2), 134-179, DOI:10.1080/05704920701829043

Nakamoto, K. (1977). *Infrared and Raman spectra of inorganic and coordination compounds*. Hoboken, New Jersey: John Wiley & Sons.

Nieves, J. L., Valero, E. M., Nascimento, S. M. C., Hernandez-Andres, J. & Romero, J. (2005). Multispectral synthesis of daylight using a commercial digital CCD camera. *Appl. Opt*., *44*, 5696-5703.

Nijssen, A., Schut, T. C. B., Heule, F., Caspers, P. J., Hayes, D. P., Neumann, M. H., & Puppels, G. J. (2002). Discriminating basal cell carcinoma from its surrounding tissue by Raman spectroscopy. Journal of Investigative Dermatology, *119* (1), 64-69.

Ning, P. B., Gong, C. M., Zhang, Y. M., Guo K. K. & Bai J. (2011). Lead, cadmium, arsenic, mercury and copper levels in Chinese Yunnan Pu'er Tea. *Food Addit Contam B*, *4*, 28-33.

Nischan, L.M., Joseph, R.M., Libby, J.C. & Kerekes, J.P. (2003). Active spectral imaging. *Lincoln Laboratory Journal*, *14*(1), 131-144.

Ogawa, S., Lee, T. M., Kay, A. R. & Tank, D. W. (1990). Brain magnetic resonance imaging with contrast dependent on blood oxygenation. *PNAS*, *87*(24), 9868-9872.

Okano, T., Uga, S., Ishikawa, S. & Shumiya, S. (1993). Histopathological Study of Hereditary Cataractous Lenses in the SCR Strain Rat. *Experimental Eye Research*, *57*, 567-576. https://doi.org/10.1006/exer.1993.1161

Okuno, T., Nakanishi-Ueda, T., Ueda, T., Yasuhara, H. & Koide, R. (2012). Ultraviolet action spectrum for cell killing of primary porcine lens epithelial cells. *J Occup Health*, *54*, 181-186.

Ondrej, C., Zdenek, B., Adam, L., Antonin R., Bretislav, M., Josef, L. & Lenka, V. (2014). Laser- induced fluorescence spectroscopy in tissue local necrosis detection", *Proc. SPIE 8941*, *Optical Interactions with Tissue and Cells XXV; and Terahertz for Biomedical Applications*, *89411D*. Retrieved from https://doi.org/10.1117/12.2052637

Ong, C.W., Shen, Z. X., Ang, K. K. H., Kara, U. A. K. & Tang, S. H. (2002). Raman microspectroscopy of normal erythrocytes and Plasmodium berghei-infected erythrocytes. *Appl. Spectrosc.*, *56*, 1126-1131.

Opoku-Ansah, J. (2012). *Development of a multispectral light emitting diode imaging microscope for malaria red blood cells diagnostics*. Master of Philosophy Thesis, University of Cape Coast.

Opoku-Ansah, J., Eghan, M. J., Anderson, B. & Boampong, J. N. (2014). Wavelength Markers for Malaria (Plasmodium Falciparum) Infected and Uninfected Red Blood Cells for Ring and Trophozoite Stages, *Applied Physics Research*, *6*(2), 2014 ISSN 1916-9639 E-ISSN 1916-9647.

Opoku- Ansah J., Eghan, M. J., Anderson, B., Nyarko Boampong, J. & Buah-Bassuah P. K. (2016). Laser-Induced Autofluorescence technique for Plasmodium falciparum Parasite Density Estimation, *Applied Physics Research*, *8*(2), 43-51.

Retrieved from URL: http://dx.doi.org/10.5539/apr.v8n2p43.

Opoku- Ansah J., Anderson, B., Eghan, M. J., Osei – Wusu Adueming, P. & Amuah C. L. Y. (2017). A Retrofitted Metallurgical Microscope Using Light Emitting Diodes for Multi-Spectral Imaging, Modern Applied Science, *11*(9), 30 -38,

Retrieved from https://doi.org/10.5539/mas.v11n9p30.

Palmer, J. M. & Grant, B. G. (2009). *The Art of Radiometry*. Vol: PM 184, SPIE PRESS, Bellingham, Washington, USA.

Park, J. I., Lee, M. H., Grossberg, M. D. & Nayar, S. K. (2007). Multispectral imaging using multiplexed illumination. *IEEE 11th International Conference on Computer Vision*, 1-8.

Peng, C. & Liu J. (2013). Studies on Red-Shift Rules in Fluorescence Spectra of Human Blood Induced by LED. *Appl. Phy. Res.*, *5*(1), 1-6.

Retrieved from http://dx.doi.org/10.5539/apr.v5n1p1.

Philipson, B. (1973). Changes in the lens related to the reduction of transparency. *Exp Eye Res.*, *16*, 29-39.

Phillips, A. F. & McDonnell, P. J. (1997). *Am. J. Ophthalmol*. *123*, 42.

Platt, U., & Stutz, J. (Eds). (2008). Differential absorption spectroscopy. In Kim, Y., Platt, U., Gu, M. B. & Iwahashi, H. *Atmospheric and Biological Environmental Monitoring* (pp. 135-174). Heidelberg, Berlin: Springer.

Prasad, P. N. (2003). *Introduction to biophotonics*, Hoboken, NJ: Wiley-Interscience.

Raman, C. V. & Krishman, K. S. (1928). A new type of secondary radiation. *Nature, 121* (3048).

Rayleigh, L. (1881). On the electromagnetic theory of light. *Philos. Mag.*, *12*(73), 81, 101.

Resnikoff, S., Pascolini, D. & Mariotti Pokharel, G. P (2004). Global magnitude of visual impairment caused by uncorrected refractive errors in 2004. Bull *World Health Organ.*, *86*(1), 63-70

Rice, B. W., Cable, M. D. & Nelson, M. B. (2001). In Vivo Imaging of Light-Emitting Probes. *J. Biomed. Opt.*, *6*, 432-440. Retrieved from http://dx.doi.org/10.1117/1.1413210.

Richard, M., Paul, J. & Neal, R. (2002). *Spectral Imaging and Biomedicine*. New Devices New Approaches, Proceedings of the 31st Applied Imagery Pattern Recognition Workshop.

Ross, N. E., Pritchard, C. J., Rubin, D. M. & Duse, A. G. (2006). Automated image processing method for the diagnosis and classification of malaria on thin blood smears. *Medical and Biological Engineering and Computing*, *44*, 427-436.

Sangare, M., Agneroh, T. A., Bagui, O. K., Traore, I., Ba, A. & Zoueu, J. T. (2015). Classification of African Mosaic Virus Infected Cassava Leaves by the Use of Multi-Spectral Imaging. *Optics and Photonics Journal*, *5*, 261-272. Retrieved from http://dx.doi.org/10.4236/opj.2015.58025

Sasaki, K., Sakamoto, Y., Fujisawa, K., Kojima, M. & Shibata, T. (1997). A New Grading System for Nuclear Cataracts - An Alternative to the Japanese Cooperative Cataract Epidemiology Study Group's Grading System. *Cataract Epidemiology*. *27*, 42-49.

Sauer, M., Hofkens, J. & Enderlein, J. (2010). *Handbook of Fluorescence Spectroscopy and Imaging: From Ensemble to Single Molecules*. Weinheim, Germany: John Wiley & Sons.

Schaepman, M. E., Ustin, S. L., Plaza, A. J., Painter, T. H., Verrelst, J. & Liang, S. (2009). Earth system science related imaging spectroscopy-An assessment. *Elsevier Inc.*, *Remote Sensing of Environment*, *113*, 123-137.

Schilt, S., Thevenaz, L. & Robert, P. (2003). Wavelength modulation spectroscopy: combined frequency and intensity laser modulation. *Appl. Opt.*, *42*(33), 6728-6738.

Sharma, K. K. & Santhoshkumar, P. (2009). Lens aging: effects of crystallins. *Biochim. Biophys. Acta*, *1790*, 1095–1108. (doi:10.10.1016/j.bbagen.2009.05.008).

Shearer, T. R., David, L. L., Anderson, R. S. & Azuma, M. (1992). Review of selenite cataract. *Curr Eye Res.*, *11*, 357.

Sigrist, M. W. (1994). *Air monitoring by spectroscopic techniques*. New York: John Wiley & Sons.

Slater, D. & Healey, G. (1999). Material Classification for 3D Objects in Aerial Hyperspectral Images. *Proc. Computer Vision and Pattern Recognition*, *2*, 268-273.

Smith, B. C. (1996). *Fundamentals of Fourier Transform Infrared Spectroscopy*; CRC Press: London; Chapter 4.

Somesfalean, G. (2004). *Environmental Monitoring using Diode Laser Spectroscopic Techniques*. Phd Thesis, Lund Report on Atomic Physics, 329.

Sparrow, J. M., Brown, N. A. P., Shun-Shin G. A. & Bron A. J. (1990). The Oxford modular cataract image analysis system. *Eye*. *4*, 638-648.

Standring, S. (2008). *Gray's anatomy: The anatomical basis of clinical practice*. ISBN: 97807071645, Elsevier.

Stuart, B.H. (2004). *Infrared Spectroscopy: Fundamentals and Applications*. Wiley, United Kingdom.

Sun, D. W. (Ed). (2008). *Modern techniques for food authentication*. Burlington, USA: Academic press.

Sun, X. & Anderson, J. M. (1993). A Spatially Variable Light-Frequency-Selective Component-Based, Airborne Pushbroom Imaging Spectrometer for the Water Environment. *Photogrammetric Eng. & Remote Sensing*, *59*(3), 399-406.

Svanberg, S. (1992). *Atomic and molecular spectroscopy*, 2nd ed., Springer Verlag, Berlin.

Svanberg, S. (1993). *Air Pollution Monitoring with Optical Techniques* Chpt.3, M. Sigrist (ed.) (Wiley, New York).

Svanberg, S. (2004). *Atomic and Molecular spectroscopy*: Basic Aspects and Practical Applications, 4th ed., *Springer*, Berlin.

Svanberg, S. (2009). Optical analysis of trapped gas-gas in scattering media absorption spectroscopy. *Laser Physics*, *19*, 1-10.

Svanberg, S. (2012). *Atomic and molecular spectroscopy*, 6th ed., Springer Verlag, Berlin.

Taylor, H. R. (1999). Epidemiology of age-related cataract. *Eye*., *13*, 445-448

Teikari, P. (2008). Multispectral imaging. Course project for AS-75.2128 imaging and display technology, Helsinki University of Technology.

Thanh, N. T., Wehrens, R. & Buydens, L. M. C. (2004). Clustering multispectral images: a tutorial. *Chemometrics and Intelligent Laboratory Systems*, *77*, 3-17.

The Royal College of Ophthalmologists (2004). Cataract surgery guidelines. p. 6. Retrieved from https://www.rcophth.ac.uk/wp-content/uploads/2014/12/2010-SCI-069-Cataract-Surgery-Guidelines-2010-SEPTEMBER-2010-1.pdf

Thermo Nicolet Co. (2001). Introduction to Fourier Transform Infrared Spectrometry. http://mmrc.caltech.edu/FTIR/FTIRintro.pdf Accessed Mar. 19, 2008.

Thylefors, B. (1997). Global data on blindness. *Bull World Hlth Org*., *73*, 115-121.

Thylefors, B., Chylack, Jr. L.T., Konyamia, K., Sasaki, K., Sperduto, R., Taylor, H. R. & West, S. (2002). A Simplied Cataract Grading System – The WHO Cataract Grading Group. *Ophthalmic Epidemiology*, *9*(2), 83–95.

Tuchin, V. (2007). *Tissue Optics: Light Scattering Methods and Instruments for Medical Diagnosis*. 2nd ed., SPIE, Bellingham.

Tuft, S., Al-Dhahir, R., Dyer, P. & Zehao ,Z. (1990). Characterization of the fluorescence spectra produced by excimer laser irradiation of the cornea. *Invest Ophthalmol Vis Sci*; *31*, 1512.

Van de Hulst, V.H.C. (1981). *Light scattering by small particles*. Dover Publications Inc., New York.

Van Den Berg, F. M., Van Amstel, P. J., Janse, C. J., Meis, J. F. G. M. & Mons, B. (1991). Detection of different developmental stages of malaria parasites by non-radioactive DNA in situ hybridization. *Histochemical Journal*, *23*, 109-115.

Van Der Linden, A., Van Camp, N., Ramos-Cabrer, P. & Hoehn, M. (2007). Current status of functional MRI on small animals: Application to physiology, pathophysiology, and cognition. *NMR Biomed*., *20*(5), 522-545.

Vo-Dinh, T. (2003). *Biomedical Photonics Handbook*, CRC Press LLC, New York.

Walsh, L. J. & Shakibaie, F. (2007). Ultraviolet-induced fluorescence: shedding new light on dental biofilms and dental caries. *Australasian Dental Practice*, *18*(6), 1-7.

Wang, P. G. (Ed.). (2008). *High-throughput analysis in the pharmaceutical industry* (pp 265 – 270). Boca Raton: CRC Press.

Wang, Z., Tangella K., Balla, A. & Popescua, G. (2011). Tissue Refractive Index as Marker of Disease. *Journal of Biomedical Optics*, *16,* 116017. Retrieved from https://doi.org/10.1117/1.3656732.

Wartewig, S., & Neubert, R. H. (2005). Pharmaceutical applications of Mid-IR and Raman spectroscopy. Advanced drug delivery reviews, *57* (8), 1144-1170.

Weale, R. A. (1985). Human lenticular fluorescence and transmissivity, and their effects on vision. *Exp Eye Res.*, *41*, 457-473.

Webster, G. T., Tilley, L., Deed, S., McNaughton, D. & Wood, B. R. (2008). Resonance Raman spectroscopy can detect structural changes in haemozoin (malaria pigment) following incubation with chloroquine in infected erythrocytes. *FEBS letters*, *582* (7), 1087-1092.

Weibring, P., Edner, H. & Svanberg, S. (2003). Versatile mobile lidar system for environmental monitoring. *Applied Optics*, *42*, 3583-3594.

Wellman, J. B. (1981). Multispectral Mapper: Imaging Spectroscopy as Applied to the Mapping of Earth Resources. *Proc. SPIE Imaging Spectroscopy*, *268*, 64-73.

West, S. K. & Taylor, H. R. (1986). The detection and grading of cataracts: an epidemiologic perspective. *Surv Ophthalmol.*, *31*,175-84.

West, S. K, Rosenthal, F., Newland, H. S. & Taylor, H. R. (1988). Use of photographic techniques to grade nuclear cataracts. *Invest Ophthalmol Vis Sci*; *29*, 73.77

Wilson, R. H., Vishwanath, K. & Mycek, M. (2016). Optical methods for quantitative and label-free sensing in living human tissues: principles, techniques, and applications, *Advances in Physics*: *X*, *1*(4), 523-543, DOI: 10.1080/23746149.2016.1221739.

Wood, B. R., Steven, J. L., Cooke, B. M., Glenister, F. K., Lim, J. & McNaughton, D. (2003). Raman imaging of hemozoin within the food vacuole of *Plasmodium falciparum* trophozoites. *FEBS Lett.*, *554*, 247-252.

Wood, B. R., Langford, S. J., Cooke, B. M., Lim, J., Glenister, F.K., Duriska, M., Unthank, J. K. & McNaughton, D. (2004). Resonance Raman spectroscopy reveals new insight into the electronic structure of *β*-hematin and malaria pigment. *J. Am. Chem. Soc.*, ***126***, 9233-9239.

Workman, J. Jr. (2001). *Interpretive spectroscopy for near-infrared, The Handbook of Organic Compounds;* Academic Press: California; 143-182.

Winkler, B. S. & Riley, M. V. (1991). Relative contributions of epithelial cells and fibers to rabbit lens ATP content and glycolysis. *Invest. Ophthalmol. Vis. Sci.*, *32*(9), 2593-2598.

Xu, Y., Gao, X., Lin, S., Wong, D. W. K., Liu, J., Xu, D., Cheng, C., Cheung, C. Y. & Wong, T. Y. (2013). Automatic Grading of Nuclear Cataracts from Slit-Lamp Lens Images Using Group Sparsity Regression.*International Conference on Medical Image Computing and Computer Assisted Intervention (MICCAI)*, *16*, 468-475. Retrieved from https://doi.org/10.1007/978-3-642-40763-5_58.

Yang, Y., Ye, Y., Li, F. & Ma, P. (1987). Characteristic autofluorescence for cancer diagnosis and its origin. *Lasers Surg Med.*,*7*, 528-32.

Yang, D., & Ying, Y. (2011). Applications of Raman spectroscopy in agricultural products and food analysis: A review. *Applied Spectroscopy Reviews*, *46* (7), 539-560.

Yang J. I., Yeh D. B., Kuo J. M., Pan B.S., Lee, G. C., Liu Y. H. & Lai Y. J. (2012). Detection of copper Ions in liquid foods and beverages based on an enzymatic method. *J Food Drug Anal*; *20(1)*, 83-87.

Yolcu U., Sahin, O. F. & Gundogan, F. C. (2014). *Imaging in Opthalmology*. Retrieved from http://dx.doi.org/10.5772/58314.

Yuval, G., Ian, T. & McNamara, G. (2006). Spectral Imaging: Principles and Applications. *Cytometry Part A*, *69*(8), 735-47. DOI:10.1002/cyto.a.20311

Zeiss. (2001). Eye Examination with the Slit Lamp. Retrieved from http://www.frankshospitalworkshop.com/equipment/documents/ophthalmology/equipment/Eye%20Examination%20with%20the%20Slit%20Lamp%20-%20Carl%20Zeiss.pdf

Zhang, H. F., Maslov, K. & Wang, L. V. (2007) In Vivo Imaging of Subcutaneous Structures using Functional Zhang. *Photoacoustic microscopy*, *Nat. Protoc*., *2*(4), 797-804. Retrieved from http://dx.doi.org/10.1038/nprot.2007.108

Zhang, Y., Hong, H & Cai, W. (2011). Photoacoustic Imaging, *Col. Spr. Harb. Protoc*. Retrieved from http://dx.doi.org/10.1101/pdb.top065508

Zhao, L. J., Ren, T. & Zhong, R. G. (2012). Determination of lead in human hair by high resolution continuum source graphite furnace atomic absorption spectrometry with microwave digestion and solid sampling. *Anal Lett*, *45*(16), 2467-2481.

Zheng, W., Lau, W., Cheng, C., Soo, K. C. & Olivo, M. (2003). Optimal excitation-emission wavelengths for autofluorescence diagnosis of bladder tumors. *Int J. Cancer*, *104*(4), 477-481.

Zhou, X., Liu, X., Jeffries, J. B. & Hanson, R. K. (2005). Selection of NIR H_2O absorption transitions for in-cylinder measurement of temperature in IC engines. *Meas. Sci. Technol.*, *16*, 2437–2445.

Zhou, L. & El-Deiry, W. S. (2009) Multispectral Fluorescence Imaging, *J. of Nucl. Med.*, *50*, 1563-1566.

Retrieved from http://dx.doi.org/10.2967/jnumed.109.063925

Zimmerman, T., Rietdorf, J. & Pepperkok, R. (2003). Spectral imaging and its application in live cell microscopy. *FEBS Lett.*, *546*, 87–92.

Zohdi, V., Whelan, D. R., Wood, B. R., Pearson, J. T., Bambery, K. R. & Black, M. J. (2015). Importance of Tissue Preparation Methods in FTIR Micro-Spectroscopical Analysis of Biological Tissues: "Traps for New Users." *PLoS One*, *10*(2), -0116491.

Zoris, L. & Stojcic M. (2013), The influence of ultravoilet radiation on the Eye *Primary Health Care*, *3*(1), doi: 10.4172/2167-1079.1000133

Zuclich, J., Previc, F. H., Novar, B. J. & Edsall, P. R. (2005). Near UV/Blue light -induced fluorescence in the human eye: Potential interference with visual function. *J. Biomed. Opt*. *10*(4), 44021. doi: 10.1117/1.1990163.

APPENDIX

PEER REVIEW PUBLICATION AND POSTER

1. **Adueming, P.O.-W.**, Eghan, M. J., Anderson, B., Kyei, S., Opoku - Ansah, J., Amuah, C.L.Y.,Sackey, S .S and Buah -Bassuah, P.K. (2017) Multispectral Imaging in Combination with Multivariate Analysis Discriminates Selenite Induced Cataractous Lenses from Healthy Lenses of Sprague-Dawley Rats. Open Journal of Biophysics, 7, 145- 156. https://doi.org/10.4236/ojbiphy.2017.73011
2. **P. Osei - Wusu Adueming**, M. J. Eghan, B. Anderson, S. Kyei, J. Opoku-Ansah, and C. L. Y. Amuah ‘ Multispectral Imaging of Ocular Tissue: A study to discriminate healthy Lenses from Cataractous lenses of Sprague-Dawley Rat’ Presented at Winter College on Optics - Applied Optical Techniques for Bio-imaging: Advanced Microscopy and Spectroscopy in Life and Environmental Sciences. Trieste, Italy. 13/02/2017-24/02/2017.